Title

Crystalline Disposal R&D at LBNL: FY20 Progress Report

Authors

Guglielmi, Yves
Chang, Chun
Cook, Paul
et al.

Publication Date

2020-07-20

Peer reviewed

Crystalline Disposal R&D at LBNL: FY20 Progress Report

Spent Fuel and Waste Disposition

Prepared for
US Department of Energy
Spent Fuel and Waste Science and Technology

Yves Guglielmi[1], Chun Chang[1], Paul Cook[1], Patrick Dobson[1], Florian Soom[1], Seiji Nakagawa[1], Auli Niemi[2], Chris Juhlin[2], Henning Lorenz[2], Jan-Erik Rosberg[3], Benoît Dessirier[4], Chin-Fu Tsang[1],[2], Alexandru Tatomir[2], Farzad Basirat[2], Emil Lundberg[2], Bjarne Almqvist[2], Sharon Borglin[1], Christine Doughty[1], LianGe Zheng[1]
[1]LBNL, [2]Uppsala University, [3]Lund University, [4]Stockholm University

June 18, 2020
LBNL-2001334
SFWD Working Document: External Release

This page intentionally left blank.

Revision 6
10/07/2019

APPENDIX E

NFCSC DOCUMENT COVER SHEET [1]

Name/Title of Deliverable/Milestone/Revision No.	Crystalline Disposal R&D at LBNL: FY20 Progress Report / M4SF-20LB010302031
Work Package Title and Number	Crystalline Disposal R&D - LBNL / SF-20LB01030203
Work Package WBS Number	1.08.01.03.02
Responsible Work Package Manager	Liange Zheng (signature on file)
	(Name/Signature)
Date Submitted	**06/18/2020**

Quality Rigor Level for Deliverable/Milestone[2]	☐ QRL-1 ☐ Nuclear Data	☐ QRL-2	☐ QRL-3	X QRL 4 Lab-QA Program[3]

This deliverable was prepared in accordance with Lawrence Berkeley National Laboratory (LBNL)
(Participant/National Laboratory Name)

QA program which meets the requirements of
X DOE Order 414.1 ☐ NQA-1 ☐ Other

This Deliverable was subjected to:

X Technical Review ☐ Peer Review

Technical Review (TR)	**Peer Review (PR)**
Review Documentation Provided	**Review Documentation Provided**
☐ Signed TR Report or,	☐ Signed PR Report or,
☐ Signed TR Concurrence Sheet or,	☐ Signed PR Concurrence Sheet or,
X Signature of TR Reviewer(s) below	☐ Signature of PR Reviewer(s) below
Name and Signature of Reviewers	**Name and Signature of Reviewers**
Liange Zheng (all sections)	Yuxin Wu - Section 2
(signature on file)	(signature on file)
Boris Faybishenko (all sections)	Timothy Kneafsey – Section 3
(signature on file)	(signature on file)

NOTE 1: *Appendix E should be filled out and submitted with each deliverable. Or, if the PICS:NE system permits, completely enter all applicable information in the PICS:NE Deliverable Form. The requirement is to ensure that all applicable information is entered either in the PICS:NE system or by using the FCT Document Cover Sheet.*

- *In some cases there may be a milestone where an item is being fabricated, maintenance is being performed on a facility, or a document is being issued through a formal document control process where it specifically calls out a formal review of the document. In these cases, documentation (e.g., inspection report, maintenance request, work planning package documentation or the documented review of the issued document through the document control process) of the completion of the activity, along with the Document Cover Sheet, is sufficient to demonstrate achieving the milestone.*

NOTE 2: *If QRL 1, 2, or 3 is not assigned, then the QRL 4 box must be checked, and the work is understood to be performed using laboratory specific QA requirements. This includes any deliverable developed in conformance with the respective National Laboratory / Participant, DOE or NNSA-approved QA Program*

NOTE 3: *If the lab has an NQA-1 program and the work to be conducted requires an NQA-1 program, then the QRL-1 box must be checked in the work Package and on the Appendix E cover sheet and the work must be performed in accordance with the Lab's NQA-1 program. The QRL-4 box should not be checked*

This page is intentionally left blank.

CONTENTS

This page is intentionally left blank.

LIST OF FIGURES

LIST OF TABLES

ACRONYMS

AF	Artificial Fracture
COSC	Collisional Orogeny in the Scandinavian Caledonides
DFN	Discrete Fracture Network
DI	Deionized
DP	Pressure Differences
EC	Electrical Conductivity
EDZ	Excavation Disturbed Zone
FCP	Fault Closing Pressure
FEPs	Features, Events, and Processes
FFEC	Flowing Fluid Electrical Conductivity
FCP	Fracture Closing Pressure
FOP	Fracture Opening Pressure
FPP	Fracture Propagation Pressure
HiP	High Pressure
KG^2B	K for Grimsel Granodiorite Benchmark
LBNL	Lawrence Berkeley National Laboratory
LVDT	Linear Variable Differential Transformer
NAGRA	National Cooperative for the Disposal of Radioactive Waste
PM	Permeability Modifier
PV	Pore Volume
R&D	Research and Development
SIMFIP	Step-rate Injection Method for Fracture In-situ Properties
SFWST	Spent Fuel and Waste Science and Technology
SRT	Step Rate Test
Ti	Titanium
URL	Underground Research Laboratory

This page is intentionally left blank.

CRYSTALLINE DISPOSAL R&D AT LBNL: FY20 PROGRESS REPORT

1. INTRODUCTION

Within the Spent Fuel & Waste Science and Technology (SFWST) Program, research work continues further with the goal to better understand long-term performance of disposal systems in three main geologic rock types: clay/shale, salt, and crystalline rock. This report documents LBNL's research activities related to investigations of crystalline host rock according to the scope of two work packages: SF-20LB01030207 "Crystalline International Collaborations – LBNL," and SF-20LB01030203 "Crystalline Disposal R&D – LBNL." These research activities correspond are related to key Features, Events, and Processes (FEPs), ranked in importance from medium to high, as listed in Table 7 of the Used Fuel Disposition Campaign Disposal Research and Development Roadmap (FCR&D-USED-2011-000065 REV0) (Nutt, 2011). Specifically, these research activities address FEP 2.2.01, Excavation Disturbed Zone (EZD). The results of these research activities provide important insights into understanding and predicting flow and transport processes that could occur in low-permeability crystalline rocks, in which fractures might serve as main conduits for fluid flow and radionuclide transport. The evolution of the EDZ during the excavation of the tunnel as well as the evolution of microcrack growth within the EDZ after the emplacement of backfill are critical for predicting the long- term behavior of the EDZ. A number of factors including stress, temperature, water activity, capillary pressure, chemistry, and mineralogy can affect the rock evolution, which require advanced experimental tools to study it.

Section 2 of this report presents a description of a new laboratory test apparatus being developed to characterize the rock of the excavation damage zone (EDZ) in a mined crystalline repository. We have developed a high pressure (up to 10,000 psi), high temperature (up to 200˚C) triaxial loading system that enables long-term (days to months) laboratory experiments simultaneously on multiple core-scale samples under temperature, flow, mechanical stress, and chemically controlled conditions. We also used the system for measurement of permeability of granite samples obtained from the Grimsel Underground Research Laboratory (URL). Rate-dependent strength and creep tests of the samples for relatively long time (up to ~1 week) were planned, but delayed due to the COVID-19 pandemic.

Section 3 of the report describes the results of research activities conducted by LBNL researchers jointly with members of the science team of the "Collisional Orogeny in the Scandinavian Caledonides" (COSC) project. Field tests were conducted in the 2.5 km deep COSC-1 borehole in central Sweden to obtain flow characteristics of crystalline basement rock. An innovative downhole fracture characterization device, the Step-rate Injection Method for Fracture In-situ Properties (SIMFIP) tool, was installed in the borehole COSC-1 for real-time measurements of 3D mechanical displacements within borehole intervals, containing one or more fractures, together with measurements of the injection water flow rate, pressure, temperature and water electrical resistivity. Our team previously used Flowing Fluid Electrical Conductivity (FFEC) logging to identify hydrologically transmissive fractures in this borehole (e.g., Tsang et al., 2016; Doughty et al., 2017) and to link the identified flow zones with fractures observed on the image logs and core samples. The transmissive zones that were identified by the FFEC logs are quite extensive (over 1 m long) in many cases, and there are multiple fracture/foliation features that may correspond to the inflow zones. In this report, we describe the results of tests conducted to characterize three specific intervals within the COSC-1 borehole, using the SIMFIP tool. Tests were conducted to characterize three zones -- a zone with a flowing fracture, a zone with a mineralized (sealed) fracture, and a zone of mainly intact rock. These three zones were located in the borehole at a depth of ~0.5 km. Modeling of the SIMFIP data was conducted to simulate stress data using two approaches – an inversion of the displacement data, using the approach of Kakurina et al. (2019 and submitted), and a fully coupled hydromechanical analysis of fracture movements using the numerical modeling code 3DEC, which employs the distinct element method. We also present the results of updated laboratory and modeling studies conducted to characterize hydraulic properties of

crystalline rock cores from the COSC-1, which were determined using a unique laboratory-scale apparatus developed at LBNL. This apparatus was used to measure multi-directional transmissivity of core samples, collected at selected intervals in the COSC-1, and the results can be used to assess fracture anisotropy under confining stress conditions. To validate the results of laboratory-scale tests, we used synthetic core samples and a newly obtained core sample from the flowing fracture interval that was tested by the SIMFIP in the field.

2. LONG-TERM LABORATORY EDZ CHARACTERIZATION TESTING CAPABILITY DEVELOPMENT

2.1. Introduction

The strength and failure of rock is time dependent (Lajtai et al., 1991). The strength, geophysical, and hydrological properties of the rock surrounding the tunnel will change with time, affecting the evolution of Excavation Damaged Zone (EDZ), which may lead to a tunnel collapse (Bieniawski, 1989). After the emplacement of a bentonite backfill, the microcrack growth within EDZ is impacted by a number of factors including stress, temperature, water activity, capillary processes, chemistry, and mineralogy, which exhibit time-dependent, complex interaction. Understanding these processes and predicting the long-term performance of the rock surrounding a drift tunnel is critical for ensuring the safe storage of spent nuclear fuel and wastes.

In FY20, we have continued the development of a dedicated laboratory method to conduct long-term (days to months), temperature-controlled (up to ~200˚C) flow, mechanical, and chemical experiments simultaneously on multiple core-scale samples. Preliminary laboratory tests were used to characterize some fundamental properties (i.e., porosity and permeability) of granite core samples obtained from the Grimsel URL, Switzerland. Later in FY20, we will also conduct experiments to investigate (1) a time-dependent failure of rock subjected to a constant stress (i.e., static fatigue or creep experiment), and (2) a loading-rate dependent strength and its impact on the failure mode (i.e., ductile vs. brittle), both under the influence of elevated temperature, and, particularly, of the fluid chemistry. Additionally, we will conduct post-experiment characterization of the rock samples, which will include determination of the impact of long-term loading on changes in the acoustic (seismic) properties, and to evaluate the feasibility of using geophysical techniques to monitor *in-situ* rock property changes.

2.1 Designing and construction of a dual-sample triaxial rock testing system

In this section, we will describe the key components of the fabricated test system, including (1) the pressure vessels and a load frame, (2) hydraulic plumbing and a stress control system, (3) a temperature control system, and (4) strain measurement system.

2.1.1 Test system

The baseline characteristics of the developed test system are:

- Tested rock core size is 3.8 cm in diameter and up to 10 cm in length,
- Confining pressure is up to 10,000 psi (~70 MPa),
- Axial stress is up to ~29,000 psi (200 MPa),
- Temperature is up to 200˚C, and
- Two core samples can be tested simultaneously.

The schematic of the design of the test system is presented in Figure 2-1a. Figures 2-1c shows fabricated end plugs with a Viton jacket (TEMCO/CoreLab, OK) used for holding the core samples. A 3.8 cm diameter core with a maximum length of 10 cm is jacketed in a Viton sleeve, and the interfaces between the core plug and the top piston plug and also the bottom pedestal are sealed by the jacket. The core sample, jacket, top and bottom end plugs are housed in a cylindrical Grade-23 titanium hull (Figure 2-1b). A previously fabricated loading frame (Figure 2-1b) is used to apply and control the axial stress.

a. Design drawing

b. Single unit of assembled system

c. Top and bottom end plugs with jacketed cores

Figure 2-1. (a) A schematic of the high-temperature triaxial test system. This system (excluding plumbing for axial and confining stress fluids and pore fluid flow) has the following main parts: a confining cell consisting of Grade-23 titanium hull (shell), flanges, end plugs, and an external loading frame. A hydraulic ram (jack) is used to apply axial stress to the sample in the vessel. (b) The photos of assembled single unit of the vessel along with the load frame and the hydraulic rams, and (c) the fabricated top and bottom end plugs held together with a Viton jacket holding a core sample

2.1.2 Hydraulic plumbing and stress control

The confining stress and axial stress of each unit of the dual rock testing system are controlled independently by units of high-pressure (up to 12,000 psi [83 MPa]), and two-cylinder syringe pumps (Vindum Engineering VP-12K-SS) (Figure 2-2). The two cylinders of these pumps can be operated independently, and can be refilled automatically with a minimal impact from pressure and volume perturbations during valve operation, which cannot be avoided for recharging fluids. Because we anticipate that the elastomeric (typically Viton) part of the heated sections of the test system degrades quickly when exposed to hot water at temperature above 150 °C, we plan to use silicone oil as the confining fluid, and hydraulic oil in the hydraulic ram. In order to avoid contamination of the syringe pumps with oils, we have installed a series of transfer cylinders so that the oil pressure and flow can be controlled using water in the syringe pumps.

Figure 2-2. The high-pressure syringe pumps used for confining and axial stress control.

Figure 2-3a shows a schematic of the hydraulic plumbing, which includes (1) a control and data acquisition system, (2) a front fluid control panel, and (3) a load frame and pressure vessels. Using two dual-cylinder Vindum pumps, the confining and axial stress for each unit can be controlled independently. After preparation, the pumps can be controlled and the pressure, volume and a pumping rate are monitored remotely through a PC using a designated software. The front fluid control panel was assembled using stainless steel tubing rated at 12,000 to 60,000 psi to satisfy the test pressure requirement. High-pressure valves and fittings were used at a rated pressure of 60,000 psi from High-Pressure Equipment (HiP) parts, which provide secure pressure connections minimizing leakage. The panel consists of four high-pressure transfer cylinders for using oils (silicone and hydraulic) to control confining and axial stress. The upstream of each cylinder is connected to a pressure relief value set at 9,500 psi in case of over pressurization. The downstream of each cylinder is connected to a fluid reservoir via a 3-way coupling with a valve, so that the fluid depleted during initial setup and during a loading test can be refilled. During the test, the valve is closed to disconnect the fluid reservoirs (ambient pressure) from the rest of the system. The downstream of each cylinder is also connected to either the hydraulic ram (for axial stress) or the pressure vessel (for confining stress), depending on its function. To prevent over pressurization, we also implemented four pressure relief values at the upstream of each hydraulic ram and pressure vessel. Figure 2-3b shows a photograph of the system.

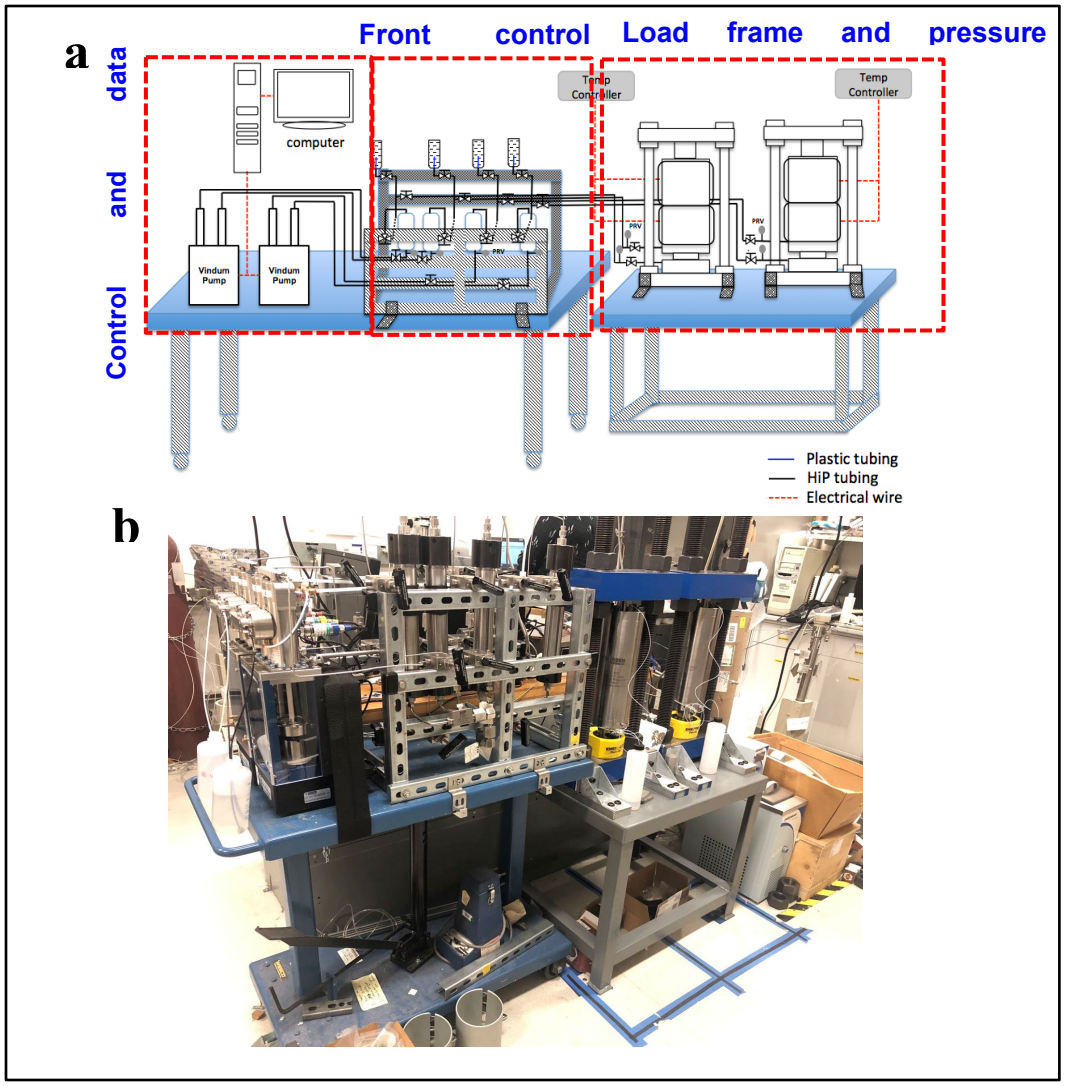

Figure 2-3. A schematic (a) and a photo (b) of the hydraulic plumbing system for the core-scale rock tests.

2.1.3. Temperature control

The temperature of the pressure vessels will be controlled using four rings of mica band heaters (Marathon/Western Thermal MISC 503-3) with fiberglass insulation. Both internal and external temperature of the pressure vessel will be monitored and controlled using temperature regulators. While the pressure vessel can be heated up to 200˚C through the mica band heater, the bottom hydraulic ram requires the temperature not exceeding 40˚C, because of possible seal damage. We adopted a cooling circulation bath with a U-shape cold plate to maintain a low surface temperature of the hydraulic ram. Figure 2-4 presents the temperature control system, both for heating the vessel and for cooling the bottom hydraulic ram (the yellow block). A proper heating insulation is required to maintain a high temperature difference, high mechanical strength, and to fit into the frame aperture without making the test assembly mechanically unstable.

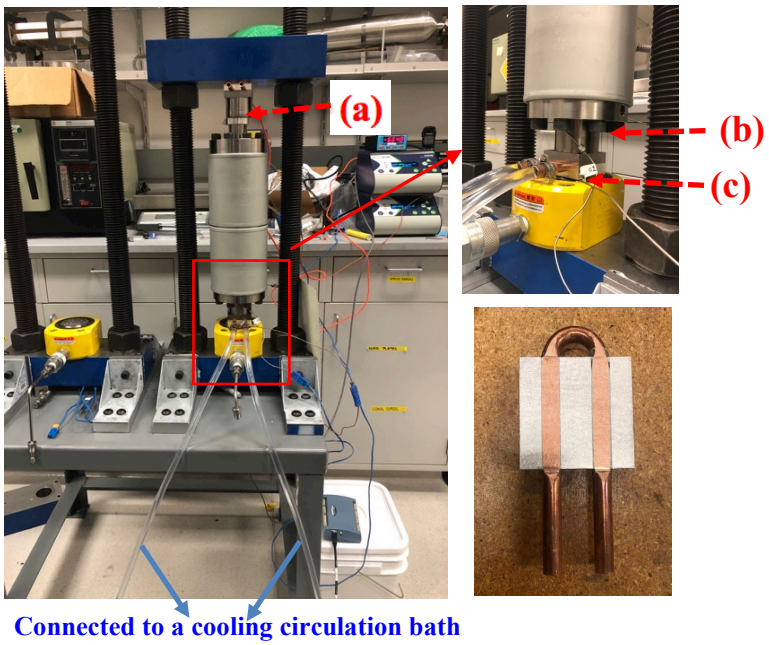

Figure 2-4. A temperature control system that includes two mica band heaters, U-shape cooling plates connected to a water circulation bath (chiller), a Grade-5 Titanium rod for thermal insulation between the vessel and the cooling plate. The symbols (a), (b) and (c) mark the locations of later-mentioned temperature measurement in which the heating band temperature was controlled at a range of temperatures up to 100°C.

After an extensive survey of the mechanic and thermal properties of different materials, we selected a high-strength Grade-5 Titanium rod (2''diameter) for heat insulation. The grade 5 titanium has a high mechanical strength (120,000 psi yield strength), and a low thermal conductivity at 7.2 W/m·K. The thickness of the rod was designed based on the heat load and the thermal impedance of the cold plate + circulation system.

The heat load Q induced is calculated via

$$Q = k\Delta TA/H \tag{2-1}$$

where k is the thermal conductivity (7.2 W/m·K), ΔT=160 K is the temperature difference, A=0.002 m^2 and H are the surface area and thickness of the insulation block, respectively. The thermal impedance is the sum of the thermal resistance of a material. For the cold plate, it was calculated by the following equation:

$$\theta = (T_{max} - T_{out}) * (A'/Q) \tag{2-2}$$

where T_{max}=40°C is the maximum desired surface temperature of the cold plate, A'=3.27×10^{-3} m^2 (5.0625 inch^2) is the surface area, and T_{out} is temperature of water leaving the cold plate, which is calculated as

$$T_{out} = T_{in} + \frac{Q}{\rho \upsilon C_p} \tag{2-3}$$

where T_{in} is the water temperature at the inlet of the cold plate, which will be marinated at 15° C by the fluid circulated by the cooling bath, ρ, υ and C_p are water density (1 g/cm^3), circulation rate (maximum at 350 mL/s) and specific heat (4.2 J/g·°C). Combining Eqs. (2-2) and (2-3), we were able to calculate the

impedance (θ) and plot its relationship with the thickness (H) of the insulation block. Figures 2-5a and b show the calculated relationships of heat load and thermal impedance vs. block thickness.

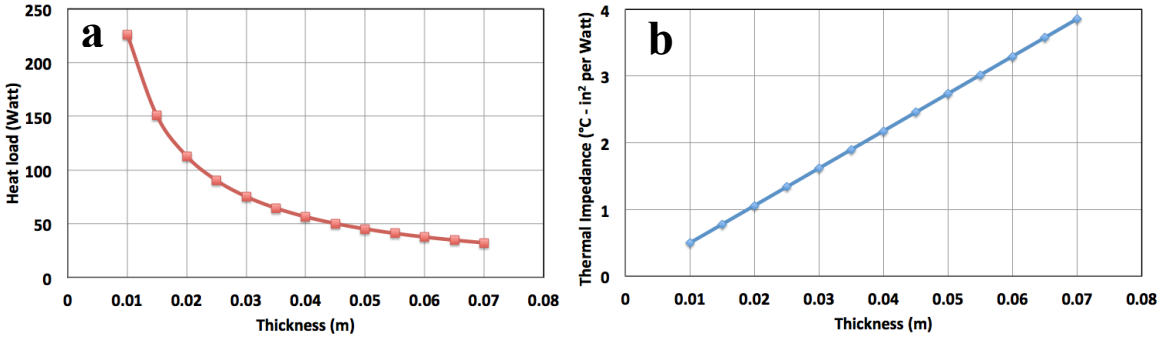

Figure 2-5. The relationship of heat load (a) and thermal impedance (b) vs. the insulation block thickness calculated from Eq. (2-1) and (2-2).

The calculated thermal impedance shown in Figure 2-5b can then be compared with the thermal impedance vs. water circulation rate for different cold plates shown in Figure 2-6. Any plate could be adopted only when its plots is below the thermal impedance required from Figure 2-5b. We selected the CP10 2-pass plate, which meets the performance requirement only when the thermal impedance in Figure 2-7b is higher than 2 °C· in^2/W, and the block thickness is >0.04 m. Note that our cooling bath has a maximum circulation rate of 5.5 gallons/min, which will ensure satisfying the performance requirement because the characteristic curve for CP10 2-PASS in Figure 2-6 decreases with increasing water circulation rate. After this analysis, a 0.05 m thick Grade-5 Ti block was used for thermal insulation between the heated high-pressure vessel and the cold plate.

To verify the performance of the actual system experimentally, we turned on the mica heater bands and maintained the temperature of the gap between the bands and vessel surface constant up to 100°C. Three thermocouple sensors were installed at different locations: (a) on the surface of the top piston plug, (b) at the bottom of the vessel, but above the insulation block, and (c) beneath the cold plate on the surface of the hydraulic ram. Figure 2-7 displays steady-state temperature measured by the three thermocouple sensors at a range of elevated temperatures. Note that the temperature on the hydraulic ram surface was successfully kept as low at 18°C, even when the heating temperature was increased to 100°C. We can reduce the temperature further if necessary by lowering the chiller temperature (e.g., from the current 15 to 4°C) to ensure the surface temperature of the hydraulic ram is maintained below 40°C when heating temperature is increased to 200°C. We will also adopt the same method for thermal insulation between the loading frame and the top piston plug, although the required insulation performance is not as strong as the bottom interface.

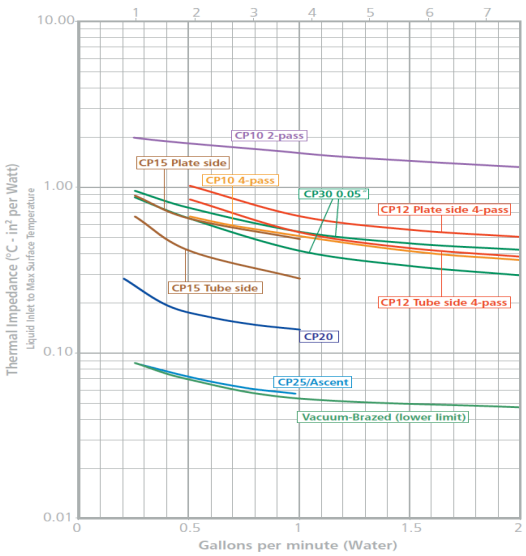

Figure 2-6. The diagram of thermal impedance vs. water circulation rate showing the capability of the cooling plate from https://www.boydcorp.com/thermal/liquid-cooling/liquid-cold-plates.html (Note we adopted the CP10 2-pass mode).

.

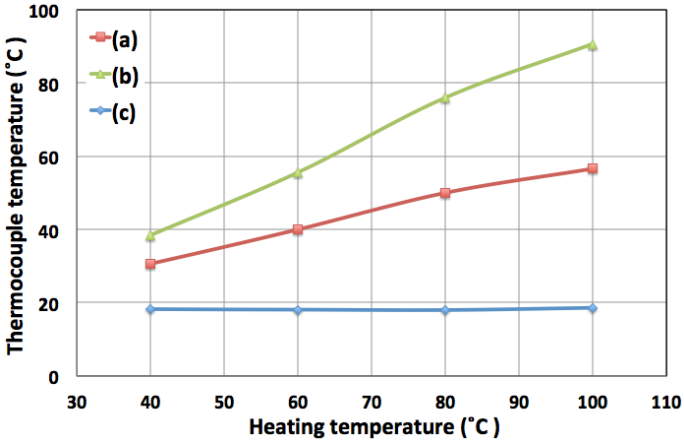

Figure 2-7. The temperature changes monitored at different locations of the vessel vs. the heating temperature. The locations of thermocouple senor (a), (b) and (c) are shown in Figure 2-4.

2.1.4. Strain measurements

The axial strain of the sample will be measured using a high-precision Linear Variable Differential Transformer (LVDT) sensor (RDP Electrosense, PA) at a resolution of 0.001% of the full scale (i.e., 0.1 micron over a +/-1 cm range) (Figure 2-8a). Note that each pressure vessel is also equipped with 20 electrical feedthroughs (five Kemlon 16-B-02924-00 4-pin PMS connectors) (Figure 2-8b) for internal sensor installment. For example, these sensors include temperature sensors and strain gages for circumferential strain measurement, giving extendable capability of the system if more monitoring is needed. All these sensors were connected to a data acquisition box (16 measurement channels and 2 analog

and record the measurements together with the pump volume and pressure data, using a software for operating the Vindum syringe pumps.

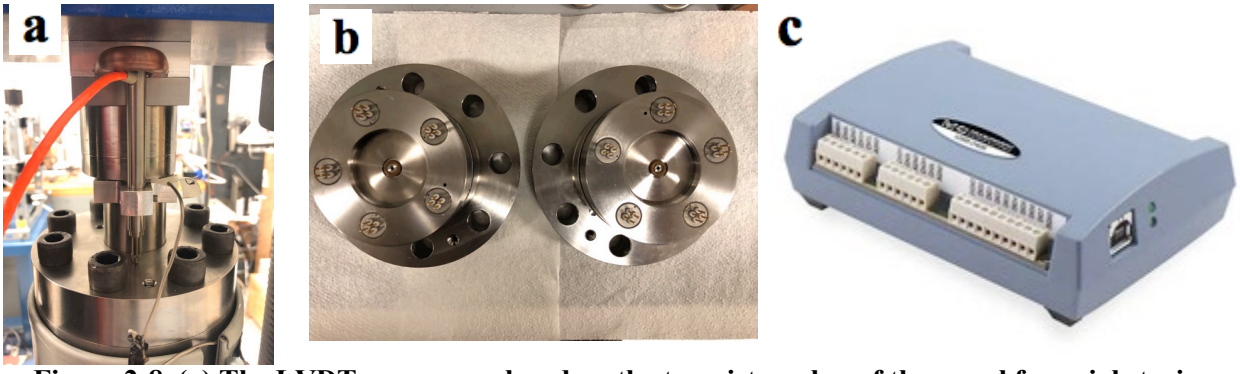

Figure 2-8. (a) The LVDT sensor emplaced on the top piston plug of the vessel for axial strain measurement. (b) The five feedthrough ports at the bottom pedestal that allow for maximum 20 electrical feedthroughs. The ports can be modified and fabricated for other sensing purpose. (c) The data accusation box for simultaneous external data monitoring along with Vindum pump control and monitoring.

2.2. Sample preparation

We obtained two large disk (slab) samples from the Grimsel URL. The sampling location, shown in Figure 2-9a, is BK cavern, where the formation rock is highly fractured (Bossart and Mazuret, 1991). The borehole (drill bit diameter of 300 mm) was drilled with a plunge azimuth of 178° (almost N-S trending) and was slightly upward plunging (Figure 2-9b). The provided two rock disks were cut from the original large core at drilling depths of 0 to 10 cm and 250 to 257 cm from the wall surface (Figure 2-9b). The rock showed strong foliation and coarse grains up to ~1 cm in size (Figure 2-9c).

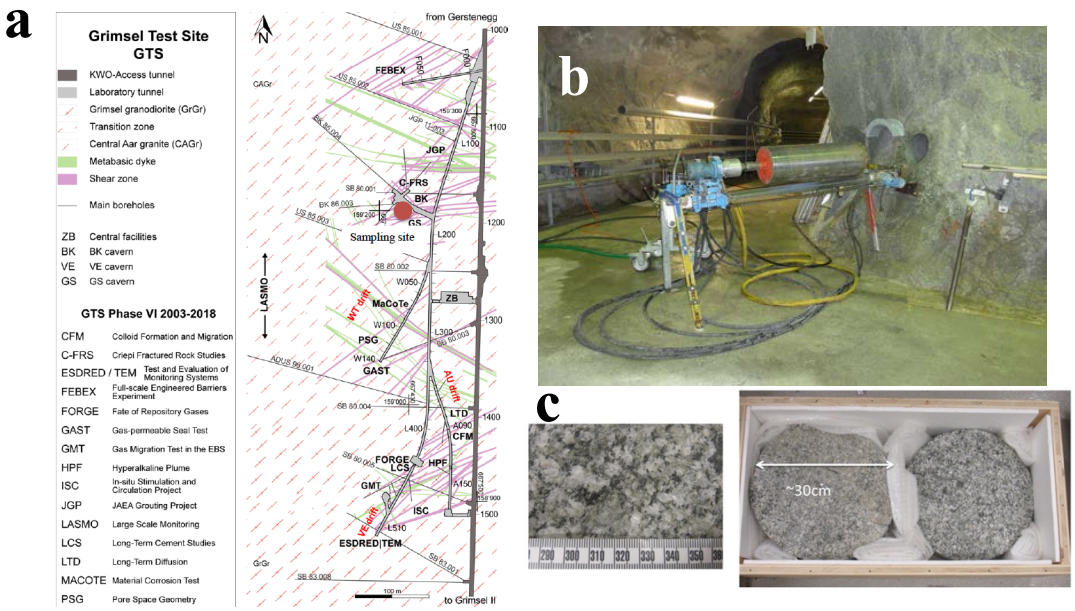

Figure 2-9. (a) The sampling site (marked by the red dot) at the Grimsel Test Site, (b) the photo of the drilling large rock blocks at the tunnel wall, and (c) photographs of large field cores (slabs) obtained from Grimsel URL (Courtesy of Kober Florian, NAGRA).

Ten rock core samples (with a diameter of 3.8 cm and a maximum length of 10 cm) were extracted from one of the slabs, perpendicular to the borehole drilling direction, and the coring direction is parallel to the vertical, maximum principal stress (Figure 2-10). The end faces of eight cores were sawn flat, and grounded smooth along with the sides. The fresh cut surfaces present clear foliations that are parallel to the long axis of the cores. Extra caution was taken to ensure that the two end surfaces were perpendicular to the sides as closely as possible. The machined cores were characterized for bulk density, porosity, and permeability.

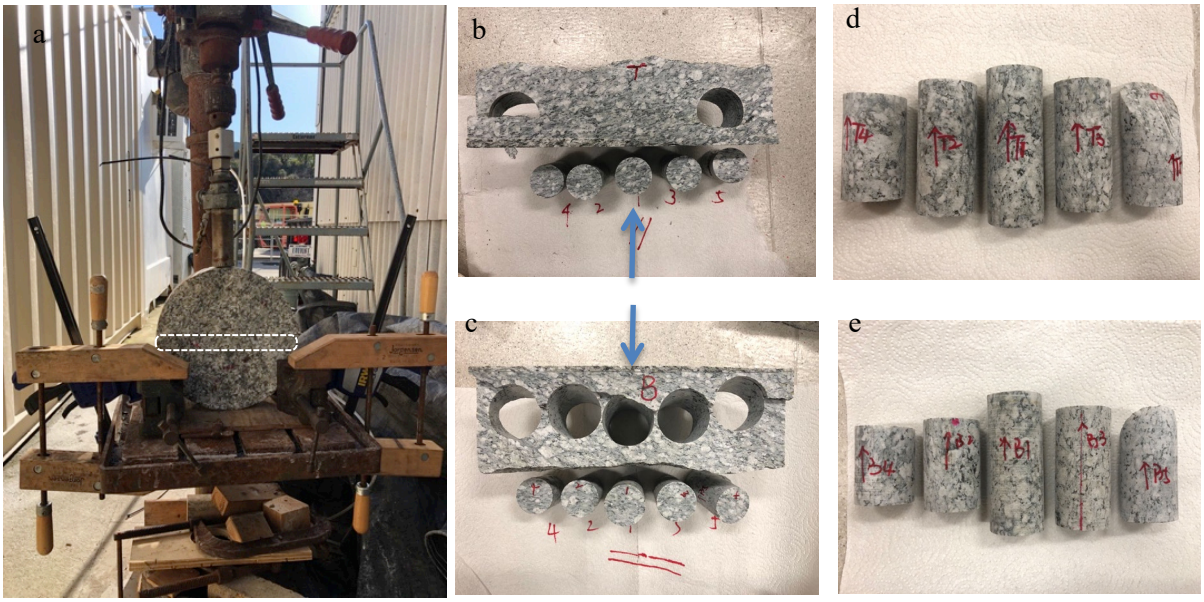

Figure 2-10. (a) Photograph of the coring operation of the rock slab from the side in the vertical direction. The slab was cut into two pieces (marked by T and B for top and bottom in (b) and (c)) along the white dotted box, leaving a rectangular piece in the middle. (b), (c) also show the clear foliations parallel to the long axis of the cores. (d) and (e) present the ten cores fabricated at 3.8 cm diameter and 5-10 cm long. The blue arrows in (b) and (c) mark the drilling direction at the field site.

2.3. Porosity and permeability measurements

The laboratory testing system was used to determine the porosity and permeability of the granite samples. The rock cores were first oven dried and weighed for dry mass, then submerged under water and connected to vacuum at -101 kPa. We vacuum-saturated the samples at different length of time, with an aim to fully saturate the samples by comparing the mass change vs. vacuum time. Figure 2-11 shows the porosity calculated from the volume of each core sample and mass change (by weighing) after vacuuming for 3 and 6 hours. Note the small variations of porosity measured from vacuuming of 3 and 6 hours (<0.021%). After 6 hours of vacuuming, the porosity of the eight core samples varies from 0.5% to 0.6%, similar to the measurements from Keusen et al. (1989).

Before the permeability tests, a series of leakage tests was conducted on the lab system. The system, excluding the pressure vessels, was filled by water in the hydraulic lines and presurized to 2,000 psi by the Vindum pumps, and the pressure was held constant for 3 days. The volume changes of the pumps were monitored to quantify any leakage of the system. Over the 3 days, the volumes of the four pump cylinders (two for confining stress control and two for axial stress control) fluctuated from -0.018 mL to 0.044 mL relative to the initial value, with no continuous decrease in volume observed. This indicates a good hydraulic sealing of the system and the small volume variations (espectially for the negative changes) may due to room daily temperature changes. The high pressure vessels were pressure tested to check for leakage. This was conducted independently by the manufacturer/vendor (Vindum Engineering Inc.) before the vessels were delivered to the lab.

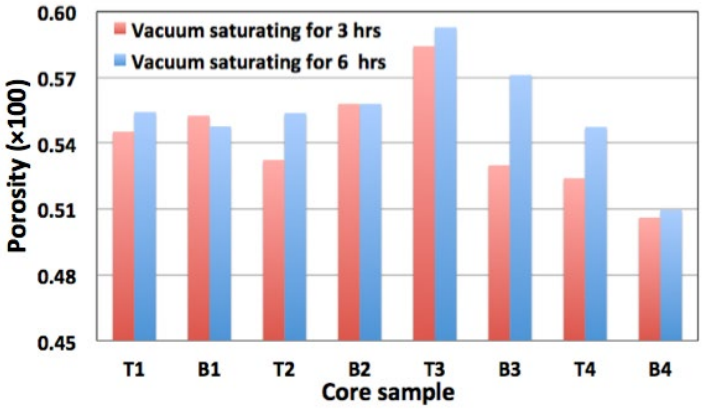

Figure 2-11. The porosity calculated for core samples based on the results of saturation under vacuum for 3 and 6 hours.

After the leakage test, the lab system was used to conduct permeability measurements on Samples T2 and T3 (with the same length of 8.4 cm) under room temperature and without axial loading (see Figure 2-3b). Water-saturated cores, jacketed with a Viton sleeve and assembled together with end plugs, were emplaced into vessel shells. The remaining space of the vessel chambers and the system pipelines was filled with the deionized (DI) water. Finally, the confining pressure for both vessels was increased to 900 psi and held constant. For Sample T2, stepwise constant flow rate water injection was performed, and the differential pressure was measured along the core. An ambient pressure was maintained at the outlet of the core thus the differential pressure equals to the injection pressure applied at the inlet. Figure 2-12 shows the measured confining pressure and the differential pressure vs. injected water volume (PV refers to the pore volume) at (a) 0.01 mL/min, (b) 0.0075 mL/min, (c) 0.005 ml/min, (d) 0.001 mL/min, and (e) 0.0005 mL/min. The average differential pressures at the steady states were computed and are plotted against applied differential pressure in Figure 2-14a. During the permeability tests (~1 week), the volume change was <0.1 mL in both pumps providing constant confining pressure.

For Sample T3, we first conducted the same constant-rate injection tests. However, the inlet pressure showed a quick increase, and it then exceeded the confining pressure before reaching a steady state. When the injection pressure exceeded the confining pressure, it could have created near-wall flow, leading to overestimated permeability. Thus, instead of using the constant-rate injections, we performed constant-pressure injection tests, and monitored the flow rate changes as a function of time. Figure 2-13 shows the flow rate changes as a function of time at applied differential pressure of (a) 150 psi, (b) 300 psi, (c) 375 psi, (d) 450 psi, (e) 560 psi, and (f) 675 psi. These injection pressures were maintained lower than the confining pressure to avoid any near-wall flow. The average flow rate at the steady state was also obtained and plotted against applied differential pressure in Figure 2-14b.

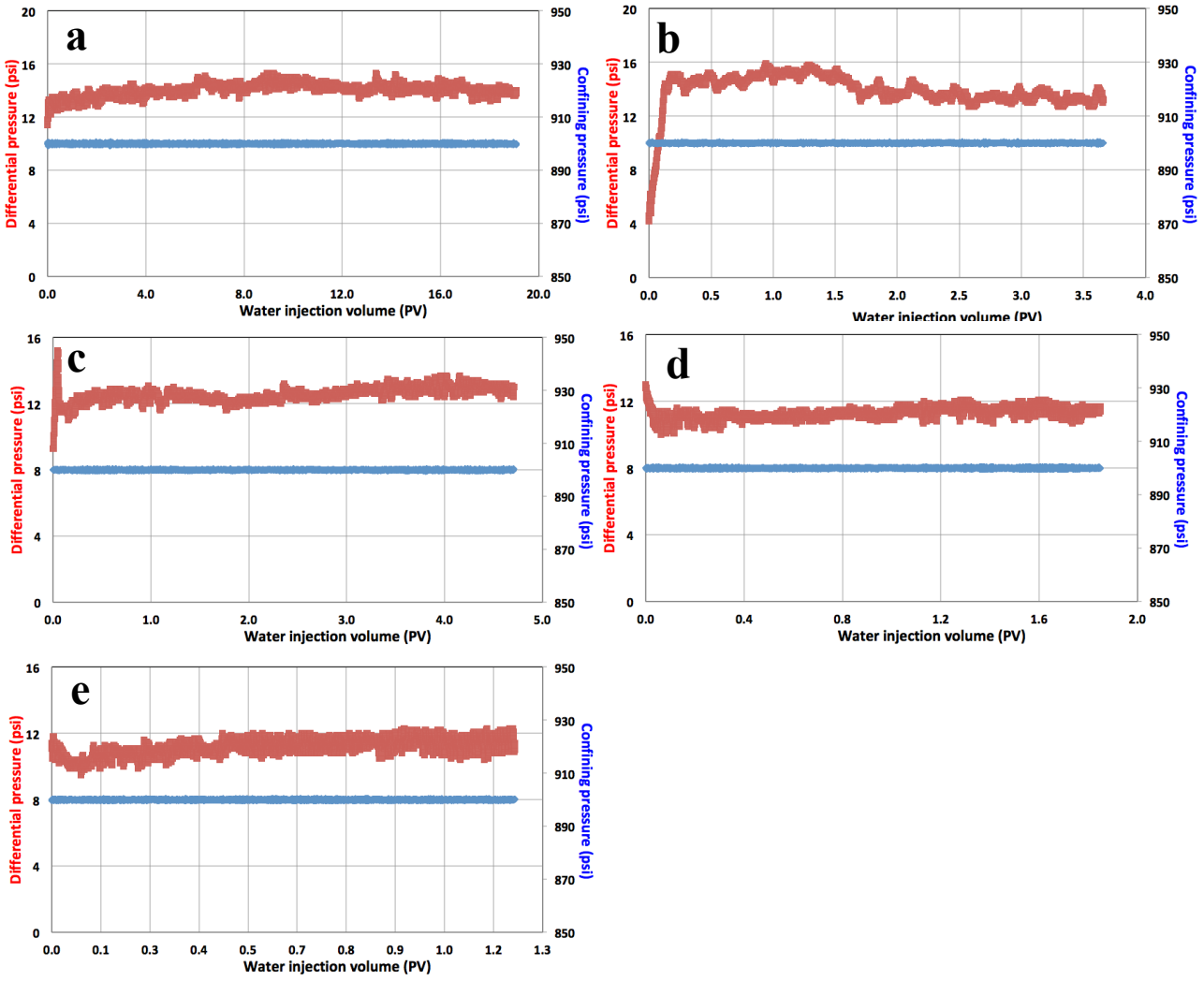

Figure 2-12. The confining pressure and differential pressure vs. injected water volume (PV refers to the pore volume) in Sample T2 at (a) 0.01 mL/min, (b) 0.0075 mL/min, (c) 0.005 ml/min, (d) 0.001 mL/min and (e) 0.0005 mL/min. The pressure data was recorded at every 5s. The confining pressure (marked by the blue lines) was maintained constant at 900 psi in each test.

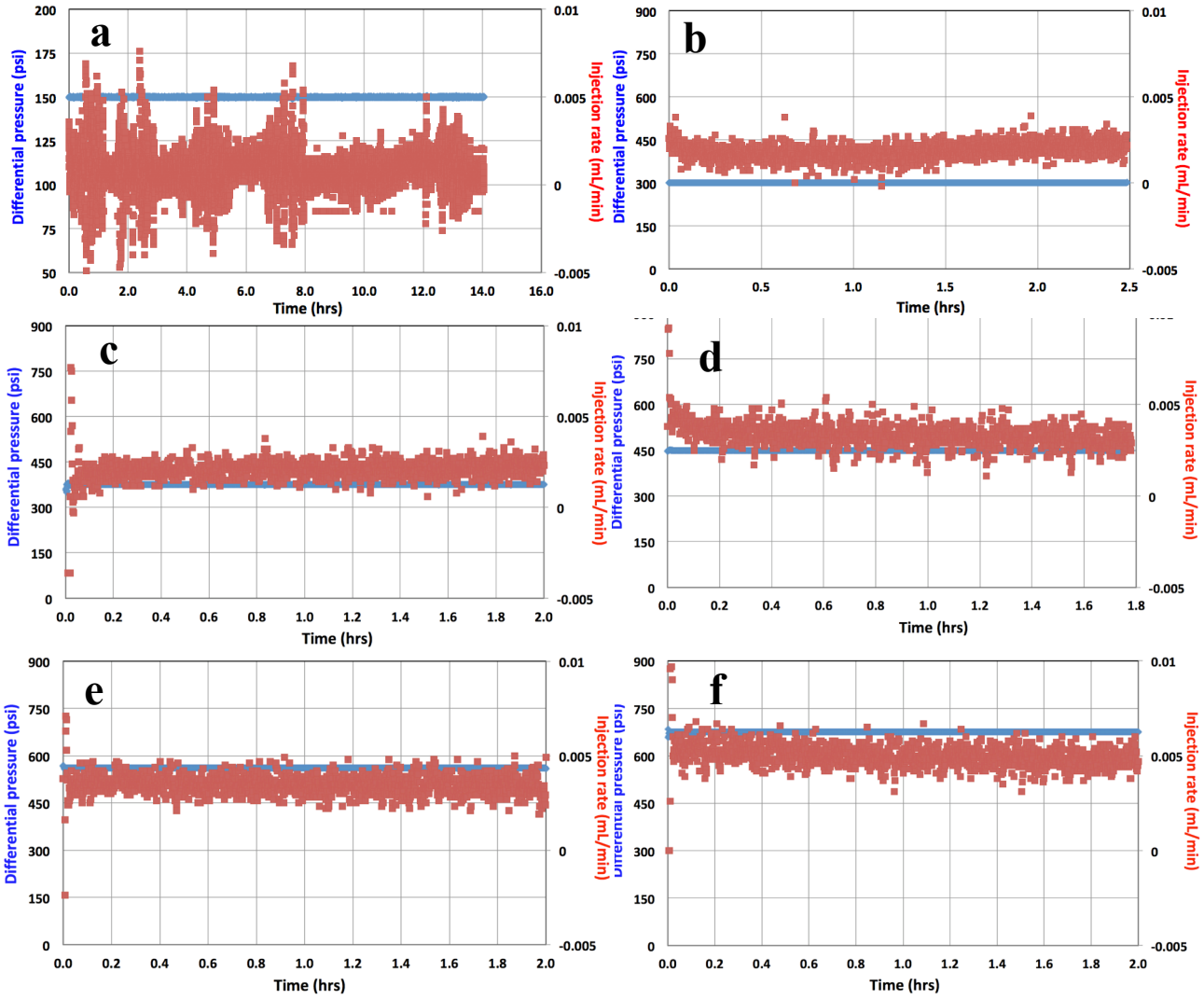

Figure 2-13. The injection rate variations as a function of time at applied differential pressure of (a) 150 psi, (b) 300 psi, (c) 375 psi, (d) 450 psi, (e) 560 psi and (f) 675 psi. Both pressure and injection rate were recorded at every 5s.

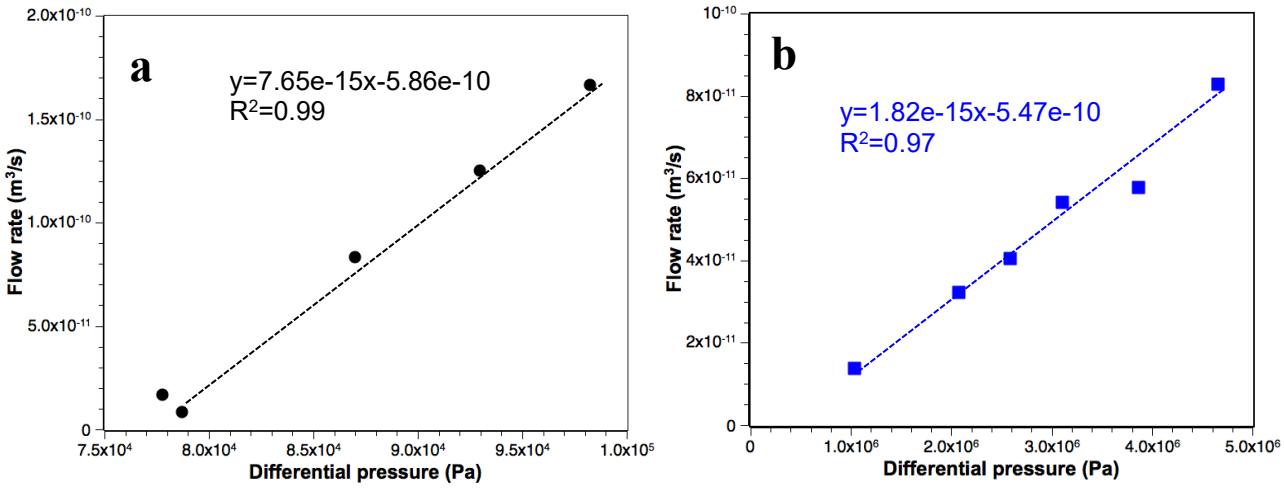

Figure 2-14. The relationships of flow rate vs. differential pressure at the core inlet and outlet for Samples T2 (a) and T3 (b). Note the pressure and flow rate data were converted to Pa and m^3/s to calculate permeability. Each data point was averaged over the stable different pressure and flow rate shown in Figures 2-12 and 2-13.

Based on the linear relationship between the flow rate and the differential pressure, shown in Figure 2-14, the flow process in cores can be described using Darcy's law given by

$$\frac{Q}{\Delta P} = k\frac{A}{\mu L} \tag{4-4}$$

where k is absolute permeability (m^2), A is the cross-section area of the core (m^2), μ and L refer to the water viscosity at room temperature at 25 ˚C (0.00089 Pa·s) and sample length (m), respectively.

The permeability values calculated using Eq. (4-4) are 504.3 and 1.2 μD for Samples T2 and T3, respectively. We compared our measurements with available data from K for Grimsel Granodiorite Benchmark (KG^2B) (David, 2018a, b), a collaborative benchmarking exercise for estimating the permeability of Grimsel granodiorite. In KG^2B, 24 laboratories were involved in measuring permeability of the rock under the same effective confining pressure (730 psi). The samples were obtained from a granite and granodiorite tunnel in the Central Aar Massif in Switzerland. Along the tunnel, major damage zones are located in meter-scale shear zones or widely spaced discontinuities caused by regional deformation. Two cores of Grimsel granodiorite, each about 1 m in length and 85 mm in diameter, were retrieved at a distance of 4–6 m from the tunnel wall of the Grimsel test site, far away from the EDZ. The cores were cut into small blocks at lengths requested by each participant (between 2 and 10 cm). These cores showed similar, visible grain shape and foliations parallel to the core axis (at an angle of about 20˚–30˚). From 35 independent measurements, an average permeability of 1.11 μD with a standard deviation of 0.57 μD was obtained. This result is similar to the permeability of Sample T2.

Note that we conducted tests of samples that were obtained within the EDZ (~2.5 m away from the tunnel wall). This may explain the unexpectedly high permeability measured for Sample T2. While both samples were obtained from the same large host rock block (~30 cm diameter), the two orders of magnitude difference in permeability indicates pronounced heterogeneity, and potential open cracks/fractures in Sample T2, which caused high permeability (although there is no visible crack/damage on the sample surface). Also note that during the experiments, water flow direction is parallel to the foliations of both samples (see Figure 2-10d) and the maximum principal stress, which would be the preferred orientation of tensile microcracks and fractures. We will conduct anisotropic seismic velocity measurements

independently to verify/compare any potential cracks/fractures in both samples. We will also produce thin sections of the rock and conduct detailed examination of the microstructures and foliations under the microscope. As an option, it may be informative to perform additional permeability tests and/or seismic velocity measurements using cores collected in directions perpendicular to the foliations to characterize the anisotropy.

2.4. Summary of the current status and plans for the remainder of FY20

We have developed a high pressure (up to 10,000 psi), high temperature (up to 200˚C) triaxial loading system to enable long-term (days to months) laboratory experiments of flow simultaneously on multiple core samples under temperature, mechanical, and chemically controlled conditions. We also used the system for permeability measurements of granite samples obtained from the Grimsel URL. We will conduct additional tests to better understand the mechanical, chemical and microstructural properties of the rock.

We will conduct rate-dependent strength and creep tests of the samples for relatively long time (up to weeks). Due to the COVID-19 pandemic and a shelter-in-place order, the originally planned creep tests have been delayed. We will resume the experiments as soon as the access to the laboratory is permitted.

This page is intentionally left blank.

3. CHARACTERIZATION OF TRANSMISSIVE FRACTURES IN CRYSTALLINE ROCKS

3.1 Introduction

Crystalline rocks are one of several potential geologic environments that have been considered for long term disposal of nuclear waste due to their inherent low permeability (e.g., Witherspoon et al., 1981; Bredehoeft and Maini, 1981). One key challenge in evaluating the safety case for crystalline rocks is that fractures present within these rocks may serve as transmissive pathways for radionuclide transport (Cherry et al., 2014). The 2019 update to the SFWST R&D roadmap identified that improved site characterization techniques are needed for crystalline repository systems, especially to characterize fractures and their hydrogeologic properties; such data are needed to develop accurate discrete fracture network (DFN) models (e.g., Follin et al., 2014; Hadgu et al., 2017). Such DFN models have been also used to model fluid flow for enhanced geothermal systems (Makedonska et al., 2020) and evaluate the potential for leakage from geologic CO_2 sequestration sites (Chen et al., 2019).

Our team at LBNL has been collaborating with the Collisional Orogeny in the Scandinavian Caledonides (COSC) scientific team to use the COSC-1 borehole as a testbed to evaluate fracture transmissivity within a crystalline basement environment. This borehole, located in central Sweden, was drilled to a depth of 2.5 km, and encountered a sequence of high-grade metamorphic rocks, such as felsic gneisses, amphibolite gneisses, calc-silicate gneisses, amphibolite, migmatites, and garnet mica schists, with discrete zones of mylonite and microkarst (Lorenz et al., 2015). Our initial work focused on using Flowing Fluid Electrical Conductivity (FFEC) logging to identify hydrologically transmissive fractures (e.g., Tsang et al., 2016; Doughty et al., 2017) and to link these identified flow zones to potential correlative fractures observed in image logs and core samples. During the 2019 field campaign (Guglielmi et al., 2019), we deployed the Step-rate Injection Method for Fracture In-situ Properties (SIMFIP) tool (Guglielmi et al., 2013; 2015) to test a suite of selected fractures within the COSC-1 borehole. Details of our field activities can be found in Appendix 1.

During the 2019 field study, we evaluated three different intervals within the COSC-1 borehole (Figure 3-1): 1) a gently dipping transmissive fracture at a depth of ~505.9 m, which is subparallel to foliation; 2) a steeply dipping cemented fracture located at a depth of ~515.1 m; and 3) an unfractured interval located at a depth of 485.2 m. Our team was able to leverage previous detailed characterization of the core and borehole, and use gamma log mapping to precisely locate the SIMFIP tool relative to the features that our team selected for testing. The transmissive fracture is located in an interval that had been previously identified as permeable by FFEC logging at ~506 m – three distinct fluid entry zones (at 504.6, 504.8 and 505.9 m depths) were identified using an *in-situ* conductivity probe (see Section 3.2). The other two zones that were examined did not have measurable transmissivity based on previous FFEC logging runs. The goal was to better characterize two distinct types of fractures (steeply dipping features and shallow dipping, foliation parallel fractures) and to also determine fundamental rock properties, stress orientation, and Sh_{min} values by creating a hydrofracture within an intact section of the borehole and modeling the results of these field tests (Sections 3.3–3.6). Our team obtained core samples that correspond with the tested depths for more detailed characterization in the laboratory – the preliminary results of these tests are presented in Section 3.7. Additional core characterization is planned, along with borehole televiewer logging of the COSC-1 borehole in the tested intervals to obtain fracture orientation data from the stimulated features. This field test represents the deepest borehole deployment of the SIMFIP tool (by a factor of 10) to date.

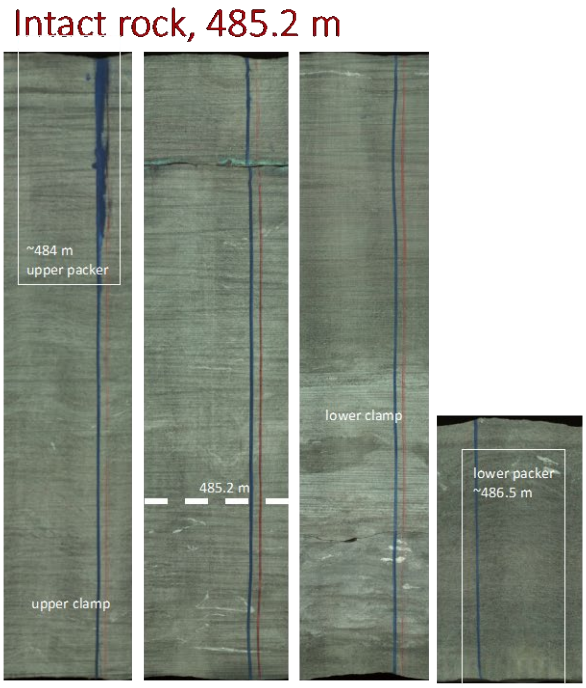

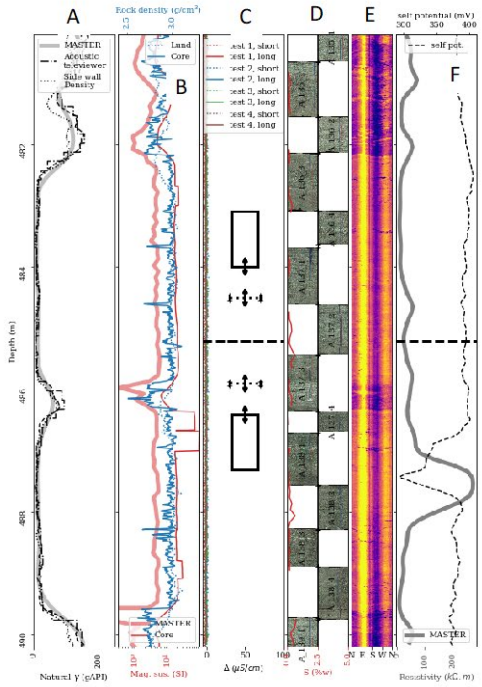

Flow zone 505.9 m Two to three flowing fractures 504.6, 504.8 and 505.9 m

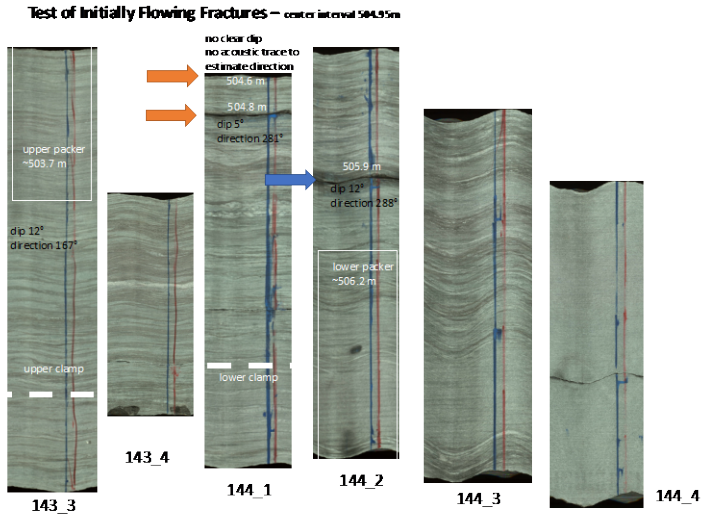

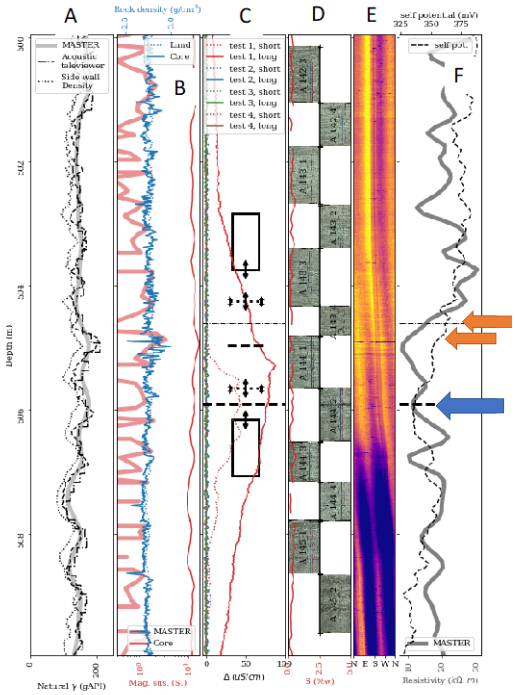

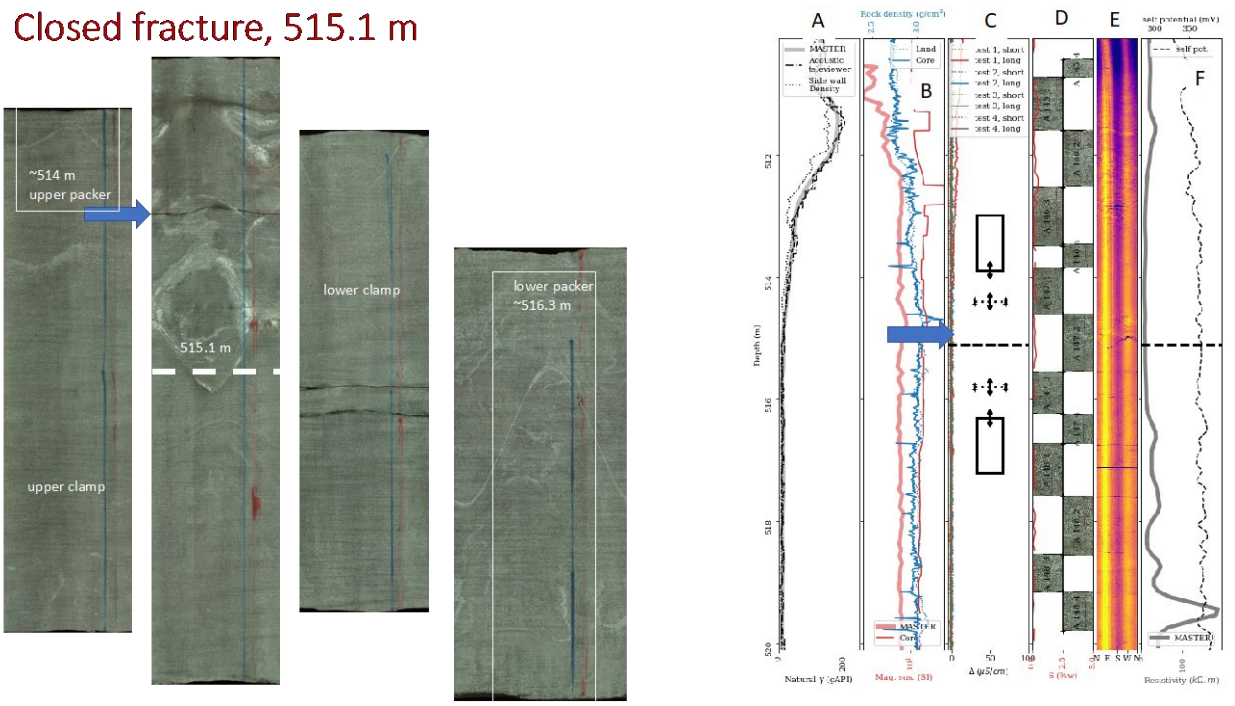

Figure 3-1. Composite logs of the three depths of 485.2, 505.9, and 515.1 m studied with the SIMFIP in the COSC-1 borehole during the 2019 field campaign. The left images represent core photos for each section, along with the locations of the packers and clamps from the SIMFIP tool. The geometry of the SIMFIP system (packers and clamps) is portrayed in Figure 3-2a. On the right, column A represents a suite of gamma log runs taken (these were used to help register the depth of the tool precisely), column B shows the magnetic susceptibility and rock density, column C shows the normalized conductivity values from FFEC logging (with positive changes indicating more saline and conductive fluids from formation waters being discharged into the dilute borehole), column D shows the unrolled core photographs along with plotted variations in S contents (wt. %) of the core samples, column E depicts the acoustic televiewer log image for the borehole interval (from Wenning et al., 2017), and column F depicts rock electrical resistivity and self-potential log measurements. Data from Dessirier et al. (submitted).

3.2 Detection of Flowing Fractures With A Distributed Water Resistivity Probe

3.2.1 Instrument setup and measurement protocol

The conductivity probe is attached to the upper part of the SIMFIP probe (Figure 3-2a). It consists of an array of 63 electrodes (originally 64) with 62 intervals of 10 cm each in between them, measuring electrical resistivity at regular time intervals by applying a voltage that is compared with a voltage across a resistor of known resistance (Figure 3-2b and c), hereby obtaining a continuous resistivity profile. An electrical conductivity sensor (EC) was integrated into the gamma logging tool that was lowered into the borehole together with the conductivity probe (Figure 3-2a). It provided actual conductivity measurements at a single point immediately above the conductivity probe, allowing for comparison of the conductivity data and transformation of the relative resistivity values of the probe into absolute conductivity values.

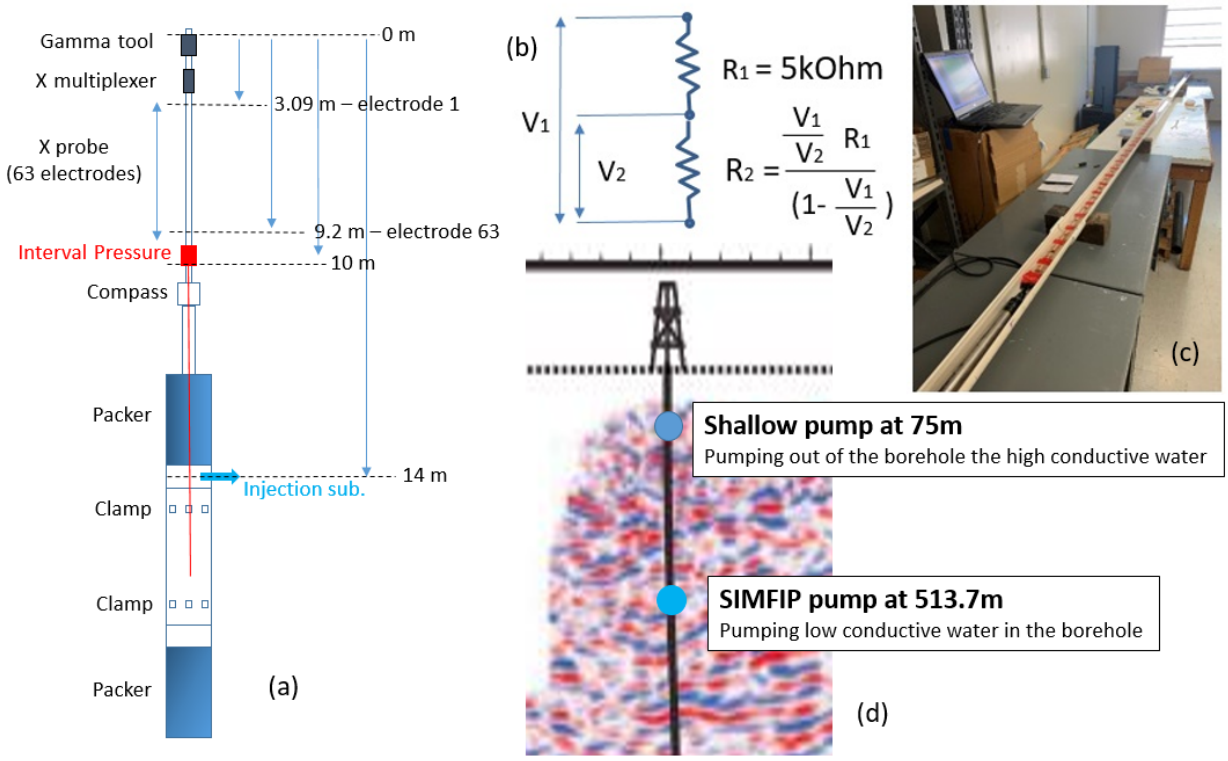

Figure 3-2. (a) – Schematic diagram of the SIMFIP probe including the resistivity probe and the gamma tool at the top (the gamma tool is used to localize the probe at depth). (b) - Concept of the resistivity measurement at each interval (R2) relative to a known resistance (R1) in the probe's control unit head. (c) - The 6.2 m long, 63 electrode probe laid out in a calibration trough. (d) – Deployment configuration of the resistivity measurement in the COSC-1 borehole (after Wenning et al., 2017).

The probe was deployed in the COSC borehole in order to profile the water resistivity between 502.87 and 509.07 m depth, a borehole interval where flowing fractures had previously been identified by FFEC measurements. After the probe was set at the interval and left to measure the conductivity of the present borehole fluid for a while in order to obtain a measurement baseline, freshwater from a nearby creek was pumped into the borehole 7.6 m below the probe (Figure 3-2d; also indicated by blue arrow in Figure 3-2a). In order to create a negative pressure gradient from the formation to the borehole, a shallow pump in the borehole at a 75 m depth was activated to draw down the hydraulic head in the borehole (Figure 3-2d). This was intended to stimulate flow of formation water out of flowing fractures into the borehole, where it could be detected by the conductivity probe.

Figure 3-3a shows the applied pumping rates at both depths and the borehole water pressure measured at the SIMFIP probe (Figure 3-2a for location of the pressure sensor in the probe). Freshwater injection below the conductivity probe started at 12:19 on June 16, 2019. At 13:20, the shallow pump at a 75 m depth was activated with a continuous pumping rate of 5 l/min. This operation introduced electric noise on the pressure sensor. At 13:48, the rate of the shallow pump was increased to 10 l/min, and the freshwater injection below the conductivity probe was ceased. At 15:01, the shallow pump achieved its maximum drawdown of 75 m and was turned off for ~25 min. At 15:25, the shallow pump was turned back on with a flow rate of ~6 l/min, which was lowered to 4.5 l/min at 16:13 to maintain a constant drawdown of 75 m. The conductivity measurement was terminated at 16:08. Figure 3-3b is a schematic explanation of the water circulation

induced in the borehole by the two pumps. Borehole initial water (dark blue color in Figure 3-3b) was replaced by fresh water (cyan blue color in Figure 3-3b) in a borehole interval much larger than the measuring zone. A part of the water was pumped out of the borehole by the shallow pump, but another significant part leaked in high permeability fractures intersecting the shallow borehole zone.

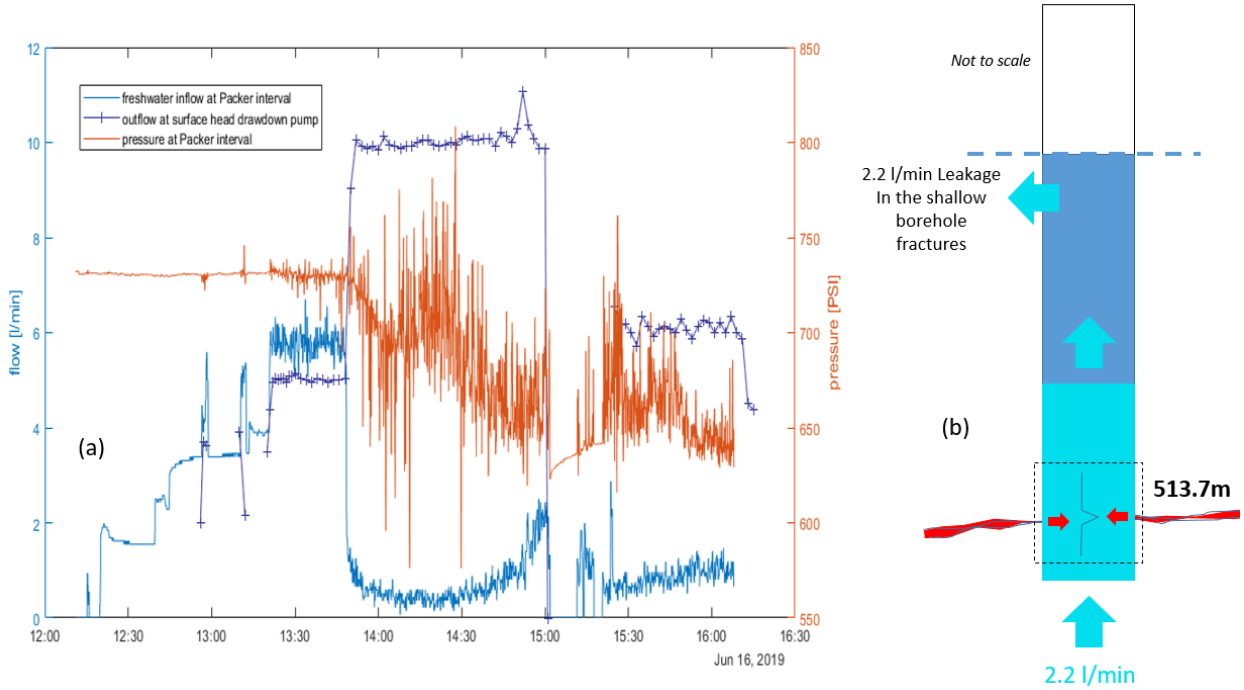

Figure 3-3. (a) – Injection freshwater flowrate, pumped borehole water flowrate and water pressure variations versus time; (b) – Water circulation in the borehole during the resistivity measurement.

3.2.2 Data processing

The raw data include a resistivity relative to a built-in resistor of 5kOhm, with 0 representing a perfectly conductive interval, and 1 representing a perfectly resistive interval between two contacts. Using the absolute conductivity measurement from the gamma tool, the relative resistivity measurements of the conductivity probe are transferred into absolute conductivity measurements in µS/cm. Variations of the measured conductivity along the probe due to the uneven placement in the borehole were corrected using baseline data collected prior to the test (when the probe was resting in an undisturbed column of water with an assumingly homogeneous conductivity).

After obtaining a baseline-corrected absolute conductivity value for each interval at every point in time, the data are analyzed along the time axis of the test (Figure 3-4). It can be seen that at the beginning at 12:53:29, roughly 30 minutes after the start of the freshwater injection, the higher conductive formation water was subsequently replaced by lower conductivity fresh water at each conductivity interval. However, at some intervals, a slightly higher conductive signal persists (Figure 3-4) for a time after freshwater was injected below, and before a large pressure gradient was caused by the shallow pump close to the surface. These "anomalies" for each interval were compared to similar water resistivity signals at a given time, and identified by previous FFEC tests and to borehole fracture locations observed on the acoustic logs (Figure 3-5).

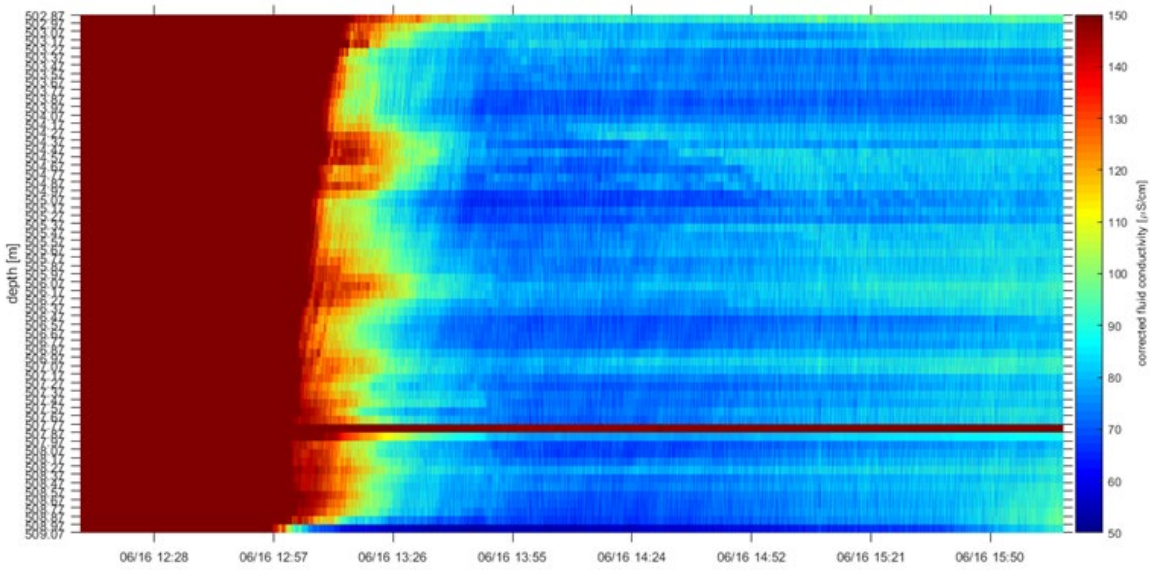

Figure 3-4. Borehole water absolute electrical conductivity variations with depth (vertical axis) and with time (horizontal axis)

3.2.3 Interpretation

After the borehole water was replaced with freshwater, but before the shallow pump was turned on to draw down the hydraulic head, a weak but consistent signal of persisting higher conductivities can be observed at two to three distinct interval regions (Figure 3-4). This is believed to be due to the presence of flowing fractures, allowing for a small inflow and diffusion of formation water into the borehole (Figure 3-3 and 3-5). Unfortunately, when the shallow pump was turned on in order to create a negative pressure gradient allowing for an increased inflow of formation water, it had the adverse effect of diminishing the signal. When the flowrate was turned up, the anomalies almost vanished. This is believed to be caused by the much stronger flow of freshwater past the probe, flushing the borehole completely with freshwater. However, the initial signal picked in the low-flow regime could be very well correlated with data from previous borehole logging, coring and FFEC measurements (Figure 3-5). Due to the high resolution of the distributed electrical resistivity measurements, 2 to 3 flowing fractures could be located within the broader resistivity anomaly.

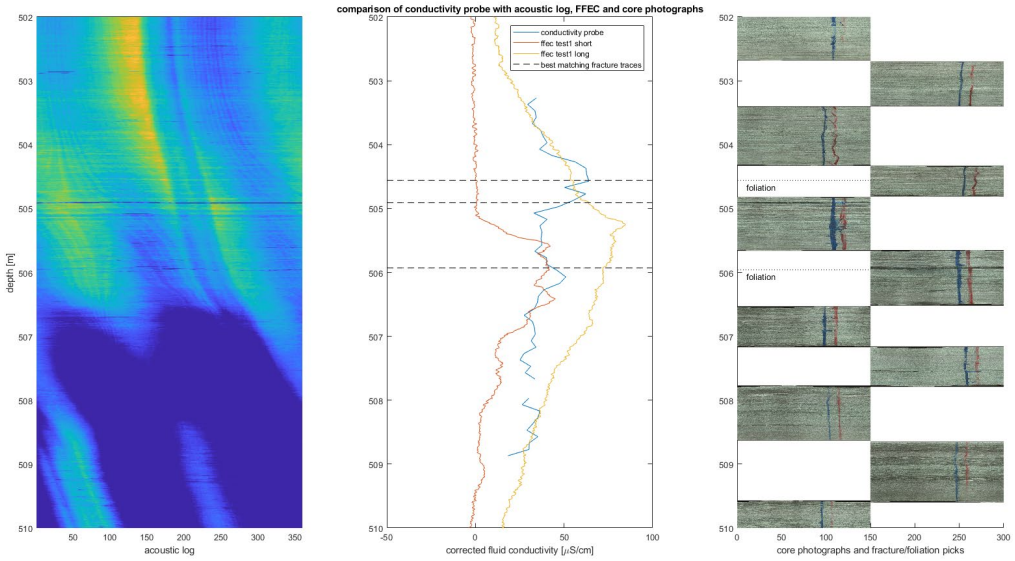

Figure 3-5. Left – Acoustic log showing traces of natural fractures; Middle – Borehole water conductivity variation with depth. The blue curve is the conductivity measured with the SIMFIP device. It is compared to conductivity signals captured by a moving FFEC probe in previous studies (Tsang et al., 2016; Doughty et al., 2017). There is a good correspondence of anomalies observed by the two methods. The SIMFIP conductivity may eventually show details, characterized by two to three conductivity peaks highlighting the possible existence of several flowing natural fractures. Right – Several fractures (denoted by dashed lines in center column) are observed on borehole cores at depths matching the observed conductivity anomalies.

3.3 In Situ Hydromechanical Testing of Fractures

3.3.1 Test setting and protocol

Three borehole intervals, each 2.41m long, have been tested:

- Test 1: An interval made of intact rock was selected between 484 and 486.4 m depth from the acoustic log observation in the field. Cross-checking with cores showed afterwards that this interval might be affected by two flat fractures at 484.9 and 486.2 m, with orientations roughly 247/13. These fractures appear sub-parallel to foliation. One is between the SIMFIP clamps, one is below the lower clamp.
- Test 2: Initially flowing fracture interval between 503.7 and 506.2 m depth. Flowing fractures were identified using a water resistivity measurement (Section 3.2) at 504.6, 504.8 and 505.9 m, respectively. This means that the two shallower fractures were between the SIMFIP clamps, while the deepest one is below the lower clamp. Fractures are relatively flat, more or less parallel to the foliation with dip direction and dip of 281/5 to 288/12, respectively.
- Test 3: Initially closed fracture between 513.9 and 516.3 m depth. No flow anomaly was observed in this interval in previous FFEC studies. This is why it is defined as affected by initially closed fractures, with one feature parallel to foliation (260-280/2-13) and the other representing a steeply dipping mineralized fracture (110/59). All fractures are located between the SIMFIP clamps.

The instrument used for the injection tests is a SIMFIP borehole probe, which allows for simultaneous measurements of fluid pressure and three-dimensional displacements at high frequency (Guglielmi et al., 2013; 2015). The injection interval is isolated in the open hole using two inflatable rubber packers, with sliding sleeves straddled by a steel mandrel. A 0.49 m long and 0.1 m diameter pre-calibrated aluminum cage located between the two packers is clamped onto the borehole wall. When clamped, the cage is disconnected from the straddle packer system. As discontinuities intersected by the borehole interval are deforming as a result of the fluid injection into the interval, the cage allows obtaining angle-dependent strain measurements that are used to constrain the full three-dimensional displacement tensor and the three rotations of the upper anchor of the cage relative to the lower anchor. The maximum displacement range of the deformation cage is 0.7 and 3.5 mm in the axial and radial directions of the borehole, respectively, and the accuracy is $\pm 5 \times 10^{-6}$ m. A compass set on the probe provides the orientation of measurements with 0.1° accuracy. Thus, in further analyses, the displacements can be rotated into a geographic reference frame.

The displacement data are continuously logged together with pump parameters (pressure and flow rate). The pressure sensors allow for measurements over a pressure range from 0 to 20 MPa, with a 0.01 MPa accuracy. The relation between the compliance of the probe and the elastic response of the borehole wall was studied extensively through laboratory tests. It is shown that the device is ~10 times more compliant than the rock, and that the orientation and magnitude of displacements below the stimulation pressure strongly depends on the elastic anisotropy of the rock and on the coupling between the probe and the borehole wall. In theory, there should be no SIMFIP response for a uniform inflation of the pressurized interval in isotropic intact rock. In the field, the SIMFIP probe is capturing an elastic response, which depends on the SIMFIP's clamp compliance and clamping efficiency, orientation of the cage in the borehole and on the borehole wall geological heterogeneity. These different effects are removed from the signal during a pre-processing phase (see below). During each injection test, either the injection pressure or the injection flowrate is controlled by a pump set at the surface. The sampling frequency is 500 Hz. To facilitate analysis, the signal is down-sampled during pre-processing.

Packers were first inflated in order to seal the interval. Then, the displacement sensor was anchored to the borehole wall. Figure 3-6 shows the hydraulic cycles applied in the interval during each of the three performed tests. The protocol was practically the same for each interval:

- A pressure step-increase and step-decrease was first applied. Maximum pressure remained below the fracking or the stimulation pressure. This can be seen when the pressure at each step was constant. This cycle was used to (i) check the packers' sealing efficiency, and (ii) to test the SIMFIP clamping efficiency to the borehole wall. A linear relationship between the SIMFIP displacement and the pressure was used to apply the compensation related to the SIMFIP-borehole system mechanical response.
- The high-pressure stimulation cycles are then performed. The key idea is to produce a significant fracture displacement that will be later used to estimate the fracture mechanical properties and the state of stress. In the intact rock interval, this period corresponds to a succession of leak-off tests. In the two other intervals, pressure is initially increased step-by-step until fracture opening begins. Then, pressure is maintained for several minutes to grow the fracture away from the borehole influence. The interval is then shut-in for several minutes and finally bled off.
- The controlled pressure cycle is the last hydraulic cycle. Once the interval is fractured, or once a preexisting fracture is reactivated, this cycle's objective is to characterize the fracture's hydraulic properties. Pressure is maintained constant at different step values by varying the injection flowrate.

Pressures up to about 16 MPa and 2 to 4 l/min injection flowrates were applied during the tests performed in the COSC-1 borehole.

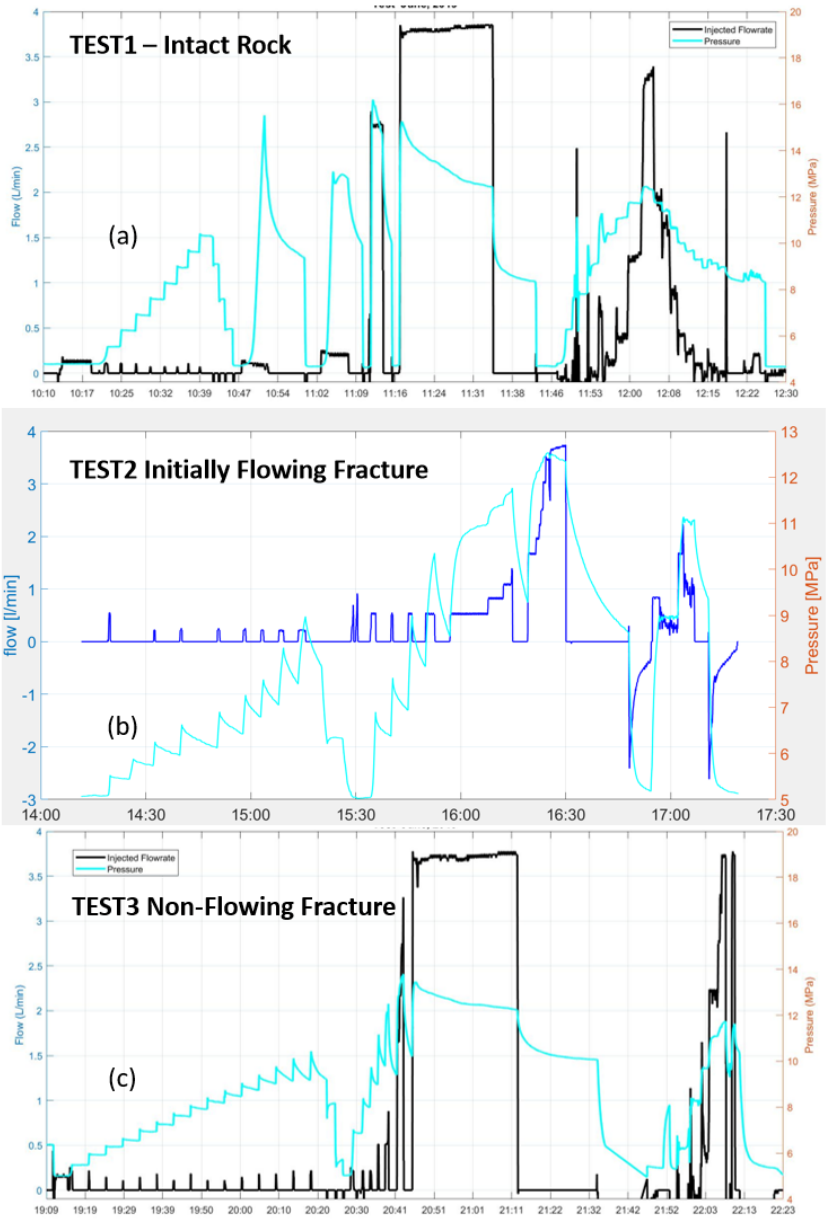

Figure 3-6. Hydraulic stimulation protocols applied in (a) – Intact rock interval (detailed analysis of the SRT test from 11:46 until 12:30 is shown in Figure 3-7), (b) – Initially flowing fractures interval (the higher pressure cycle conducted between 16:18 and 16:45 is detailed in Figure 3-8) and (c) – Non-flowing fractures interval (the fracture propagation period at 3.7 l/min injection flowrate from 20:42 to 21:11 is detailed in Figure 3-9).

3.3.2 Test Results

3.3.2.1 Synthesis of the activation pressures

Figure 3-6 and Table 3-1 summarize the key parameters deduced from the analysis of the SIMFIP tests. The breakdown pressures, which are the maximum pressures reached during the tests, vary from 12.5 to 16.15 MPa in the initially flowing fracture and intact rock interval, respectively. This pressure is considered as a rough estimation of the fracture initiation, which is known to start at lower pressure (Detournay et al.,

1997). The closed fracture interval displays an intermediate value of 13.79 MPa. The fracture propagation pressure, which is the pressure at which fluid-induced rupture propagates in the fracture, is consistent between all tests with values of 12.26 to 12.53 MPa. This pressure is picked at the end of the injection period, just before shut-in (Figure 3-6). The fracture opening pressure (FOP) and the fracture closing pressure (FCP) correspond to pressures when there is a sudden increase or decrease in the injection flowrate, caused by a hydraulic opening or closing of the activated fracture, respectively. The FOP/FCP increase with the depth of the tests with values of 9.25 MPa at Test 1 (485.2 m depth), about 11 MPa at Test 2 (506 m depth) and 11.7 MPa at Test 3 (515 m depth). This would correspond to a vertical stress gradient steeper than lithostatic, and this apparent depth-dependent variation may be locally perturbated around the activated fractures. Overall, these key pressures values do not differ much between tests although stronger contrast could have been expected due to the three contrasting interval geologies. Indeed, the fracture propagation pressures (FPP) are very close regardless of whether the interval contains initially flowing fractures, no flowing ones or intact rock. The FPP value is also close to what would be the expected vertical stress at the depth of the tests given a 2700 to 2800 kg/m^3 rock density (Hedin et al., 2016). Thus, the contribution of any rock or fracture strength to the FPP appears limited.

Table 3-1. Activated fractures, displacement modes and key activation pressures deduced from the three SIMFIP tests in COSC-1 borehole. See displacement vectors in Figures 3-7 to 3-9.

Test	Activated Fracture Depth/dd/d (m/degree/degree)	Mode	Displacement vector	Pressure Breakdown or max. (MPa)	Propagation Pressure (MPa)	FOP/FCP (MPa)
1 – Intact rock	484.9/246.6/12.9	Opening with shear increasing with fracture growth	AB	16.15	12.44	9.25 9.278
2 – Initial flowing fracture	505.9/288/12	Opening then shear at high Pressure	AB BC CD	12.53	12.53	10.98/11.55
3 – Closed Fracture	514.6/270/10 515.1/110/59	Mixed 2 fractures could be activated	AB CD DE EF	13.79	12.26	11.7/11.51

3.3.2.2 Test 1 – "Intact Rock"

Figure 3-6a shows that fracturing of the intact rock interval was conducted in 4 successive leak-off tests from 10:47 to 11:46 on June 18, 2019. It was followed by a pressure step-rate test from 11:46 until 12:30. All tests roughly show the same type of borehole displacement-vs-pressure responses. We focus on the final step rate test (SRT) test because, at this time, the rupture has propagated away from the borehole influence, and is more reflective of the *in-situ* fracture hydromechanical response. Figures 3-7a and b show a drastic change in the borehole displacements above 10MPa. It is the [AB] period from 12:03 to 12:10. It is about 1MPa above the FOP (Figure 3-7e), and it corresponds to a sharp non-linear increase in the injection flowrate. A large displacement offset remains when pressure is stepped down back to the initial borehole pressure, highlighting that some irreversible fracture displacement was triggered. Figures 3-7c and d show that this activation period is characterized by an upwards plunging $\underset{AB}{\rightarrow}$ vector oriented N0°. In detail, similar displacement orientations of smaller magnitudes are detected immediately following FOP. If we consider

the $\underset{AB}{\rightarrow}$ vector as representative of the opening of a mode 1 fracture, it should be parallel to the normal to the fracture plane. This gives a ~0/50° average orientation of the fracture. $\underset{AB}{\rightarrow}$ vector is also compatible with the opening with a reverse shear component of the 246/13 fracture observed on cores between the SIMFIP anchors.

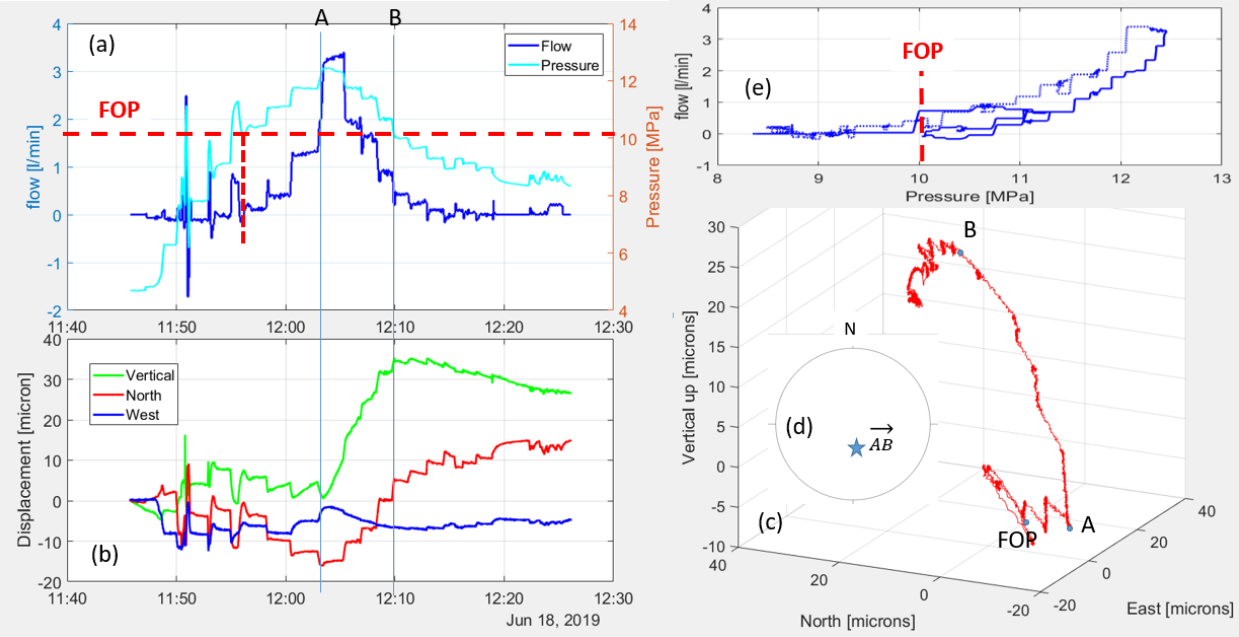

Figure 3-7. Test 1 pressure-displacement signals during the pressure-step-rate stimulation (see Figure 3-6a for location of this cycle in the entire test sequence). (a) – Pressure (light blue) and flowrate (dark blue). (b) – Displacements oriented in geographic coordinates. (c) – Three-dimensional displacement variation with time during the test. (d) – Stereographic lower hemisphere projection of $\underset{AB}{\rightarrow}$ displacement vector. (e) – Flowrate-vs-pressure curve (FOP is the Fracture Opening Pressure).

3.3.2.3 Test 2 – Initially Flowing Fracture

The initially flowing fractures were identified using a distributed water electrical conductivity probe test deployed at the interval depth before setting the SIMFIP test (see Section 3.2). As mentioned earlier, three flowing fractures were identified, two being between the SIMFIP anchors and one below. Displacements measured during activation of these fractures showed a contraction of the SIMFIP sensor, only compatible with the mechanical opening of the fracture located below the lower anchor. This test confirmed the initial hydraulic opening of the interval fractures since transient pressure steps were observed starting at the low pressures during the first pressure step rate cycle from 14:00 to 15:30 (Figure 3-6b). In Figure 3-8 we show details of the higher-pressure cycle conducted between 16:18 and 16:45 (Figure 3-6b), that produced the most significant borehole displacements. A large negative vertical displacement was observed while pressure was increased (Figure 3-8a and b). Compared to the horizontal northern and western displacements, which are relatively low, this shows that vertical movement is dominant and compatible with the opening of the gently dipping 288/12 fracture located below the SIMFIP anchors. The displacement evolution is described by several vector directions rotating with time, and with the interval pressure (Figures 3-8c and d). During the fast pressure increase, vectors $\underset{OA}{\rightarrow}$ and $\underset{AB}{\rightarrow}$ show a sub-vertical displacement. The fracture is mainly opening. When injection pressure gets to 12.3 to 12.5 MPa, there is a drastic reorientation

of the displacement vector characterized by a northern reverse movement on the fracture plane ($\underrightarrow{BC}$). After initial opening, the activated fracture is thus slipping at high pressure. When injection is shut-in, the fracture displays a mainly normal closing characterized by vector $\underrightarrow{CD}$, which is collinear to $\underrightarrow{OA}$ and $\underrightarrow{AB}$. Figure 3-8e shows no clear flowrate variation related to the fracture shearing period [BC], the sharp non-linear flowrate increase being associated to the [OB] normal opening period. Thus, Test 2 highlights two contrasting hydromechanical fracture responses: an initial normal opening at low to intermediate injection pressures followed by shear at high pressures.

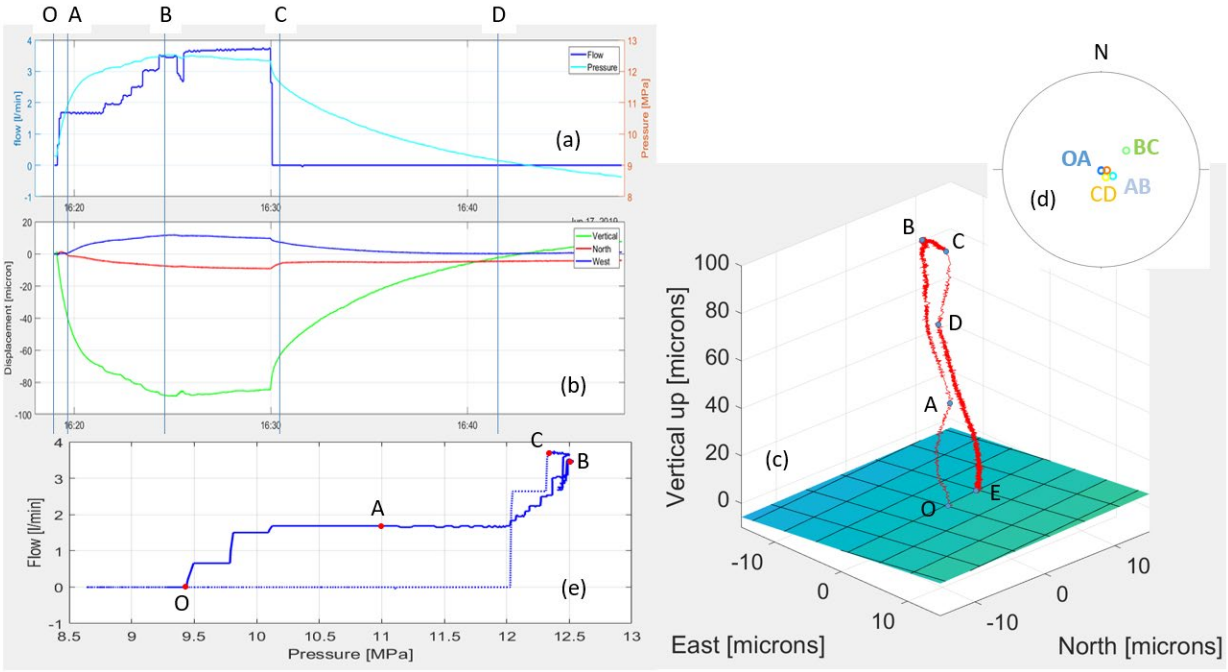

Figure 3-8. Test 2 pressure-displacement signals during the high-pressure stimulation cycle (see Figure 3-6b for location of this cycle in the entire test sequence): (a) Pressure (light blue) and flowrate (dark blue). (b) Displacements oriented in geographic coordinates. (c) Three-dimensional displacement variation with time during the test (the colored surface figures the initially flowing fracture plane). (d) Stereographic lower hemisphere projection of displacement vectors. (e) Flowrate-vs-pressure curve.

3.3.2.4 Test 3 – Initially Closed Fracture

The initially closed fractures were stimulated by applying increments of increasing pressure steps from 20:25 to 20:42 on June 17, 2019, until a clear hydraulic opening was observed, characterized by a pressure transient decay at the steps (Figure 3-6c). Then, a constant 3.7 l/min injection flowrate was applied from 20:42 to 21:11 to propagate the rupture in the fracture. At 21:11, the interval was shut-in until 21:32, and finally bled off. Figure 3-9 shows the hydromechanical response of the interval during the fracture propagation period at 3.7 l/min injection flowrate from 20:42 to 21:11. During this period, the fracture propagates away from the borehole's stress influence. It is considered as the most relevant period for the analysis of the *in situ* fracture's response. Compared to the two other test intervals, the displacements display both a significant vertical and horizontal variation during the fracture propagation, highlighting shearing of the borehole (Figures 3-9a and b) although there is not much offset at the end of the test. Displacements evolve in a complex way, characterized by a general eastward and up-dip direction (Figures 3-9c and d), but with sharp reorientations in details. This highlights a much more complex interval

stimulation than was observed in the two other tests. It could relate to the activation of the two families of fractures affecting the interval, respectively the 170/10 and 110/59 fractures both being between the SIMFIP anchors. $\overrightarrow{AB}$. and $\overrightarrow{EF}$. vectors match well with the opening of the flat-lying 170/10 fracture. Reorientation to $\overrightarrow{CD}$.and $\overrightarrow{DE}$. best match with dilatant shear along the 110/59 fracture. Figure 3-9e shows that flowrate increase is associated with the vertical displacement vectors, thus the normal opening of the flat-lying fracture. There is no flowrate variation during shearing of the 110/59 fracture.

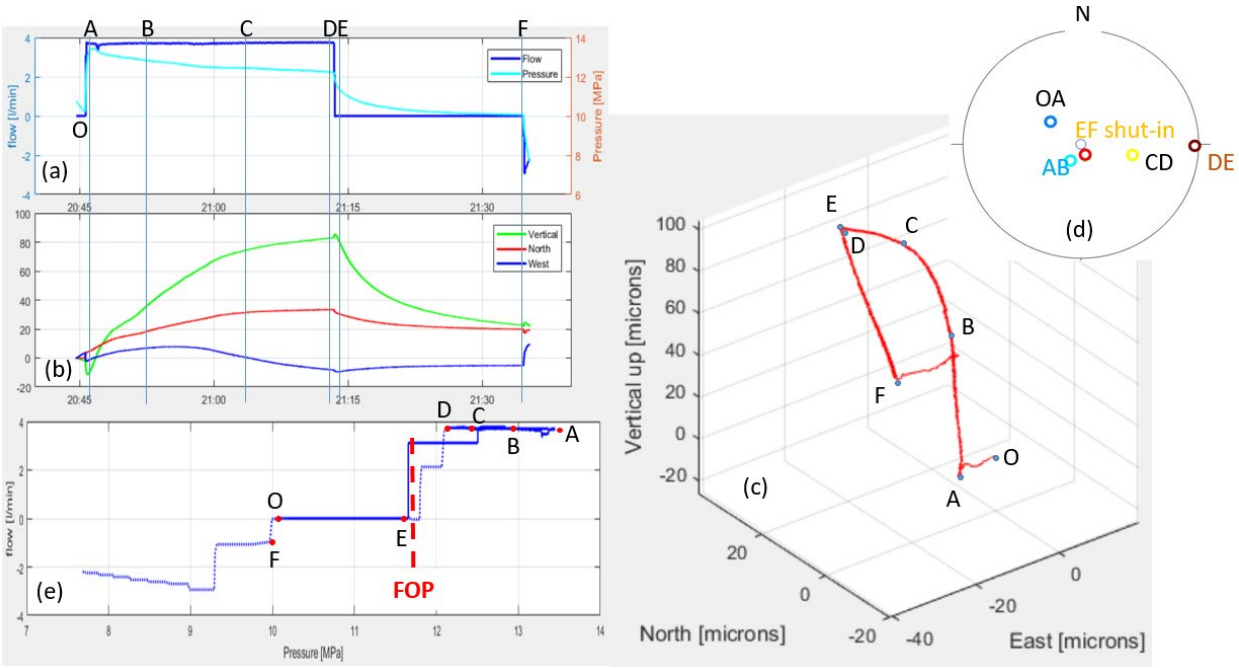

Figure 3-9. Test 3 pressure-displacement signals during the high-pressure fracture propagation cycle (see Figure 3-6c for location of this cycle in the entire test sequence). (a) Pressure (light blue) and flowrate (dark blue). (b) – Displacements oriented in geographic coordinates. (c) Three-dimensional displacement variation with time during the test. (d) Stereographic lower hemisphere projection of displacement vectors. (e) Flowrate-vs-pressure curve.

3.3.2.5 Synthesis of the activation displacements

In all tests, displacements are characterized by a dominant vertical orientation. Horizontal displacements are 1/4 to 1/10 the vertical ones in Test 3 and Tests 1&2, respectively. Displacement magnitudes are the same between tests, of about 10 to 100 micrometers. There is a very good correspondence between the main displacement variations and the hydraulic response to pressure stimulation. Figure 3-10 is a summary of the observed fracture activation modes. In Tests 1 and 2, it is mainly normal opening of the parallel-to-foliation fractures, with an irreversible slip component at the highest stimulation pressures. It is consistent with these intervals' geology consisting of foliation planes or flat-lying fractures. No clear new fracture may have been created by the stimulations (although this will require additional checking from post-testing image logging that should be conducted in June-July 2020 in the COSC-1 borehole). In Test 3, there is a more complex activation story possibly caused by the two fractures affecting the interval. The opening of the flat-lying fracture competes with the reverse shearing of the steeply dipping 110/59 fracture. These two fractures, which were observed to be closed on the corresponding core samples, opened in the field within the same range of stimulation pressures as in the two other intervals. One possibility could be that in Test

3 and in Test 1, flat-lying fractures are closed but not sealed and can open under pressure. In Test 3, the in-filling material of the 110/59 fracture may not add much strength to the fracture that reactivated.

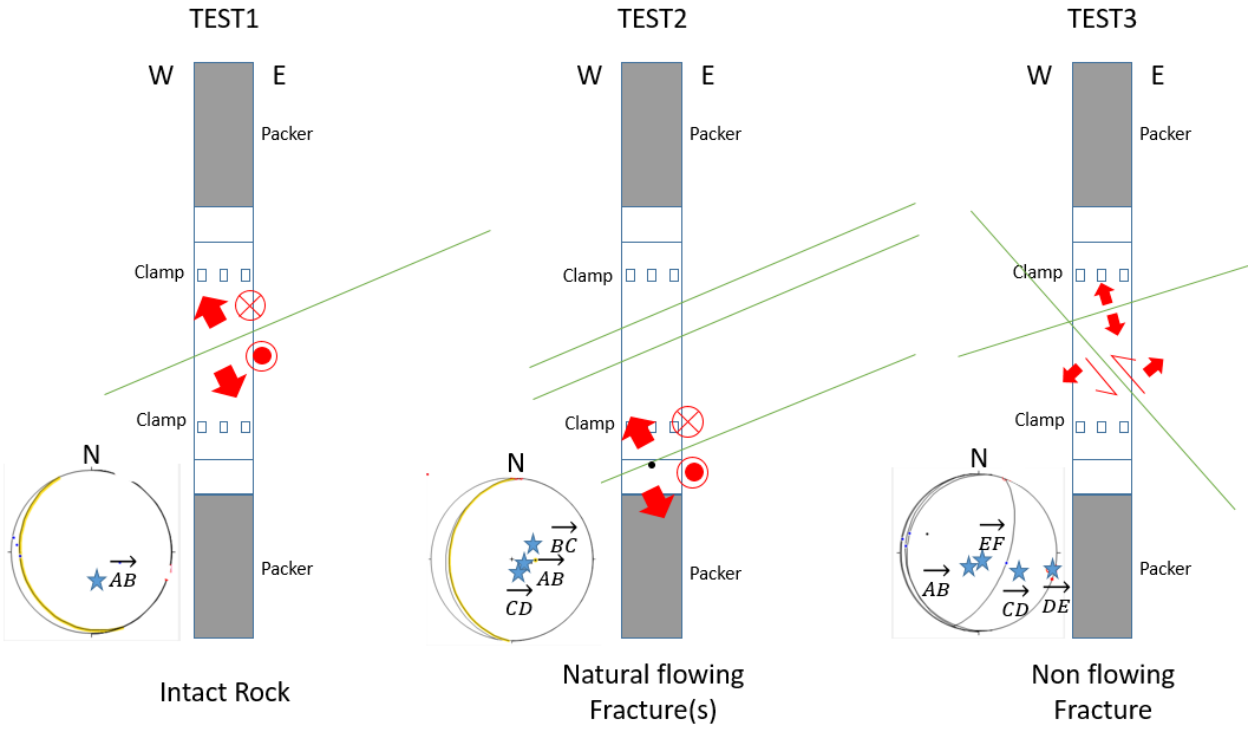

Figure 3-10. Fracture activation mechanisms deduced from in situ SIMFIP tests.

3.4 Stress Estimation from The Inversion of Displacement Data

The stress state is computed following the protocols on dislocation analysis during fluid injection and its application to stress inversion developed by Kakurina et al. (2019, and submitted). The protocol is based on inverting the SIMFIP borehole displacements vectors that have been identified in Section 3.3. We only consider the slip component of the displacement vector. The orientation of the vector together with the orientations of potentially reactivated fractures in the interval is the starting point for estimating the stress state from a single injection test. First, all possible reduced stress tensor solutions that fit the measured slip are searched. Second, the normal and vertical stress are matched on the reactivated fracture into the reduced stress ellipsoid. For the COSC-1 tests, the vertical stress was estimated by the weight of the overburden considering a 2700 kg/m^3 density (within the range of values reported by Hedin et al., 2016). The stress tensor is calculated using the orientation of the activated fractures in the intervals, their normal stress and the slip on these fractures, triggered during the fluid injection (Tables 3-1 and 3-2). We assume that the normal stress is equal to the fracture closing pressure (FCP) measured during the fluid injection (Section 3.3). We also assume that due to the vicinity of all the tests the slip may have triggered under the same stress state (or under a close variation of the stress). Nevertheless, we also conducted stress estimation by considering each test individually, in order to compare with the stress estimation from the three tests taken together. The input data for the stress inversion are given in Table 3-2.

Table 3-2. Input data used for the stress inversion from the COSC-1 SIMFIP tests

Test	Fault		Slip		Sense (1 - reverse)	FCP
	Dip dir.	Dip angle	Dip dir.	Dip angle		
1 (intact)	247	13	348	-3	1	9.28
2 (open)	288	12	53	-7	1	11.55
3 (closed)	110	59	282	-59	1	11.51

Firstly, we search for the reduced stress tensors, i.e., stress orientations (S1, S2 and S3) and stress ratio (R), for which the angular misfit between measured and calculated slip orientations is the smallest. When considering only one test at a time, there are several possible stress tensor solutions represented by the multiple colored dots in Figures 3-11a, c and e. The tensor's orientation is consistent between tests. It appears that all inversions display a sub-vertical σ_3 while σ_1 and σ_2 may shift to one another depending on the tests. When the three tests are considered all together, there is only one solution of the reduced stress tensor, which would have the angular misfit with all the measured slip of less than 10° (Figure 3-11g):

- σ_1=284.1/11.2 (red marker);
- σ_2=14.9/4.2 (blue marker);
- σ_3=125.0/78.0 (green marker),
- R=0.2.

The absolute principal stress magnitudes $\sigma_1, \sigma_2, \sigma_3$ are calculated by fitting the estimations of the fracture normal stresses σ_{n1} and σ_{n2} into the stress ellipsoid defined by the reduced stress state. We considered the normal stresses calculated on fractures 247/13 and 288/12, using equations below:

$$\begin{cases} R = (\sigma_2 - \sigma_3)/(\sigma_1 - \sigma_3), \\ \sigma_{n1} = l_1^2\sigma_1 + m_1^2\sigma_2 + n_1^2\sigma_3, \\ \sigma_{n2} = l_2^2\sigma_1 + m_2^2\sigma_2 + n_2^2\sigma_3, \end{cases}$$

where l_1, m_1, n_1 and l_2, m_2, n_2 are the direction cosines of the normal components of the fractures with respect to the principal stress axes.

When all tests are considered (Figure 3-11h), the magnitudes are $\sigma_1 = 11.82\ MPa,\ \sigma_2 = 9.77\ MPa, \sigma_3 = 9.26\ MPa$, respectively. Other combinations of the normal stresses of the fractures do not give a solution. When tests are taken separately, there is a strong variability of magnitudes between tests (Figures 3-11b, d and f), some values looking unrealistic given the COSC-1 borehole regional context.

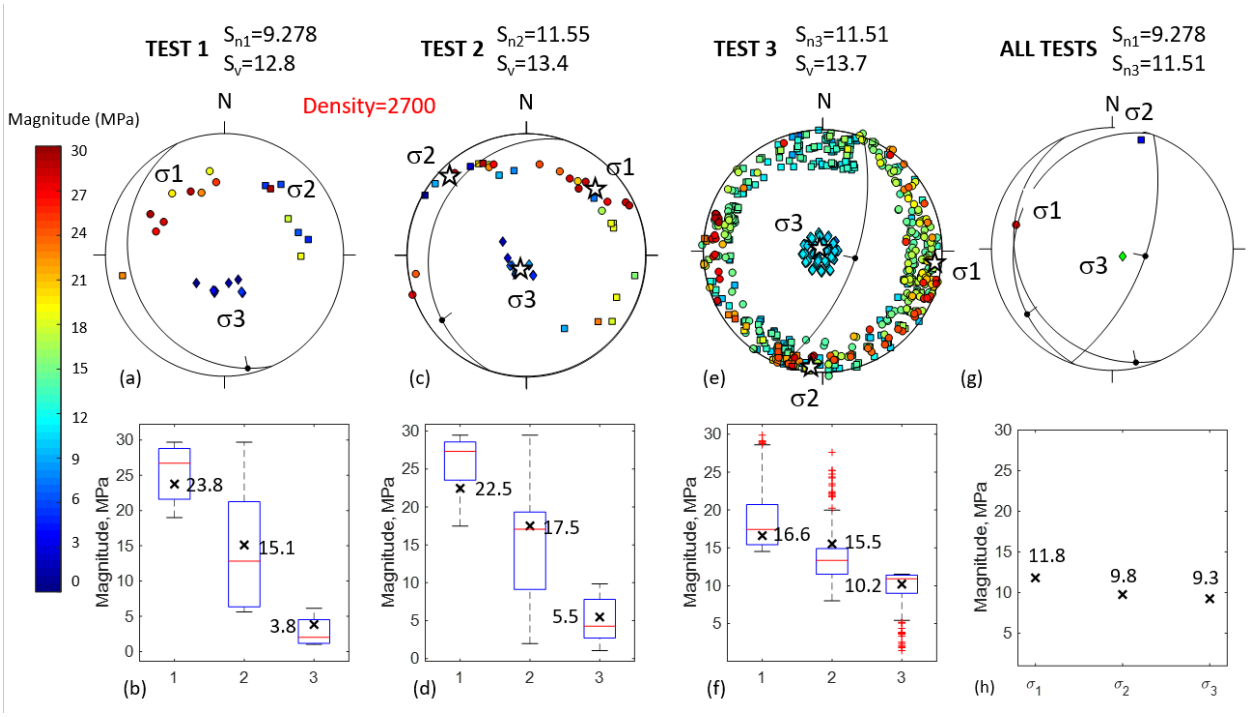

Figure 3-11. Stress inversion from SIMFIP displacement vectors and key interval pressures. Upper row shows the principal stresses orientation projected in a lower hemisphere stereogram (σ1 are circles, σ2 are squares, σ3 are diamonds, colors are stress magnitudes). Lower row shows the statistical variation of principal stress magnitude for each single inversion solution.

When the three tests are considered, we get a reverse stress regime in good accordance with the slightly reverse movements measured on all the activated fractures. Stress tensor horizontal stress orientation is in reasonable accordance with the one deduced from borehole breakout analyses (Wenning et al., 2017). The magnitude of the minimum principal stress appears lower than the weight of the overburden (which is about 13.8 MPa, considering a rock density of 2800 kg/m^3 at 500 m depth), which may look surprising. This approach assumes a homogeneous and constant pore pressure inside a non-deformable activated fracture, which results in an overestimation of the effective stress, and in an underestimation of the total normal stress applied on the fracture. Since here most of the fractures are sub-horizontal, it may explain the underestimated vertical stress.

Our approach gives an estimation of the potential full stress tensor (orientation and magnitude) taking advantage of the borehole displacements and pressures measured during the SIMFIP tests. The magnitudes of the principal stresses are close to each other, as it may be expected at the shallow depth of the tests. It is interesting to see that the estimated tensor is consistent with the one estimated from borehole breakouts (Wenning et al., 2017), observed at larger depths than the SIMFIP tests (below 600 m depth). It may show that although weaker, the stress regime is still reverse in the shallow crust. The tests showed a strong opening component of the stimulated fractures, which is not considered in our stress estimation, the slip component being a minor component of the observed fracture movements in comparison. In the next section, this stress tensor will be refined using a more exact numerical modeling of the tests.

3.5 Fully Coupled Numerical Analysis of the Simfip *In-Situ* Tests

3.5.1.1 Numerical model setting

We developed three-dimensional models of fractures in the three borehole intervals using the distinct element code 3DEC (Itasca Consulting Group, 2016). The code can be used to conduct fully coupled hydromechanical analysis of the fracture movement induced by the injections. Compared to the stress inversion approach (Section 3.4), the numerical modeling aims at studying the coupled hydromechanical processes of fluid diffusion in the activated fractures. We are interested in exploring how adding downhole displacement monitoring during a hydraulic stress test can help improve the fracture hydraulic conductivity dependency on its activation mode. We use a fully coupled hydromechanical approach to better assess the effects of the pore pressure profile evolution from the injection point into the stimulated fracture. The model domain has side-lengths of 20 m and contains the fractures activated in each interval (Figure 3-12).

We assume that the complex opening of the fractures observed in the field corresponds to a fault rupture is described by a generalized Coulomb failure criterion, including the possibility for failure in shear and in tension. The elastic hydromechanical response of the fracture is also included in the numerical model.

Injection of fluid leads to a change of pressure and fluid flow in the stimulated fracture, and consequently, to a change in stress over the fault surface and a change in aperture follow. It is assumed that the cubic law (Witherspoon et al., 1980) can be used to describe fluid flow in the fault:

$$Q = -\frac{b_h^3 \cdot w}{12\mu}\Delta P \tag{6}$$

where Q is the flow rate (m^3/s), ΔP is the increment in fluid pressure (Pa), μ_f is the viscosity of fluid (Pa.s), w is the fault width (m), and b_h is the hydraulic aperture (m), which is defined:

$$b_h = b_{ho} + \frac{\Delta\sigma_n'}{k_n} + \Delta u_s \cdot \tan\psi \tag{7}$$

where b_{ho} (m) is the initial aperture at zero normal stress, $\Delta\sigma_n'$ is the increment in effective normal stress, Δu_s (m) is the shear slip increment, and ψ is the dilation angle (°). Dilation occurs only as the fracture slips. The hydraulic aperture is linked to the permeability as follows:

$$k = \frac{b_h^2}{12} \tag{8}$$

Experimental and numerical analyses have showed that the cubic law is adequate to simulate fluid flow and hydromechanical effects along smooth surfaces (Brown, 1989; Zhang et al., 2019).

The numerical solution for fluid flow is based on the fluid domain network structure (Itasca Consulting Group, Inc., 2016). Each domain has a uniform fluid pressure and can communicate with the neighboring domains. Thus, the fluid flow is governed by the difference in pressure between adjacent domains. At each time step (Δt in s), the fluid pressure (P in Pa) is updated considering the net fluid flow and the domain volume change (ΔV):

$$P = P_0 + K_w Q \frac{\Delta t}{V} - K_w \frac{\Delta V}{V_m} \tag{9}$$

where P_0 is the initial fluid pressure, K_w (P_a) is the fluid bulk modulus, and $V_m = (V^t + V^{t-1})/2$ with V^{t-1} and V^t, the domain volumes (m^3) at previous (τ-1) and new (τ) times, respectively.

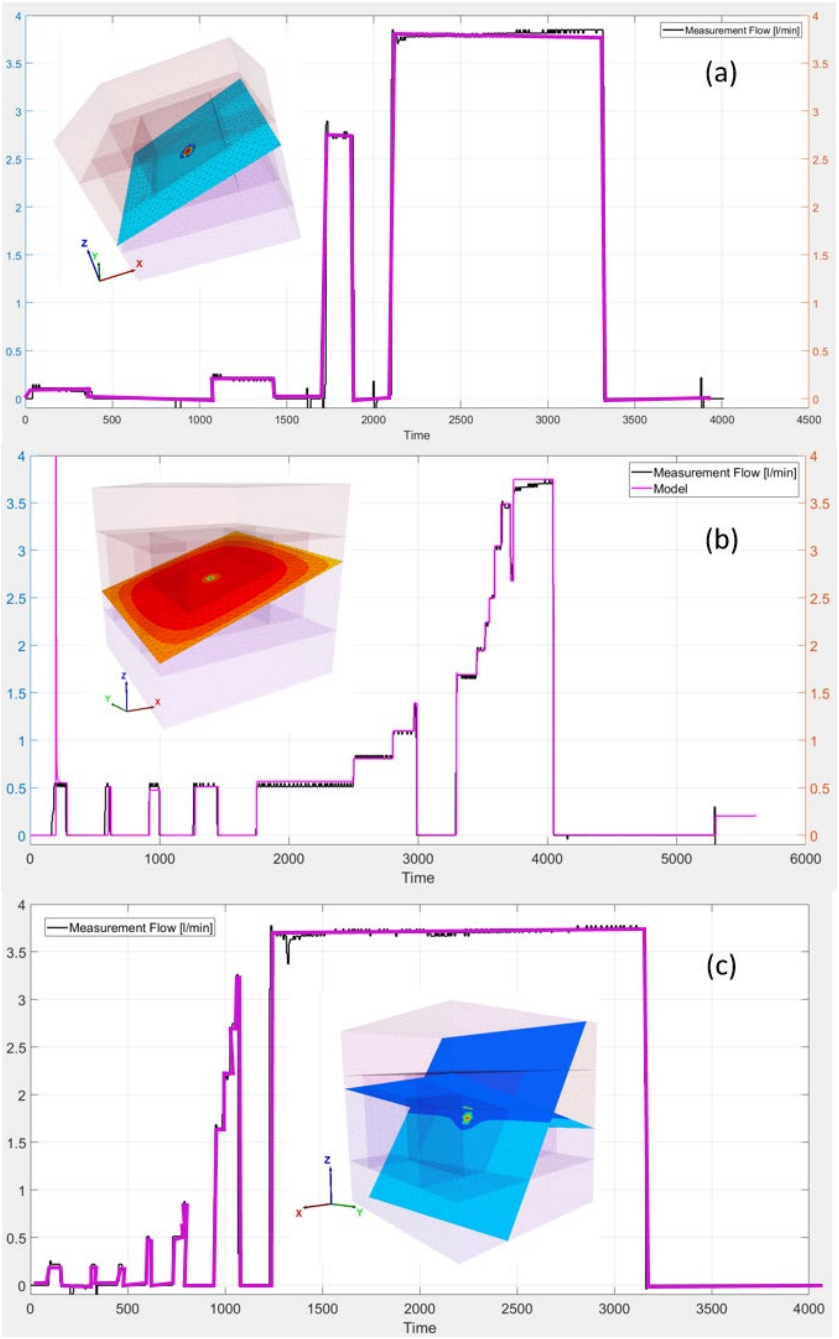

Figure 3-12. Numerical model geometry and injection flowrate history applied to the models of (a) Test 1, (b)– Test 2, and (c) Test 3. Blocks show the model with side lengths of 20 m. Colored planes are the geological fractures observed in each test interval. Injection point is the colored feature in the center of each model. Graphs show the flowrate injected in the field (black curve) and the flow rate history injected in the model (purple curve).

We used two different fluid flow modes to reproduce the observed fluid pressures:

(1) A variable permeability model (i.e. the cubic law and a value of hydraulic aperture that changes with the evolution of fault normal displacement). This flow mode was used to model the initially flowing fracture in Test 2;

(2) A variable permeability model activated at failure. We use the "crack flow model" implemented in 3DEC to simulate fluid flow in the activated parts in shear or tensile failure of the fracture plane, and prevent flow from occurring in the remaining elastic parts. This assumption is used to model the hydromechanical responses of the two initially closed intervals, during Tests 1 and 3 respectively.

The fault/fracture/rock properties used in the model are given in Table 3-3. The host rock is assumed to be linear elastic. The host rock matrix is considered impermeable. Fracture stiffness (K_n, K_s) are estimated from matching the initial reversible parts of the measured displacement-vs-pressure in situ curves. An initial hydraulic aperture is given to initiate the model. It is incrementally actuated during calculation iterations. Fracture friction, cohesion and tensile strength are given values found in the literature for this type of rock. These values are adjusted until a best match is observed between calculated and measured displacements. We start by applying the stress field estimated in Section 3.4 to all the models' boundaries. Stress magnitudes are then adjusted to match the magnitude and orientation of the measured displacements following the method developed in Guglielmi et al. (2020). A sensitivity study to the different model parameters is conducted but it is not described in this report. Here we focus on the comparison between the three tests. The field injection is simulated by applying the injection flowrate at the model's fault grid point coordinates (0, 0, 0) (purple curve in Figure 3-12) that theoretically represents the measured time-history of injection flowrate imposed in each interval during the in-situ tests. Normal and shear displacements of fractures and pore pressure are calculated at the injection point and compared to field measurements (Figures 3-13 to 15). First, the model is run to equilibrium to establish the initial static stress and pressure conditions. Then, the injection flowrate is applied (Figure 3-12).

Table 3-3. 3DEC model parameters for Test 1–Intact rock, Test 2–Initially flowing fracture, and Test 3–initially closed fracture. Bulk and shear modulus were averaged from K3 perpendicular-to-foliation value in Wenning et al. (2017) and a Young's modulus used in Stephansson et al. (1991). Fracture properties were adjusted by trial and error in order to match calculated and measured SIMFIP displacements.

Parameters	Units	Test 1	Test 2	Test 3
Bulk modulus of rock *(K)*	GPa	33.3	33.3	33.3
Shear modulus of rock *(G)*	GPa	25	25	25
Rock density *(ρ_r)*	kg/m^3	2800	2800	2800
Fault elastic stiffness *(k_n, k_s)*	GPa/m	20, 1	3.3, 0.17	8.0, 0.3
Friction angle	(°)	25	25	25
Cohesion/Tensile strength	(MPa)	(0,0)	(0,0)	(0.2,0.2)
Initial hydraulic aperture *(a_{ho})*	μm	10	10	10
Dilation angle *(ψ)*	Degree	5	5	5
Initial fluid pressure *(P_o)*	MPa	6.2	6.2	6.2
Fluid Bulk modulus (K_w)	GPa	2	2	2
Fluid density (ρ_f)	kg/m^3	1000	1000	1000
Fluid viscosity (μ_f)	Pa.s	0.001	0.001	0.001
Stress (σ1,σ2,σ3)	(MPa)	(14.5,14.0,13.0)	(14.5,14.0,13.0)	(14.5,14.0,13.0)

3.5.1.2 Model results

Figure 3-13 shows the best fit of calculated pressure, fracture opening and shear to the experimental data measured during Test 1. To achieve a reasonable match, we considered a 246/13 fracture initially closed but with no cohesion and no tensile strength (Table 3-3). The initial pressure cycles 1 and 2 (until 1600 seconds) are underestimating the field breakdown pressures while a reasonable match is obtained during the two following cycles. This is explained by the adopted modeling protocol that assumes the presence of a preexisting fracture, thus neglecting any new fracture creation or propagation (this physics is not included in the current model). The two initial cycles might involve some fracturing of the interval to explain the much higher field breakdown pressures compared to the model. Cycles 3 and 4 are much better explained because the rupture has grown into a macroscopic fracture such as the one represented in our model. Nevertheless, shear displacements are poorly explained by the model. The model calculates an increasing slip with fracture growth. This is not clear in the field data where there is little slip in the field and dominant fracture opening. Indeed, the fracture's normal displacement is well reproduced by the model. The best fit is obtained at the last pressure cycle. We calculate a slightly reverse stress regime characterized by a stress tensor oriented as the one deduced from the inversion in Section 3.4. We get principal stress magnitudes (σ_1, σ_2, σ_3) = (14.5, 14.0, 13.0) MPa at the injection point, 2.7 to 4.2 MPa larger than the estimates of Section 3.4, and little difference between the values of the principal stresses. Such a difference can be related (i) to the inversion approach, which underestimates stresses (see Section 3.4) or (ii) to stress concentration effects that govern the fracture growth (and that are poorly captured by the numerical approach).

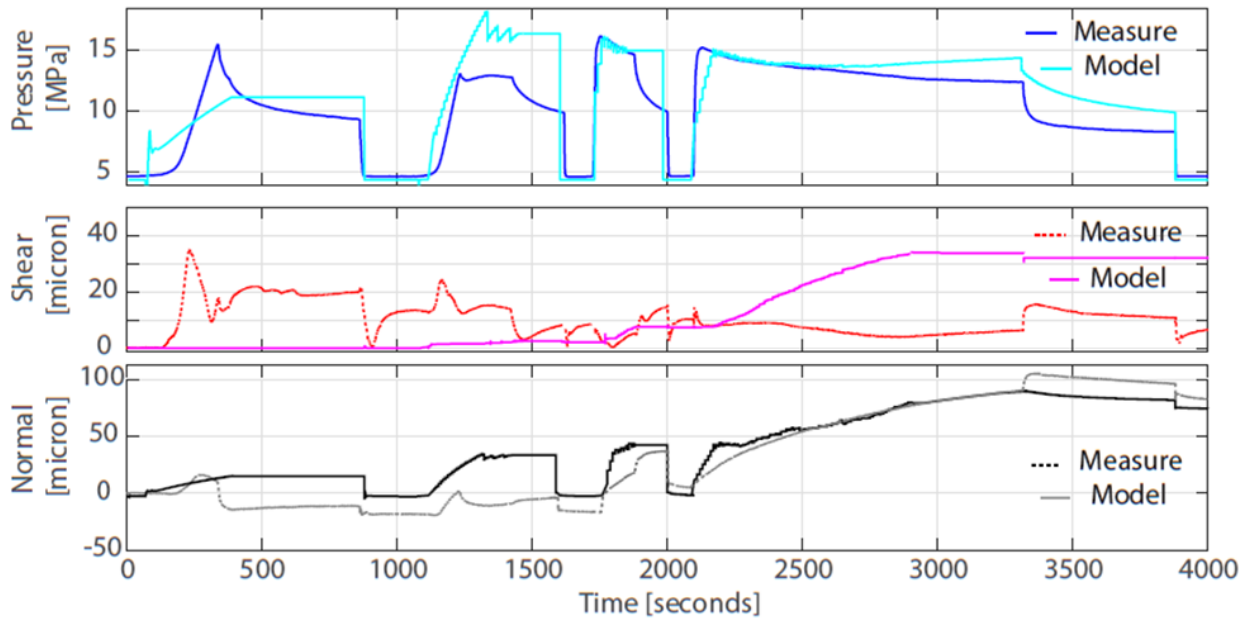

Figure 3-13. Comparison of pressure, normal opening and shear calculated with 3DEC (see model geometry in Figure 3.12a) with field measurements during Test 1 in intact rock.

Figure 3-14 shows the best fit of calculated pressure, fracture opening and shear to the experimental data measured during Test 2. There is a reasonable match of the model calculation to field data. The main difference lies in the model that does not accurately reproduce the transient pressure decays when injection is stopped (either during the initial cycles or during the shut-in at the end of the last cycle). Calculated pressure is always decaying much faster than the field pressure. This is explained by the relatively small size of the numerical model (20 m x 20 m x 20 m), and the very simple applied boundary conditions. The model better describes the injection source near-field hydromechanical response of the fracture than the far-field response, which is contained in the shut-in temporal evolution. The calculated shear displacements are small and in the range of the measured ones. Normal opening of the fracture is the dominant mechanism affecting fracture flow and the calculated pore pressure. We get the same state of stress as the one used in Test 1. The fracture shear and normal stiffness is estimated 6 times smaller in Test 2 than in Test 1. Thus, the flowing fracture appears much more deformable than the closed (or newly created) fracture in Test 1.

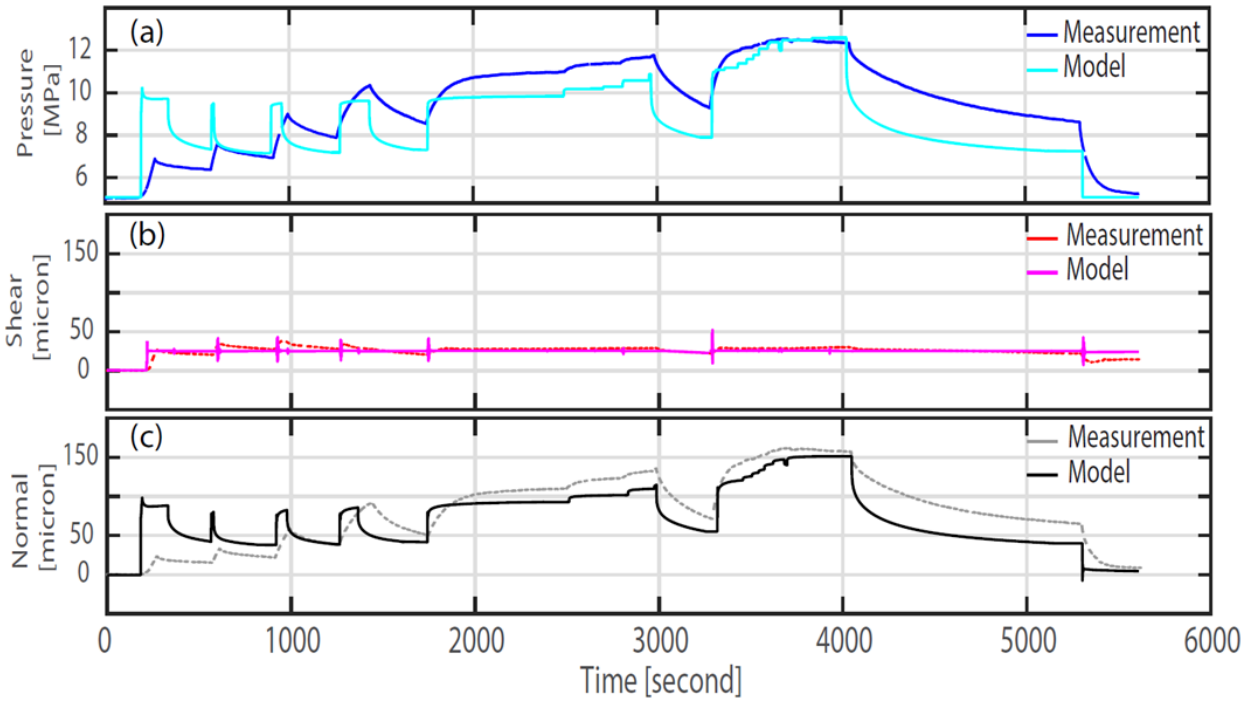

Figure 3-14. Comparison of pressure, normal opening and shear calculated with 3DEC (see model geometry in Figure 3.12b) with field measurements during Test 2 of the initially flowing fracture.

Figure 3-15 shows the best fit of calculated pressure, fracture opening and shear to the experimental data measured during Test 3. Here the model was stopped at about 1400 seconds because rupture reached the model's boundaries. This model is more complex than Tests 1 and 2 ones because it involves two cross-cutting fractures. We simultaneously inject half the measured flowrate in the center point of each fracture. Both fractures are affected by the same properties, and compared to Tests 1 and 2, we had to set a cohesion and a tensile strength equal to 0.2 MPa to match the displacement magnitudes. The same state of stress as in Tests 1 and 2 is calculated. The initial pressure and displacement steps are under-estimated until 500 seconds. After 500 seconds, the model reproduces reasonably well both pressure and displacement. We compare the calculated SIMFIP displacements (Figure 3-15c) to the field measurements (Figure 3-15b), because we do not a priori know which of the two fractures' movement explains the measured borehole displacements. A snapshot of the model's pore pressure shows that at 1000 seconds, most of the flow (red patch) is going into the 110/59 fracture. We thus conclude that this fracture predominantly activated and explained the observed displacements.

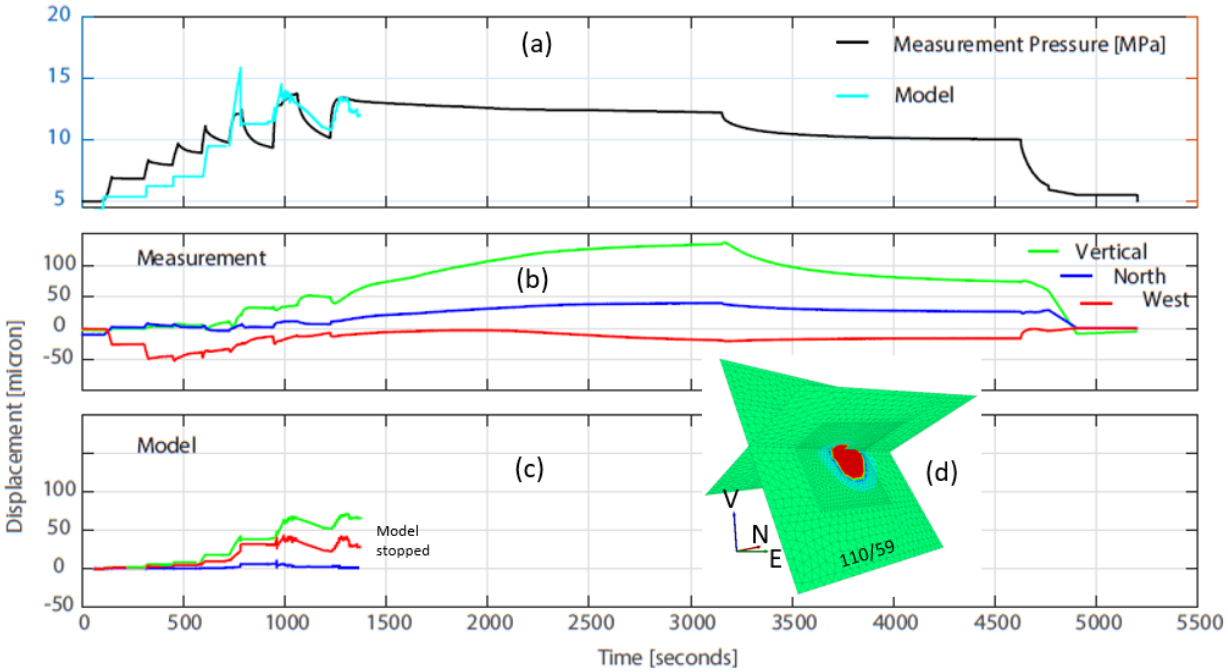

Figure 3-15. Test 3 closed fractures. (a) – Interval pressure. (b) – Measured SIMFIP displacements in geographic coordinates. (c) – Calculated SIMFIP displacements. (d) – Snapshot of fractures' pore pressure calculated at 1000 seconds (in this model flow is only allowed in the red patch which is growing with mechanical shear or tensile rupture of the predefined fracture surface).

3.5.1.3 Conclusions

The fully coupled numerical modeling of the three tested intervals allows for refining the estimate of the stress tensor, which is characterized by a slightly reverse stress regime, and an orientation consistent with the one deduced from the inversion of the SIMFIP displacement vectors. The same principal stress magnitudes (σ_1, σ_2, σ_3) = (14.5, 14.0, 13.0) MPa are used to reproduce all the tests.

The difference between the tests is explained by factor-of-6 difference in fracture stiffness and in strength and cohesion. The open-flowing fracture is also the less stiff fracture. The fracture activated in Test 1 has the highest stiffness. It can be an initially closed preexisting natural fracture sub-parallel to the foliation. Some observations on cores show that such a feature might exist, but the borehole logs do not show any preexisting fracture. It might also be a newly created fracture subparallel to the foliation, which could have provided weak planes for fracture nucleation. Test 3 shows that the 110/59 fracture with mineral infilling may reactivate under pressure even if affected with a moderate cohesion and tensile strength.

3.6 Conclusions of the Field Fracture SIMFIP Tests

Analyses of direct field pressure and displacements with an inversion method and with three-dimensional fully coupled forward numerical modeling allows for defining the activation sequence of fractures affecting the shallow crystalline crust at ~500m depth in the COSC-1 borehole. Flat-lying fractures subparallel to foliation open under variations of the normal effective stress in a slightly reversed stress regime. Planes reactivate at fracture opening pressures (FOP) as low as 9.3 MPa, about 3.7 MPa below the sub-vertical minimum principal stress. Our observations show that normal opening of fractures explains most of the flow leakage while shearing does not correlate with any change in the leakage flowrate. Borehole water electrical conductivity measurements highlight the natural leakage of some fractures before testing, while fracture displacements testing with a SIMFIP probe shows that fractures display 10-to-100 micrometer opening under a fluid pressure increase. The naturally flowing fractures appear more deformable than the closed ones for the same injection pressures. Sealed (mineralized) non-flowing fractures apparently do not display additional strength to behave differently from the closed fractures. They activate as easily as the other fractures given their orientation towards stress. The geology of the three different intervals give roughly the same leakage pressure and flow response under a comparable state of stress.

Next steps will be to analyze in detail the shut-in periods to get complementary information on the far-field connection of the fractures tested in intervals with other fractures existing in the surrounding host rock. In parallel, considering fracture mechanics in the numerical analyses will give an estimation of the stimulated fracture sizes. Numerical models tuned at the three intervals applied to other zones of the borehole will allow extending this approach to a statistical estimation of potential leakage of fractures under the state of stress defined in this study. All these steps combined should lead to a discrete fracture network including realistic individual fracture properties, and the variations of these properties with stress.

3.7 Laboratory Measurements of Transmissivity of Fractured Rock Cores

3.7.1 Introduction

This section summarizes laboratory work on anisotropic flow through fractures, which was conducted at LBNL in FY19-20. Previous work on anisotropic flow through natural fractures was completed for this project, but corresponding field transmissivity information was not available. Starting from FY18, measurements on artificial fractures were conducted to verify performance of the measurement system. During FY19-20, as a result of field work activities, three new core samples corresponding to the three zones examined by the SIMFIP were obtained and laboratory measurements were completed on one of these samples.

3.7.2 Experimental Design

Details of the experimental apparatus were described in previous reports (e.g., Dobson et al., 2017; Zheng et al., 2018). Transmissivity was measured over a range of effective stresses from 200 to 4000 psi in a custom constructed apparatus allowing water delivery to any of four inlets distributed at 45-degree increments around the circumference of the core, and to extract water from an outlet opposite to the inlet (Figure 3-16). The inlets and outlets are stainless steel half-tubes that run along the length of the core insuring contact with the fracture. A custom silicone rubber sleeve was manufactured to fit both around the core and inlet and outlet half-tubes to inhibit flow around the core. This sleeve was cast with silicone molding compound over a mockup of the setup to provide the proper fit. The pressure vessel was filled with water and confining pressure controlled by a high-pressure syringe pump. Flow through the fracture was driven using a second precision high-pressure syringe pump (Isco D-series). Confining pressure ranged

from 200-4000 psi, depending on the core, and pressure in the sample was below 20 psi at all times. Differential pressure measurements along the 60 mm flow path of the fracture was typically on the order of 0.1 – 1 psi, which necessitate adjustments of flow rate to maintain that range, depending on the transmissivity of the fracture.

To measure transmissivity, confining pressure is applied and a flow is applied to achieve a differential pressure across the fracture. Each channel was measured with a minimum of three flow rates, the resulting transmissivity was calculated, and the results from the three flow rates was averaged. In some cases, transmissivity was measured in both the forward and reverse direction.

Transmissivity was calculated using the following relationship:

$$Transmissivity\ (m^2/s) = \frac{Qg\rho l}{\Delta P w}$$

where Q is the volumetric flow rate (m^3/s), g is gravity, ρ is density, l is the fracture length, w is the fracture width, and P is pressure.

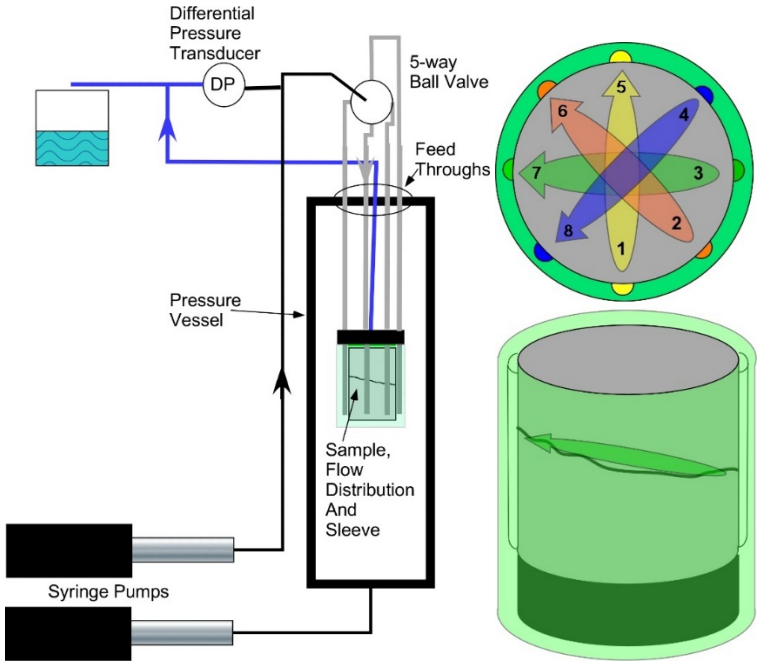

Figure 3-16. System schematic showing that the lower syringe pump controls confining pressure, and the upper syringe pump is used to inject water into the core. Two 5-way ball valves (one shown) control flow to the inlet tubes (1-4) and outlet tubes (5-8).

3.7.3 Core Descriptions

Three different artificial fracture (AF) Delrin cores were manufactured to be the same geometry as the rock cores (Figure 3-17). The AF1 core was solid except for one 1/16 in diameter horizontal hole through the center, and was designed to test whether circumferential flow could occur in the system. The second artificial fracture core (AF2) was the same size, but cut in half, with one side of the 'fracture' machined to have 4 rectangular channels, with cross sections of four channels of 0.26 mm^2, 0.50 mm^2, 1 mm^2, and 1.52

mm^2 to compare the results of measurements of transmissivity against predicted transmissivity based on this simple geometry. The third artificial fracture core (AF3) was also two-piece Delrin core with one side of the fracture etched with random paths placed in the system and tested with the same range of confining pressures used for the natural cores.

Natural fractures in core samples from the COSC-1 borehole were used in the apparatus to evaluate anisotropy with flow direction. Three cores were identified as usable in the apparatus due to geometry and condition of the fracture. Core 211-2 and 401-1 were measured previously, and Core 143-4 was received this FY (Figure 3-18). All cores were extracted from same borehole, but due to some alignment uncertainties the exact location of the extracted fracture in the borehole was uncertain. During field work in 2019 a new flowing fracture was studied, and core 143-4 was identified for comparison to field-measured transmissivity. Note that the X-ray CT scans shown in Figure 3-18 are taken without confining pressure, so apertures appear larger than they would during the measurement cycles.

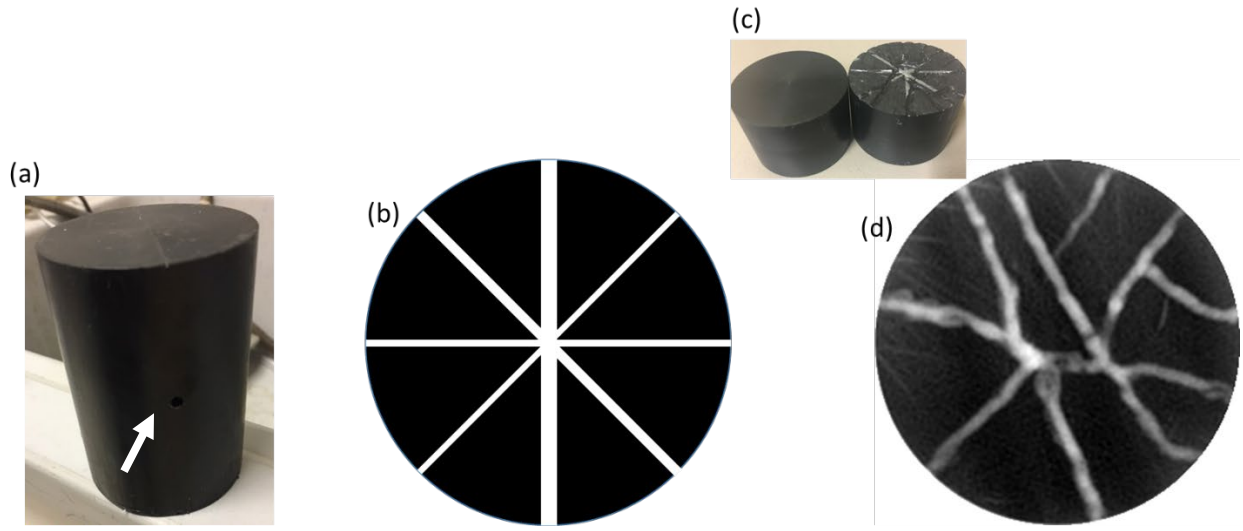

Figure 3-17. Artificial cores: (a) AF1, Delrin core with 1/16 in hole drilled through center. Hole is difficult to see but location indicated by arrow, (b) schematic of AF2 with lines representing rectangular channels, (c) image of AF3 Delrin core, and (d) AF3 cross section showing flow pathways.

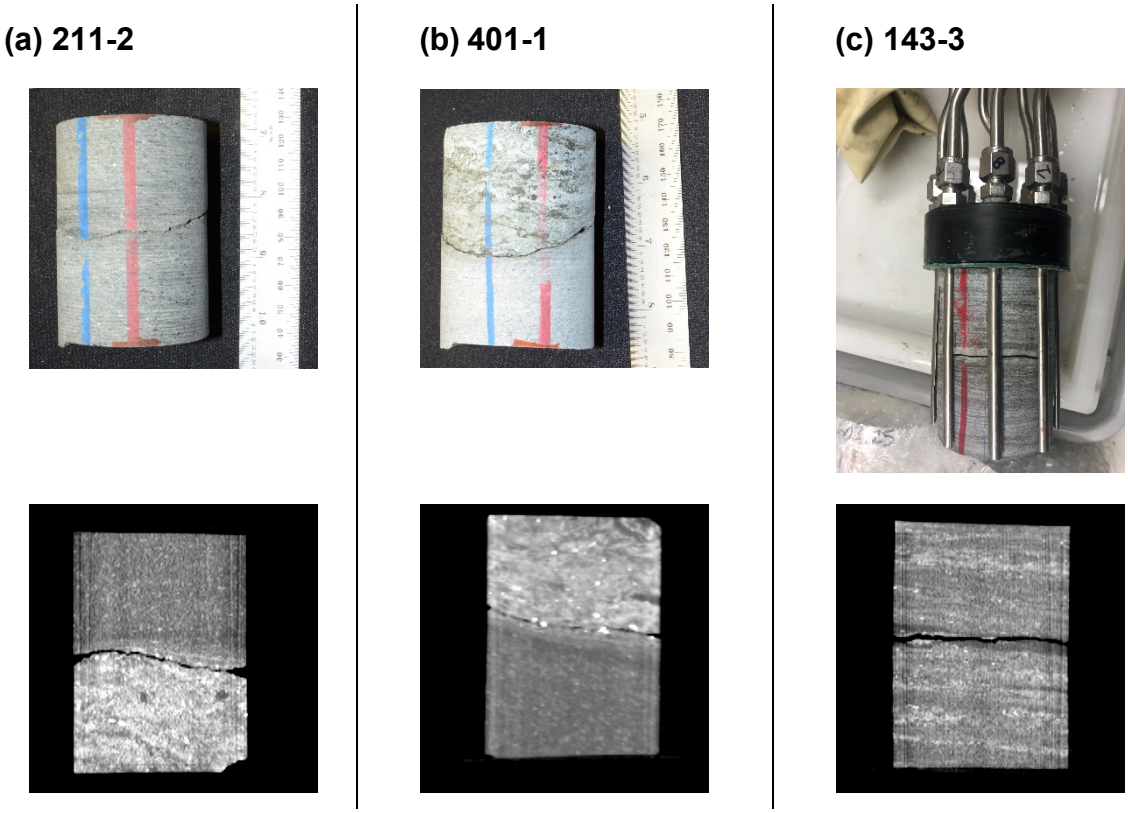

Figure 3-18. Natural Cores. Top row are images of fractures with 143-4 shown in core holder for experiment prior to the placement of the custom sleeve. Second row of images are x-ray CT scans of the fractures that were used for determination of average aperture.

3.7.4 Transmissivity Results

Transmissivity results for the artificial fractures are shown in Table 3-4. As reported previously, when AF1 was tested, the channel was aligned with the through-hole, and very low to no differential pressure was observed indicating that flow was not restricted. The T was recorded as infinite '∞', although if the flow rate was increased some flow restriction would have eventually been observed, but this was not attempted as it may have potentially damaged the apparatus. When the valves were adjusted to align away from the through-hole (solid Delrin), no flow was observed and the differential pressure steadily climbed until nearing the pressure limit of the flow system (20 psi), indicating that no flow occurred. Pressure was set on the no flow position (without the hole) for a period of 1 hour each, and no pressure drop was observed, further indicating that no circumferential flow occurred.

For AF2 and AF3, transmissivities were measured over a range of effective stresses (200 to 1100 psi) and flow rates. The flow rates were dependent on the core transmissivity, and were adjusted to give a differential pressure within the range of the sensor. AF2, with the defined straight channels, as expected showed increasing T with channel size. However, for the smaller two channels not much difference was seen. This may be due to one of the fundamental difficulties of the apparatus, trapping of air bubbles in the flow path. With these small channels this could be a major problem, so plans are to repeat this measurement to confirm results. For AF3, the results show minor differences in transmissivities for each channel. The differences in these channel geometries was due more to flow path length as opposed to flow cross section.

Transmissivity results for the natural fractures are shown in Table 3-5. These numbers represent an average number (n=10) differential pressure measurements at the confining pressure listed in the table and were measured for at least 3 flow rates. To measure each T value, there were first hundreds of measurements made for each of the flow paths to determine that the flow was stable and repeatable. The measurements started with low confining pressure and the confining pressure was gradually increased, raising the effective stress. In every case, settling of the fracture was observed, which was demonstrated by decreasing measured T with increasing confining pressure. After a few cycles the transmissivity decrease was no longer observed and a new set of measurements was taken with the 'settled' fracture. Results of the measurements as shown in Table 3-5 demonstrate that all three fractures have distinct permeability values, with the 211-2 fracture and the 143-4 fracture in the 10^{-5} m^2/s range, and the 401-1 showing lower permeability, in the 10^{-7} m^2/s range. Anisotropy differences are in the range of factors of 2 to 4, and some minor differences are seen in the measurements in the forward and reverse direction of 401-1.

Table 3-4. Results of measurements of transmissivity of the artificial fractures (AF).

	1 → 5 T (m^2/s)	**2 → 6** T (m^2/s)	**3 → 7** T (m^2/s)	**4→ 8** T (m^2/s)
AF-1	∞	0	0	0
AF-2	1.4×10^{-7}	2.2×10^{-7}	8.0×10^{-5}	1.3×10^{-4}
AF-3	4.0×10^{-5}	2.0×10^{-5}	5.7×10^{-5}	3.5×10^{-5}

Table 3-5. Results of measurements of transmissivity of the three fractures.

	Confining pressure (psi)	**1 → 5 (5→1)** T (m^2/s)	**2 → 6 (6→2)** T (m^2/s)	**3 → 7 (7→3)** T (m^2/s)	**4→ 8 (8→4)** T (m^2/s)
211-2	1000	4.0×10^{-5}	3.0×10^{-5}	1.0×10^{-4}	1.3×10^{-4}
401-1	1100	2.6×10^{-7} (2.1×10^{-7})	2.8×10^{-7} (2.3×10^{-7})	4.2×10^{-7} (3.3×10^{-7})	3.8×10^{-7} (2.3×10^{-7})
143-4	2000	3.0×10^{-5}	7.5×10^{-5}	7.4×10^{-5}	5.5×10^{-5}

3.7.5 Future Work

Future work will involve comparing current laboratory measurements with field measurements of transmissivity to help understand if this measurement technique is realistically representing transmissivities measured in the field. In addition, some additional work is in process measuring the aperture of the natural fractures to aid in numerical modelling. Finally, the large number of measurements of transmissivity in the lab will undergo further statistical testing to verify differences observed with flow path are significant.

3.8 Numerical Modeling of Previous Core Experiments

3.8.1 Motivation

We want to gain insight into laboratory experiments on fluid flow through fractured cores. Experiments are run by imposing flow *Q* between pairs of ports surrounding the core, and measuring the pressure difference (DP). This is done at a series of confining pressures between 200 and 4500 psi. Typical flow rates used are 5, 10, 15, and 20 cm^3/s. Then we use DP and Q with Darcy's law to determine the transmissivity T of the flow paths.

Figure 3-19a and Table 3-6 summarize results from previous years' work for Core 211-2. After a preliminary "settling period", T does not vary with confining pressure, and the T dependence on Q closely conforms to Darcy's law. There are consistent T differences between port pairs, with flow paths 4-8 and 3-7 showing higher T than flow paths 1-5 and 2-6, suggesting that the fracture may have anisotropic transmissivity, as illustrated schematically in Figure 3-18b. The goal of the modeling study is to investigate this hypothesis.

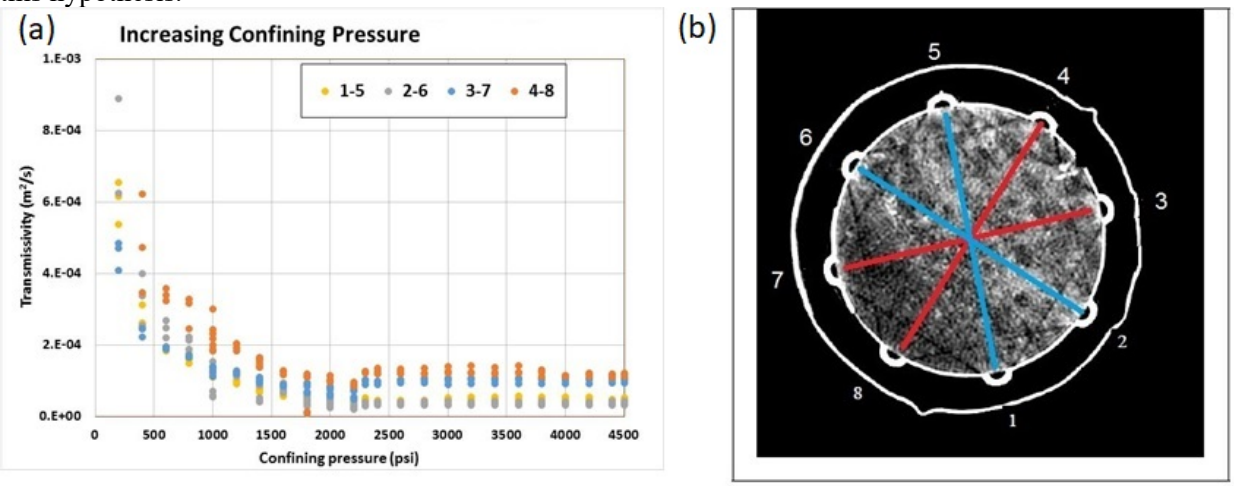

Figure 3-19. Results from previous year's lab experiments (Dobson et al., 2016, 2017; Zheng et al., 2018) on Core 211-2. (a) transmissivity T inferred from pressure difference DP between different port pairs. (b) schematic interpretation of T variations, with red indicating high-T flow paths and blue indicating low-T flow paths. Ports are labeled by number from 1 to 8. Note that in subsequent images the core is rotated so that Port 8 is on top.

Table 3-6. Summary of T values from previous years' studies on Core 211-2.

Port Pair	T (m^2/s)	Ratio T/T_{max}	Comment
4-8	1.3E-4	1.00	Maximum T
3-7	1.0E-4	0.77	High T
1-5	4E-5	0.31	Low T
2-6	3E-5	0.23	Minimum T

3.8.2 Data Used

The primary data used to develop the numerical model is the aperture distribution obtained by x-ray CT scanning the core, shown in Figure 3-20. The scan is composed of 512 x 512 measurements, at a spatial resolution 0.195 mm. The core itself, about 6 cm in diameter, is represented by a smaller number of measurements, 310 x 310. In the scan, measurements are ordered from left to right (I) and top to bottom (J). In order to plot the picture right-side up (by convention with Port 8 on top), a variable oppJ = -J is used. A threshold of 999 microns is applied, so any measurements greater than 999 are shown as 999. The port locations are visible in Figure 3-20. Ports are half-tubes with a diameter of 4.5 mm. The summary of T results from previous years are labeled on Figure 3-20, and detailed in Table 3-6.

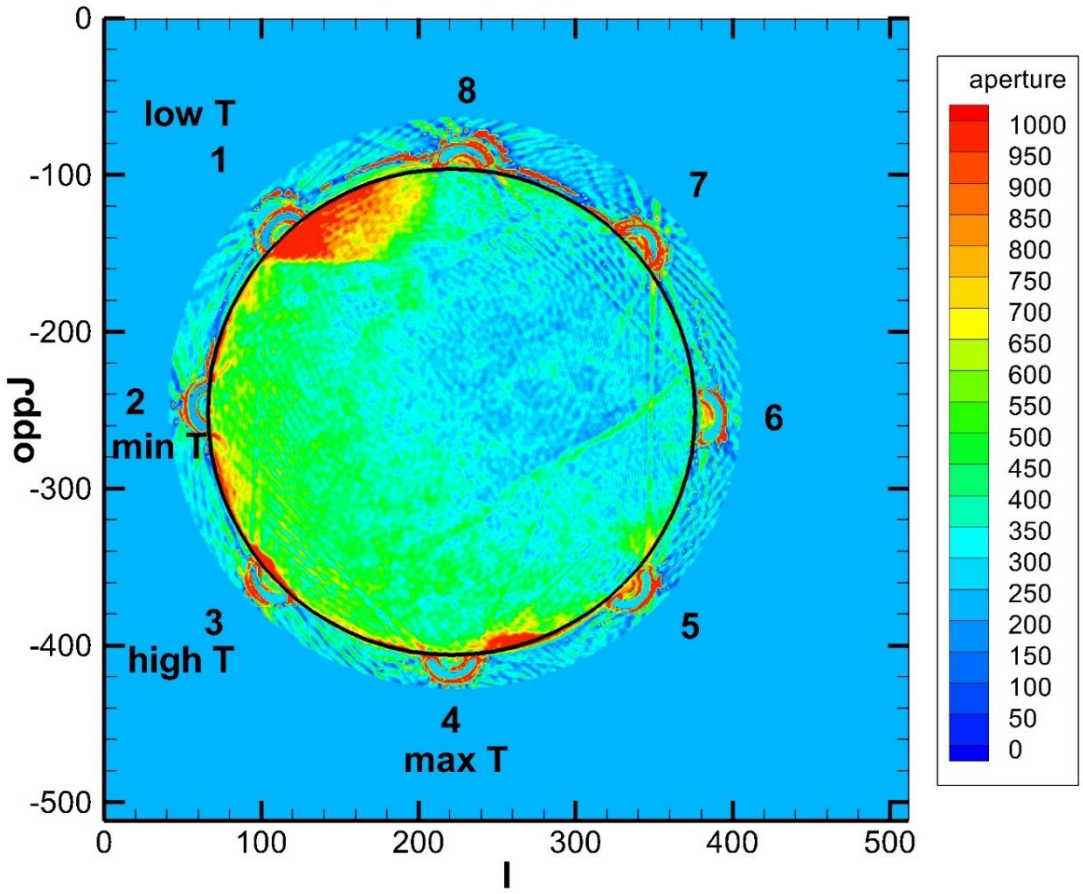

Figure 3-20. Core 211-2 scanned aperture distribution (microns) with a threshold of 999. The black circle is the interpreted edge of the core, which will be used for numerical model development, described below.

Figure 3-21 shows the distribution of apertures from the scan of Core 211-2. The arithmetic mean aperture is 292 microns. Note that values of 999 and 250 do not all represent actual measurements: 999 is the upper threshold and 250 is the background aperture outside the core. These values are omitted from averaging.

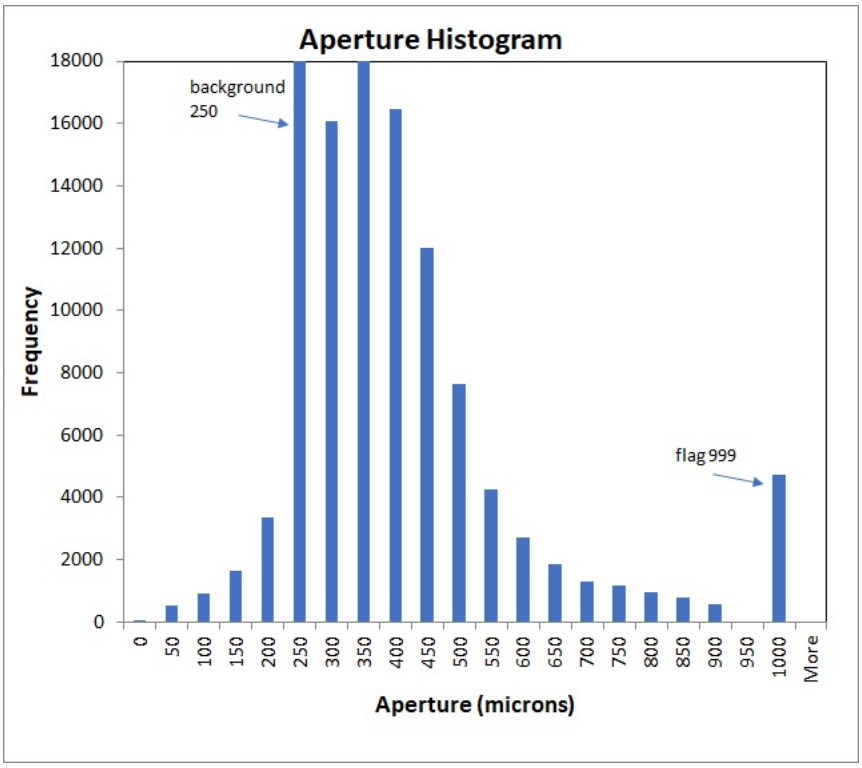

Figure 3-21. Aperture distribution for Core 211-2.

3.8.3 Model Development

3.8.3.1 General

The numerical simulator used is TOUGH3 with equation of state package EOS1, which considers a single-component (water). Here, we consider water as a single-phase liquid, flowing under isothermal conditions.

Lab experiments were done at multiple confining pressures resulting in different effective stresses, with the presumption that the aperture distribution changes with confining pressure (effective stress). Here we just use one fixed aperture distribution, equivalent to one confining pressure. Furthermore, we just use one flow rate, Q = 10 cm^3/s (0.01 kg/s), since the lab experiments verified that DP was proportional to Q.

3.8.3.2 Create Grid

The scan represents the aperture distribution in the core with resolution of 0.195 mm, on a 310 x 310 grid. For computational efficiency, it was decided to use grid blocks 0.39 mm wide, on a 155 x 155 grid. The grid generator AMESH was used to create a two-dimensional regular rectangular grid with uniform thickness to represent the fracture. As described below, the variable aperture will be represented by a variable permeability field.

3.8.3.3 Assign aperture distribution as permeability field

Because the model grid resolution is half that of the scan, arithmetic averaging over 2 by 2 squares of scan measurements is done to create an aperture distribution for the model. Then the cubic law is used to convert aperture to a permeability modifier (PM) for each grid block. Specifically

$$PM = (b/b_{avg})^3$$

where b is the aperture for the model grid block, and b_{avg} = 292 microns is the average aperture.

After the permeability modifiers are applied, the model is trimmed to a circle shown in Figure 3-20. Ports are assigned as adjacent high-permeability grid blocks by visual inspection of Figure 3-20. The resulting model is shown in Figure 3-22.

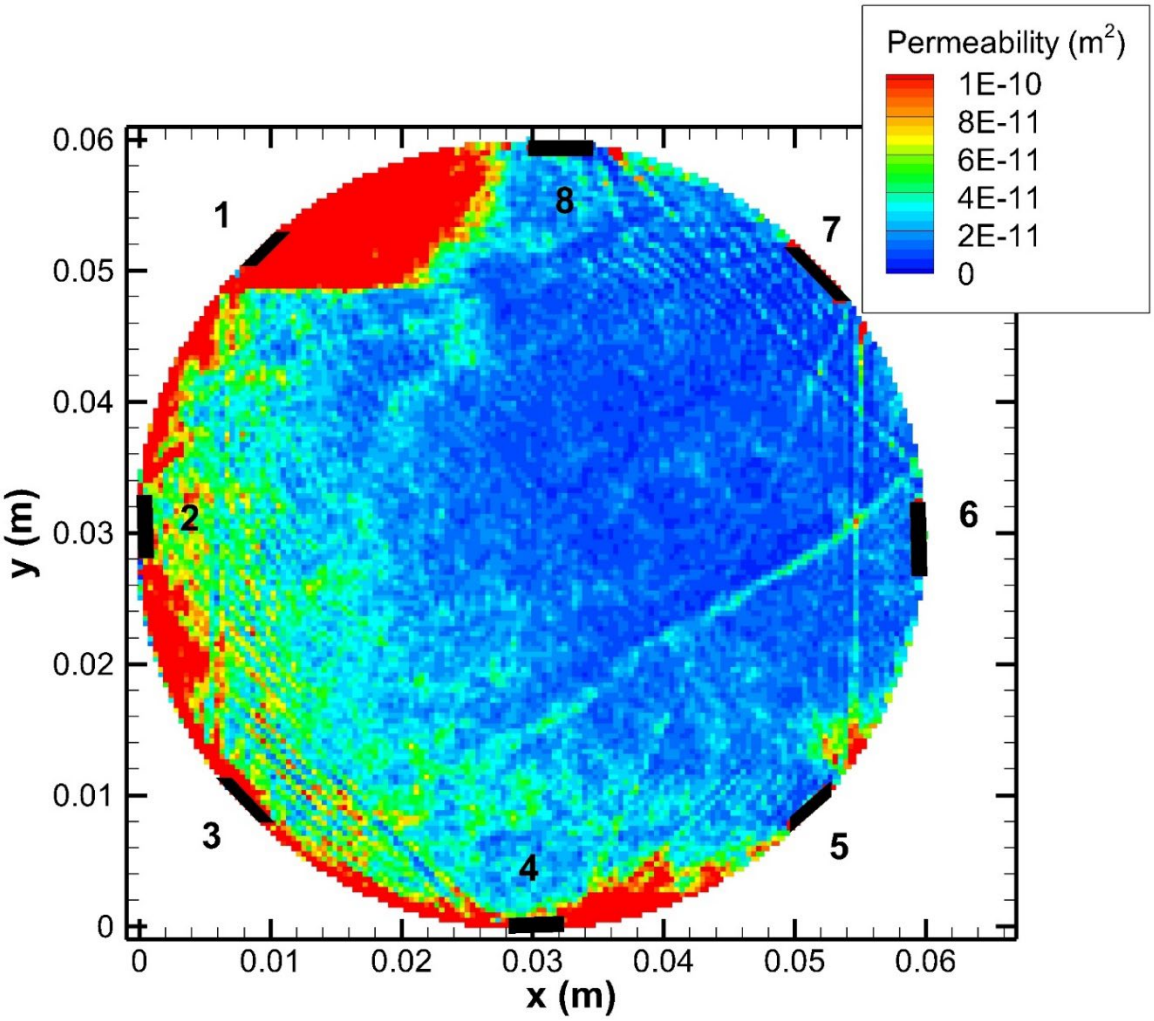

Figure 3-22. Permeability distribution for the numerical model of Core 211-2. Port locations are shown by black bars. Some of the high permeability pathways are X-ray CT artifacts.

Figure 3-23 shows the distribution of permeability modifiers, sorted from small to large over the 18,603 grid blocks of the model. Permeability modifiers range from approximately 0.01 to 30. A few grid blocks have the upper threshold permeability, which is shown by a permeability modifier of 40.

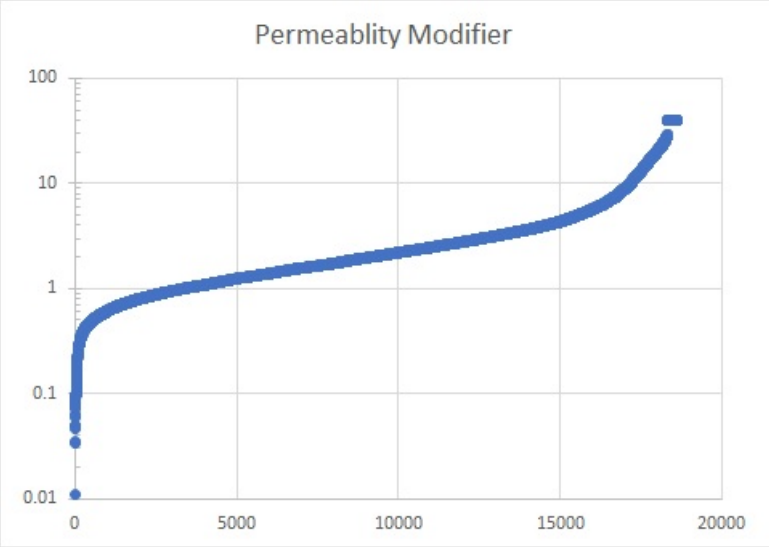

Figure 3-23. Distribution of permeability modifiers used to represent the variable aperture of Core 211-2.

3.8.3.4 Assign source and sinks to ports

Port locations are identified from Figure 3-20, and port grid blocks are given a separate material type in the TOUGH3 model. This material has a high porosity (0.99) and permeability (about 1000 times higher than the fracture permeability). Each port is about 10 grid blocks wide. The center grid block of each port is assigned as a source (ports 1, 2, 3, 4) or sink (ports 5, 6, 7, 8). The simulation period is divided into four time periods. During each period one pair of ports (1 and 5, 2 and 6, 3 and 7, 4 and 8) is assigned a positive flow rate of 0.01 kg/s at the source port and a negative flow rate of -0.01 kg/s at the sink port, with all other flow rates being zero for that time period.

3.8.3.5 Other properties

The porosity is set to 0.5 and rock compressibility is set to 1E-9 Pa^{-1}. The base permeability is calculated from the cubic law for the average aperture, and is 2E-12 m^2. For each grid block, base permeability is multiplied by the permeability modifier for that grid block.

3.8.4 Results

3.8.4.1 Pressure

In the laboratory experiments, typical pressure differences for a flow rate of 10 cm^3/s were less than 1000 Pa, whereas in the preliminary simulations with the numerical model they were about ten times greater. So, the first adjustment made to the model was to increase the base permeability and the port permeability each by a factor of ten. Unfortunately, the model would not run stably with such high port permeability. Therefore, the port permeability was returned to its original value (1E-9 m^2) and the base permeability was reduced to 1E-11 m^2. With these changes, the model runs stably and typical pressure changes are the same order of magnitude as obtained in the lab.

Plotting pressure as a function of time for the sources and sinks (not shown) indicates that steady state is achieved rapidly, within 0.01 s. Thus, each of the four time periods for the model, during which flow occurs

for different port pairs, is set at 0.01 s. Figure 3-24 shows the pressure distributions at the end of each time period.

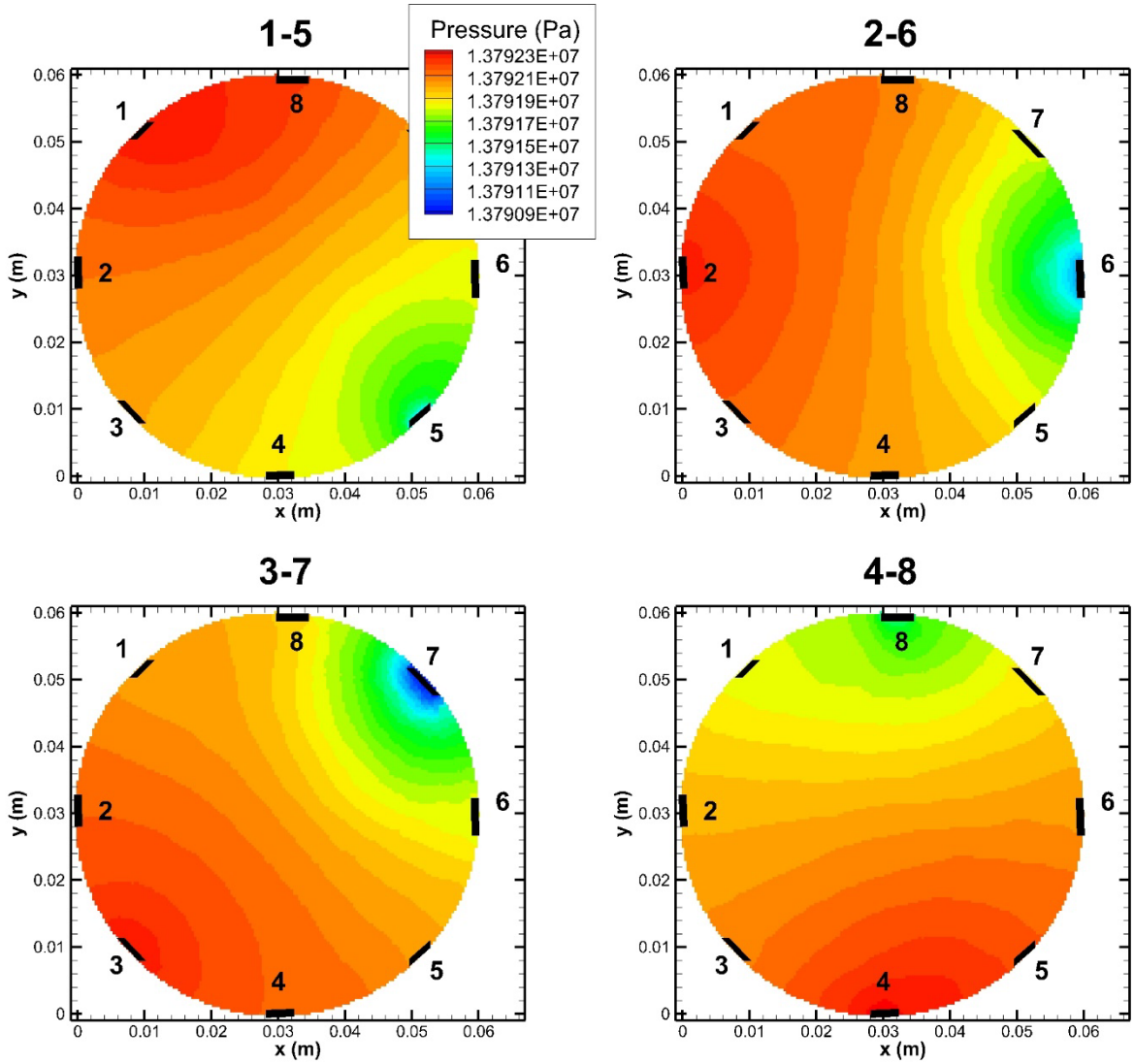

Figure 3-24. Modeled steady-state pressure distributions for the four different port pairs.

Table 3-7 summarizes the pressure differences (DP) for the four port pairs. Since DP is inversely proportional to transmissivity T, DP/DPmin = 1/(T/Tmax), which can be compared to lab values. There is reasonable agreement between model and lab for the high-permeability flow paths 4-8 and 3-7, but the model transmissivity for the low-permeability flow paths 1-5 and 2-6 is too high.

Table 3-7. Comparison of model and lab transmissivity results.

Port Pair	Model DP (Pa)	Model DP/DPmin	Model T/Tmax	Lab T/Tmax
4-8	862	1.00	1.00	1.00
3-7	1385	1.61	0.62	0.77
1-5	927	1.07	0.93	0.31
2-6	1141	1.32	0.76	0.23

3.8.4.2 Flow field

It is valuable to examine the flow field across the fracture, to see what the T values inferred from the pressure difference represent. One way to plot the flow field is as a vector plot, but the great variation in flow magnitude near and far from ports makes it very difficult to interpret such plots. A better means of visualizing the flow field is by plotting streamtraces. Figure 3-25 shows the grid near Port 1. In this representation, grid block centers are at the intersections of the black lines. The blue circles identify grid blocks that represent the port, and the filled blue circle represents the source grid block. Streamtraces (red lines) are initiated along a line that spans the extent of the port. For each port pair, the same number of streamtraces are initiated.

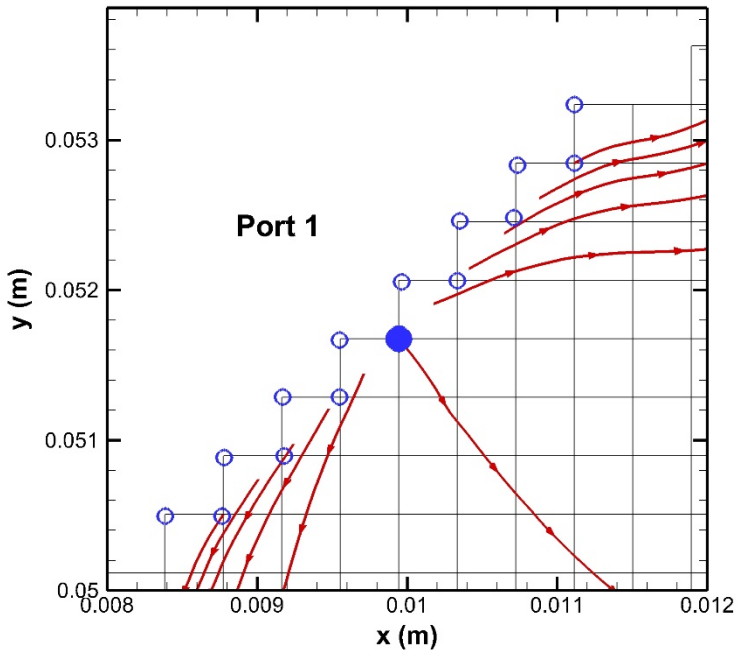

Figure 3-25. Detail of numerical grid around Port 1, illustrating how streamtraces are initiated.

Streamtrace plots are shown in Figure 3-26. The focusing of the streamtraces in the high-permeability portion of the core is apparent.

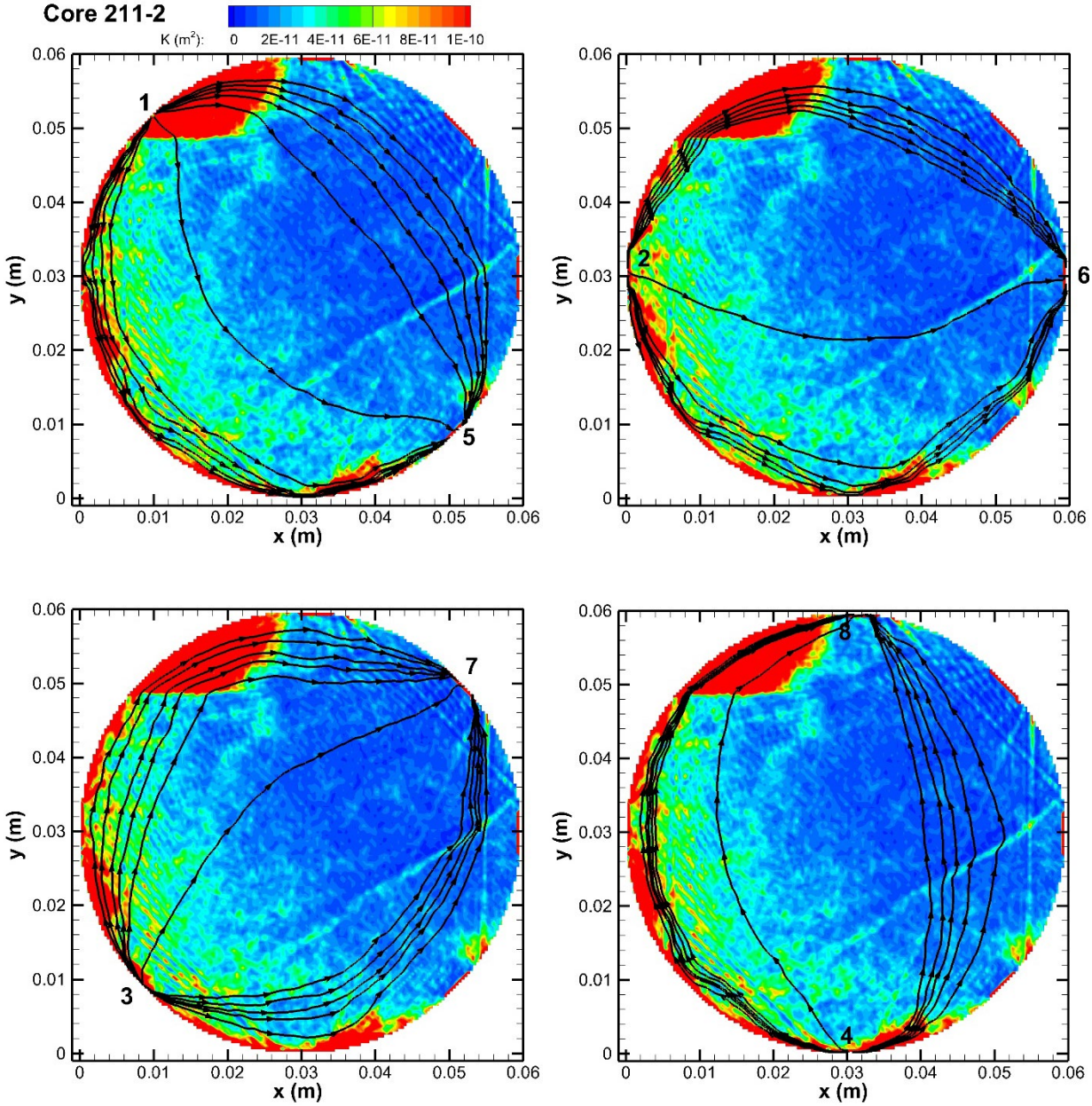

Figure 3-26. Streamtrace **plots showing modeled flow field.**

3.8.5 Discussion

The original premise to explain the variability in transmissivity T between different port pairs (Table 3-7) was that the fracture T field was anisotropic. Examination of the flow fields does not support the hypothesis that flow is controlled by an overall anisotropic transmissivity distribution, but rather by local heterogeneity. However, model results for T values for different port pairs are not completely consistent with lab results (Table 3-7), so these conclusions must be seen as preliminary. An additional shortcoming

of the model is that when a port is not being used for inflow or outflow during a given flow period, it still has a high permeability, and some of the flow paths near the outer edge of the core deviate from the path they should be taking and go through these high-permeability locations.

The model can be adjusted to try to better replicate lab results. Technical adjustments such as redrawing the black circle in Figure 3-20 that denotes the model outer boundary to include less of the very high permeability around the circumference of the core might be helpful, as will a more sophisticated representation of the ports. At a more conceptual level, the aperture distribution obtained by the scan might be decreased by a constant amount, to represent closing of the fracture due to increased confining pressure. Once the model better reproduces the lab results for transmissivity for various port pairs, its flow paths will be more reliable.

Because the model here is so much smaller than typical TOUGH3 models, which usually cover many meters or even many kilometers, care had to be taken to ensure that small spatial scales, short time scales, and small pressure differences were properly resolved. For example, in the main TOUGH3 output, not enough significant figures of pressure are shown to indicate that any change in pressure occurs when flow between ports is imposed. However, internally, TOUGH3 does use enough significant figures to properly calculate small pressure changes, and these are recorded in subsidiary output files.

3.8.6 Conclusion and Future Work

Numerical simulation of the laboratory experiments on flow through fractured cores demonstrated that the method works in principle, but model improvements are needed to make a compelling case that the model really captures the essence of lab behavior. Preliminary modeling results suggest that fracture anisotropy is not the dominant feature producing variable transmissivity values for flow between different port pairs, but rather local heterogeneity in the aperture distribution is responsible.

Technical and conceptual adjustments to the model, described in the previous section, will be carried out in an attempt to improve agreement between model and lab results.

Additionally, models will be developed of other cores whose aperture distribution has been scanned. Now that technical details involving creating models on these small spatial and time scales have been worked out, creating other models will be more efficient.

4. SUMMARY OF FY20 RESEARCH ACTIVITIES AND DIRECTIONS OF FUTURE RESEARCH

In FY20, to support the modeling of fluid flow and transport in fractured crystalline rocks, LBNL's research activities have focused on reducing the uncertainties of key flow parameters used for modeling of the EDZ. Research activities included laboratory experiments to study time-dependent rock deformation of crystalline rock under stress and high temperature conditions, and a field test conducted in the COSC-1 borehole (Sweden) via international collaboration. The work has been conducted according to the scope of work of two work packages: SF-20LB01030207 "Crystalline International Collaborations – LBNL," and SF-20LB01030203 "Crystalline Disposal R&D – LBNL," as part of the Work Package on the Crystalline Disposal R&D. A brief summary of the accomplishments in FY20 and directions of future research in the remaining time of FY20 and FY21 are as follows:

In Section 2, we presented the development of a high pressure (up to 10,000 psi), high temperature (up to 200˚C) triaxial loading system that enables long-term (days to months) simultaneous laboratory experiments on multiple core-scale samples under temperature-controlled flow, mechanical, and chemical conditions. We also developed and used the system for measurements of permeability of granite samples obtained from the Grimsel URL.

Because heterogeneity and anisotropy of rock may greatly impact the time-dependent rock creeping subjected to triaxial stress, under the influence of elevated temperature and fluid chemistry, we will conduct rate-dependent strength and creep tests of the samples for relatively long time (up to ~1 week). Unfortunately, due to the COVID-19 pandemic and a shelter-in-place order, the planned creep tests have been delayed. We will resume the experiments as soon as our access to the laboratory is permitted. We are going to perform additional characterization tests to better understand the mechanical, chemical and microstructural properties of the rock.

In Section 3, we presented the results of investigations conducted by LBNL researchers in collaboration with the Collisional Orogeny in the Scandinavian Caledonides (COSC) scientific team. The research activities were conducted using the COSC-1 borehole as a testbed to evaluate the hydrology of a crystalline basement environment. This research is aimed at providing insights on the problem of nuclear waste disposal in crystalline formations. In June of 2019, the LBNL team deployed a unique borehole monitoring tool, called Step-rate Injection Method for Fracture In-situ Properties (SIMFIP), to measure real-time 3D mechanical deformation of rock within three intervals of the COSC-1 borehole. The following field tests were carried out: pressure buildup tests, pressure falloff tests, and constant flow rate tests for each of the three intervals. Two approaches were used to evaluate the stress conditions: an inversion of the displacement data, and a fully coupled numerical simulation of fracture stimulation and fluid flow using the distinct element code 3DEC. These analyses provided insights into the stress state for the borehole intervals, as well as how the fractures responded to hydraulic stimulation. Laboratory and modeling investigations were conducted on COSC-1 core samples that correspond with the borehole intervals tested in the field. Future research activities include conducting modeling to assess far-field effects of the hydraulic stimulation of these intervals, additional rock property measurements on selected core samples, and obtaining new borehole televiewer images to better characterize the fractures that were opened at each of the three tested intervals with the application of the SIMFIP. Our collaborators at Uppsala University are conducting additional numerical simulations of the fracture flow tests. Preliminary results of these investigations were presented "virtually" at the 2020 EGU annual meeting (Basirit et al., 2020; Tatomir et al., 2020). The COSC team is currently drilling a new deep borehole (COSC-2), so there may be additional opportunities for conducting tests in this new well.

This page is intentionally left blank.

5. ACKNOWLEDGMENTS

We thank the members of the COSC scientific team for generously sharing their data and ideas on the COSC-1 project. The International Continental Scientific Drilling Program (ICDP) and the Swedish Research Council financed the drilling of the COSC-1 borehole (VR: Grant 2013–94). We also thank Yuxin Wu, LianGe Zheng, and Timothy Kneafsey for their scientific review of this work, and Boris Faybishenko and Cynthia Tilton for their editorial reviews. Funding for this work was provided by the Spent Fuel and Waste Disposition Science and Technology Campaign, Office of Nuclear Energy, of the U.S. Department of Energy under Contract Number DE-AC02-05CH11231 with Lawrence Berkeley National Laboratory and a grant by the Swedish Geological Survey to Prof. Auli Niemi of Uppsala University (research contract 36-2025-2018). We thank Florian Kober of NAGRA for providing us with the Grimsel granite sample.

This page is intentionally left blank.

6. REFERENCES

Basirat, F., Tsang, C.-F., Tatomir, A., Guglielmi, Y., Dobson, P., Cook, P., Juhlin, C., and Niemi, A. (2020) Analysis of flow and pressure data for the estimation of fracture generation and propagation – first model results from coupled hydromechanical experiments in COSC-1 borehole in deep crystalline rock, Åre, Sweden, EGU General Assembly 2020, Online, 4–8 May 2020, https://doi.org/10.5194/egusphere-egu2020-7914, 2020

Bieniawski, Z.T. (1989) Engineering rock mass classifications: a complete manual for engineers and geologists in mining, civil, and petroleum engineering.

Wiley-Interscience, 40–47. ISBN 0-471-60172-1.

Bossart, P., and Mazurek, M. (1991) Grimsel Test Site—structural geology and water flow-paths in the migration shear-zone. Nagra Tech Rep NTB 91–12, Nagra, Wettingten, Switzerland.

Bredehoeft, J.D., and Maini, T. (1981) Strategy for radioactive waste disposal in crystalline rocks. Science, 423 (4505), 293–296.

Brown, D. (1989) The flow of water and displacement of hydrocarbons in fractured chalk reservoirs. In: Fluid Flow in Sedimentary Basins and Aquifers. J. C. Goff and B. P. Williams, eds., Geological Society London, 201–218.

Chen, L., De'Haven Hyman, J., Lei, Z., Min, T., Kang, Q., Rougier, E., and Viswanathan, H. (2019) Effect of fracture density on effective permeability of matrix-fracture system in shale formations. In: Geological Carbon Storage: Subsurface Seals and Caprock Integrity, S. Vialle, J. Ajo-Franklin, and J.W. Carey, eds., AGU Geophysical Monograph 238, John Wiley & Sons, 137–146.

Cherry, J.A., Alley, W.M., and Parker, B.L. (2014) Geologic disposal of spent nuclear fuel – An earth science perspective. The Bridge, Spring 2014, 51–59.

David, C., Wassermann, J., Amann, F., Klaver, J., Davy, C., et al., (2018a) KG2B, a collaborative benchmarking exercise for estimating the permeability of the Grimsel granodiorite – Part 1: measurements, pressure dependence and pore-fluid effects, Geophysical Journal International, 215, 799–824.

David, C., Wassermann, J., Amann, F., Klaver, J., Davy, C., et al., (2018b) KG^2B, a collaborative benchmarking exercise for estimating the permeability of the Grimsel granodiorite-Part 2: modelling, microstructures and complementary data. Geophysical Journal International, 215 (2), 825-843.

Dessirier, B., Tsang, C.F., Hedayati, M., Lorenz, H., Juhlin, C., and Niemi, A. (submitted) A study of correlations of geophysical and geochemical logs with hydrogeologic features in a 2.5-km deep borehole in crystalline rock. Paper submitted for publication to Hydrogeology Journal.

Detournay, E., and Carbonell, E. (1997) Fracture mechanics analysis of the breakdown process in minifracture or leakoff test. SPE paper 28076, Soc. Pet. Eng. Prod. Facil., 12, 195–199.

Dobson, P., Tsang, C.F., Doughty, C., Ahonen, L., Kietäväinen, R., Juhlin, C., Rosberg, J.E., Borglin, S., Kneafsey, T., Rutqvist, J., Zheng, L., Xu, H., Nakagawa, S., and Nihei, K. (2017) Deep borehole field test activities at LBNL 2017. US DOE Spent Fuel and Waste Science and Technology, SFWD-SFWST-2017-000046, LBNL Report 2001043, 118 p.

Dobson, P., Tsang, C.-F., Kneafsey, T., Borglin, S., Piceno, Y., Andersen, G., Nakagawa, S., Nihei, K., Rutqvist, J., Doughty, C.,and Reagan, M. (2016) Deep borehole field test research activities at LBNL. US DOE Spent Fuel and Waste Science and Technology, FCRD-UFD-2016-000438, LBNL Report 1006044, 124 p.

Doughty, C., Tsang, C.F., Rosberg, J.E., Juhlin, C., Dobson, P.F., and Birkholzer, J.T. (2017) Flowing fluid electrical conductivity logging of a deep borehole during and following drilling: estimation of

transmissivity, water salinity and hydraulic head of conductive zones. Hydrogeology Journal, 25, 501–517.

Follin, S., Hartley, L., Rhén, I., Jackson, P., Joyce, S., Roberts, D., and Swift, B. (2014) A methodology to constrain the parameters of a hydrogeological discrete fracture network model for sparsely fractured crystalline rock, exemplified by data from the proposed high-level nuclear waste repository site at Forsmark, Sweden. Hydrogeology Journal, 22, 313–331.

Guglielmi, Y., Cappa, F., Avouac, J.-P., Henry, P., and Elsworth, D. (2015) Seismicity triggered by fluid injection–induced aseismic slip. Science, 348(6240), 1224.

Guglielmi, Y., Cappa, F., Lançon, H., Janowczyk, J.B., Rutqvist, J., Tsang, C.F., and Wang, J.S.Y. (2013) ISRM Suggested Method for Step-Rate Injection Method for Fracture In-Situ Properties (SIMFIP): Using a 3-Components Borehole Deformation Sensor, in The ISRM Suggested Methods for Rock Characterization, Testing and Monitoring: 2007–2014, edited by R. Ulusay, Springer-Verlag, Wein, doi:DOI: 10.1007/978-3-319-07713-0.

Guglielmi, Y., Cook, P., Dobson, P., Nakagawa, S., Zheng, L., Niemi, A., Juhlin, C., Lorenz, H., Rosberg, J.-E., Dessirier, B., Tsang, C.-F., Tatomir, A., Basirat, F., Lundberg, E., Almqvist, B., Borglin, S., and Doughty, C. (2019) Crystalline Disposal R&D at LBNL: FY19 Progress Report. US DOE Spent Fuel and Waste Science and Technology, LBNL Report 2001221, 32 p.

Guglielmi, Y., Nussbaum, C., Rutqvist, J., Cappa, F., Jeanne, P. and Birkholzer, J. (2020) Estimating perturbed stress from 3-D borehole displacements induced by fluid injection in fractured or faulted shales. Geophys. J. Int., 221, 1684–1695.

Hadgu, T., Karra, S., Kalinina, E., Makedonska, N., Hyman, J.D., Klise, K., Viswanathan, H.S., and Wang, Y. (2017) A comparative study of discrete fracture network and equivalent continuum models for simulating flow and transport in the far field of a hypothetical nuclear waste repository in crystalline host rock. Journal of Hydrology, 553, 59–70.

Hedin, P., Almqvist, B., Berthet, T., Juhlin, C., Buske, S., Simon, H., Giese, R., Krauß, F., Roseberg, J.-E., and Alm, P.-G. (2016) 3D reflection seismic imaging at the 2.5 km deep COSC-1 scientific borehole, central Scandinavian Caledonides. Tectonophysics, 689, 40–55.

Itasca Consulting Group (2016) 3DEC, 3-Dimensional Distinct Element Code. Itasca Consulting Group, Minneapolis, MN.

Kakurina, M., Guglielmi, Y., Nussbaum, C., and Valley, B. (2019) Slip perturbation during fault reactivation by a fluid injection. Tectonophysics, 757, 140–152.

Kakurina, M., Guglielmi, Y., Nussbaum, C., and Valley, B. (submitted). Stress state estimation from fluid induced fault dislocation data. Paper submitted for publication to Tectonophysics.

Keusen, H.R., Ganguin, J., Schuler, P., and Buletti, M. (1989) Grimsel Test Site: Geology. NAGRA, Baden, Technical Report 87-14 (NTB 87-14E).

Lajtai, E.Z., Duncan, E.J.S., and Carter, B.J. (1991) The effect of strain rate on rock strength, Rock Mechanics and Rock Engineering, 24: 99. https://doi.org/10.1007/BF01032501

Lorenz, H., Rosberg, J.E., Juhlin, C., Bjelm, L., Almqvist, B.S.G., Berthet, T., Conze, R., Gee, D.G., Klonowska, I., Pascal, C., Pedersen, K., Roberts, N.M.W., and Tsang, C.F. (2015) COSC-1 –drilling of a subduction-related allochthon in the Palaeozoic Caledonide orogen of Scandinavia, Scientific Drilling, 19, 1–11.

Makedonska, N., Jafarov, E., Doe, T., Schwering, P., Neupane, G., and the EGS Collab team. (2020) Simulation of injected flow pathways in geothermal fractured reservoir using discrete fracture network

model. Proceedings, 45th Workshop on Geothermal Reservoir Engineering, Stanford University, SGP-TR-216, 12 p.

Stephansson, O., Ljunggren, C. and Jing, L. (1991) Stress measurements and tectonic implications for Fennoscandia. Tectonophysics, 189, 317-322.

Tatomir, A., Basirat, F., Tsang, C.-F., Guglielmi, Y., Dobson, P., Cook, P., Juhlin, C., and Niemi, A. (2020) Coupled Hydro-Mechanical Modeling of Fracture Normal Displacement and Fluid Pressures during a SIMFIP (step-rate injection method for fracture in-situ properties) Test, EGU General Assembly 2020, Online, 4–8 May 2020, https://doi.org/10.5194/egusphere-egu2020-7387, 2020

Tsang, C.F., Rosberg, J.E., Sharma, P., Berthet, T., Juhlin, C., and Niemi, A. (2016) Hydrologic testing during drilling: application of the flowing fluid electrical conductivity (FFEC) logging method to drilling of a deep borehole. Hydrogeology Journal, 24, 1333–1341.

Wenning, Q.C., Berthet, T., Ask, M., Zappone, A., Rosberg, J.-E., and Almqvist, B.S.G. (2017) Image log analysis of in situ stress orientation, breakout growth, and natural geologic structures to 2.5 km depth in central Scandinavian Caledonides: Results from the COSC-1 borehole. Journal of Geophysical Research Solid Earth, 122, 3999–4019.

Witherspoon, P.A., Cook, N.G.W., and Gale, J.E. (1981) Geologic storage of radioactive waste: Field studies in Sweden. Science, 211 (4485), 894–500.

Witherspoon, P.A., Wang, J.S.Y., Iwai, K., and Gale, J.E. (1980) Validity of cubic law for fluid flow in a deformable rock fracture. Water Resour. Res., 16(6), 1016–1024.

Zhang, F., Damjanac, B., and Maxwell, S. (2019) Investigating Hydraulic Fracturing Complexity in Naturally Fractured Rock Masses Using Fully Coupled Multiscale Numerical Modeling. Rock Mech. Rock Eng. https://doi.org/10.1007/s00603-019-01851-3

Zheng, L., Deng, H., Nakagawa, S., Kim, K., Kneafsey, T., Dobson, P., Borglin, S., Doughty, C., Voltolini, M., Tsang, C.F., Dessirier, B., Wenning, Q., and Juhlin, C. (2018) Crystalline Disposal R&D at LBNL: FY18 Progress Report. US DOE Spent Fuel and Waste Science and Technology, LBNL Report 2001177, 71 p.

This page is intentionally left blank.

APPENDIX 1 – FIELD NOTES FROM 2019 COSC-1 LOGGING CAMPAIGN

(Auli Niemi, Chris Juhlin, Pat Dobson, Paul Cook, Yves Gugluelmi, Henning Lorenz, Benoit Dessirier, Alexandru Tatomir, Farzad Basirat, Jan-Erik Rosberg, Emil Lundberg, Georgios Niachros, Niranjan Joshi, Bjarne Almqvist, Eduardo Reynolds, Roland Roberts)

June 3rd – Paul departed from San Francisco

June 4th – Pat and Yves departed from San Francisco. Paul arrived in Sweden and flew to Ostersund.

June 5th – Pat and Yves arrived in Stockholm and met up with Auli Niemi. We flew to Ostersund, meeting up with Paul at the airport. We picked up Benoit at the Ostersund railway station, and then headed up to Åre in two rental vehicles. Auli cautioned us to be careful driving – there are speed limit cameras along the road. We checked into our apartments, and then went into town to go shopping for food for breakfast and lunch. The card for the Uppsala account was not accepted as payment – Auli later fixed this problem. We ate an early dinner, and then drove out to the COSC-1 site. We met up with Henning, who had come earlier with a truck full of supplies from Uppsala. We saw the container, the generator, the water reservoirs, and the pallets of supplies that had been shipped from LBNL –everything seemed to have arrived in good order. The Pelican cases were not with the pallets, but we found out from Henning that he had secured them inside of the container. We then returned back to Åre for the evening.

Field site after delivery of generator, container, and LBNL shipment.

June 6th – We drove out to the work site at 9 a.m., and had a short safety briefing with the group – a key area of emphasis was using proper lifting techniques when dealing with all of the heavy gear. We proceeded to set up the two tents (one set up with its full length – 8 m by 5 m – work area for Yves and Paul; the second (set up as 6 m x 5 m, to fit in the available space) as a cover over the winch. We then placed the Uppsala winch into position, and secured it to trees to make sure that it was secure. We set up tables inside of the SIMFIP tent and got them level for a work space. We positioned the four large Pelican cases within the tent, and then took the SIMFIP out of its case and positioned it in pieces on the tables. We noticed that there was an oil leak in the generator, and that it would not run. We used power from some of the car batteries to help power some of our equipment. Auli has been fighting a cold but has been here leading our effort in spite of her condition. It rained a bit after we had set up the tents.


Assembly of tents for building the SIMFIP and hosting the winches.

Lessons learned – When the wind started to blow strongly, the top of the tent started to move. We need to make sure that the sides of the top of the tent are fastened securely to the frame.

June 7th – We arrived at the well site at around 8 a.m. The generator repairman came out to the site in the morning and fixed the generator. We installed two UPS units (one in each tent) in case the power went out during an experiment- they should not be used for powering the winch. We had a short safety briefing – key topics included electrical safety, tripping hazards, and proper lifting techniques. We had a group of students from Uppsala University who were doing field work in the area stop by for a quick visit – Yves gave a short briefing on the SIMFIP tool and what we planned to do with this project. We set up the tripod and prepared to run an initial EC/gamma/temperature log down the borehole. Before starting, we observed that there was a slight upflow out of the borehole. Jan-Erik and Emil started running the probe down the hole, but noticed that the temperature readings were way off. After additional calibration, the temperature values made sense, and we began running the logging tool down the hole. After some time, the tripod fell over, and we stopped the logging run to set up the tripod again, this time with two guy wires (ropes, actually) to make sure that it was secure. After some adjusting, we proceeded to finish logging as far as possible (~1217 m) – we were nearly at the end of the cable on the spool. We then logged back out of the borehole at a faster rate. Henning set up the pump, water line to the stream, and the water tank, which was placed on a berm overlooking the camp so that it would have gravity feed. He then proceeded to pump the 1000 L tank full with water. Paul and Yves continued to assemble the SIMFIP tool. When inserting a tube into the system, it caught on the blue fiber optic line and pinched it. When Paul and Yves hooked up the system to check it on the computer, it showed that the line was severed. They then took apart the system, verified that there was a kink in the fiber, cut out that section, and then made several tries to splice it, finally succeeding. The splicing tool is a bit problematic – it tends to spit out the spliced section rather violently when it completes the splice – this can then break the new spliced section. One of the pipe tightening tools broke (the cast iron frame cracked)– Paul created a replacement section by using metal bars made out of flattened stainless steel tubing and threaded bars – the threaded bar sections bent when the repaired tool was used, so we switched to pipe wrenches. Chris worked on getting the geophone array in the monitoring well set up properly. One key item is that many of us did not know how to properly use the port-a-potty in the trailer – it has a sliding plate needs to be opened when using the toilet and closed when finished – folks were using it when it was closed, so the toilet started to overflow!! We made sure that everyone was informed on the proper technique. We received the shipment of the 12 nitrogen tanks (the driver carefully maneuvered his truck between the winch and truck to place the tanks in our preferred location, and we also got a shipment of the regulator valve – however, this valve doesn't appear to be what we really wanted – it has a 200 bar inlet pressure (good) and a 40 bar outlet pressure (we had hoped for a 200 bar outlet pressure as well. Paul thinks that we can use this for deflating the packers at the shallower water depths, but it may be challenging

to do this at the deeper intervals – we need to check with the valve company on Monday. Auli organized a group photo of our team! We searched for a small brass nut that is part of the SIMFIP assembly, but could not find it anywhere. We also set up the downhole pump – adding two 50 m sections of yellow hose to the top of the pump. We secured the wire cable, the blue sheath around the power cable, and the yellow hose together with electrical tape about every 2.5 m, and set a mark with red tape at a depth of 75 m. The yellow hose tended to coil a bit – Henning worked hard to remove kinks from the line as we inserted it into the well. We then lowered the pump down hole to a depth of 75 m, and also placed an In-situ Troll tool downhole to monitor the temperature and the depth to the water column. The goal was to have a discharge flow rate of ~ 8 lpm – this was achieved by varying the motor frequency of the pump. It took around 2 hours to lower the water level to a depth of 75 meters. When this was achieved, the pump was turned off and we secured the camp, turning off the generator and the UPS units and closing up the tents. Auli brought everyone pizza to eat to cap off a very busy and productive day. Pat remained at the site overnight to keep watch. It rained during part of the afternoon and also during the night.

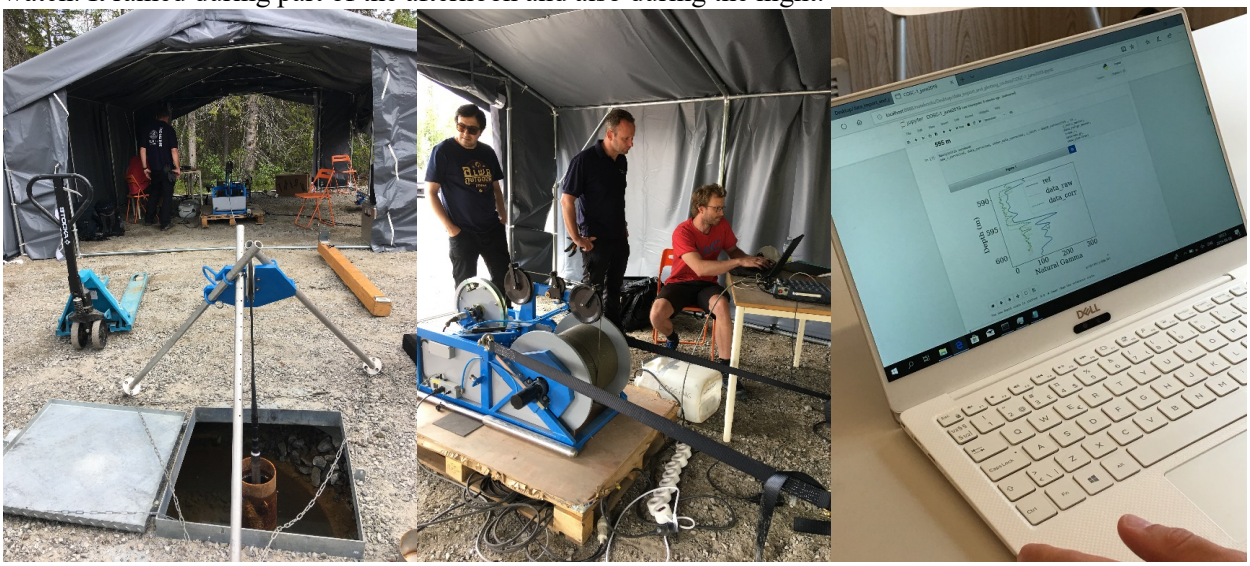

Gamma logging conducted successfully – see good match with previous data.

Deployment of downhole pump to lower head for FFEC logging run the next day.

Lessons learned – We need to make sure that all tripods and stands are properly anchored so that they don't tip and fall.

June 8th – We came out to the site at around 8 a.m. to begin work. Paul figured out that the missing nut was on top of another nut – that is why he could not tighten it properly! He removed the stacked nut from one hole and placed it in the correct location. We checked the water level in the borehole. It recovered to about 2 meters from the top of the borehole overnight. We restarted the generator and started up the pump again downhole to lower the water level back to 75 m. After the water level was lowered, the pump was pulled from the hole and Jan-Erik redeployed the EC/gamma/temperature logging tool to look for increased salinity zones associated with fluid inflow at the previously identified fracture zones. The other key objective was to confirm that we could reproduce the gamma log pattern, which we will be using to verify our borehole depths with the SIMFIP and gamma logging tool. Chin-Fu called Auli and Pat to ask about our progress, and requested that we keep detailed written records of our field activities – these may come in handy if we are trying to explain discrepancies in our data at a later date. Meanwhile, Chris and Emil proceeded to do two hammer seismic survey profiles (VSP style), stepping out with 5 hammer shots every 0.5 m in two orthogonal directions. Chris got all of the geophones to function (not bad for a 5 year old array). We had a quick safety briefing at the start of the survey, where we noted the need for safety glasses when using the sledge hammer, and also talked about tripping hazards – we put some flagging tape on the two stakes that helped anchor the tripod. We also mentioned that we need to take extra care to make sure that nothing falls down the borehole – we covered it with a board when it was open but not in use. Henning talked with Paul and Yves to find out more about the needs for supporting the different wires and tubing going underground with the SIMFIP. He found out that we need to have supports for three different electrical feeds, a fiber optic feed, the larger diameter tubing, and two smaller diameter sets of tubing (made up from the 9 spools of the smaller diameter tubing. We did not bring enough jack stands to support this number of spools. We also noticed that these spools (which have varying amounts of tubing on them) were not labeled – thus we needed to figure out a way to identify which reel corresponds with which length. To obtain more jack stands, Henning verified that the closest store that carried them was in Norway. Henning and Pat drove out to the store to procure more 8 more jack stands, four 1 m long threaded rods 30 mm thick (for the spools to rest on between the mounts), duct tape (to help cover over the threads on the rods), safety flagging tape (to block off the area where the winch cable was located), and safety glasses. We may need some 30 mm nuts to help secure the reels on the spools with the threaded rods – we may be able to procure these locally on Monday. We also purchased a household scale, which we used to weigh each of the 9 reels of thin tubing, so that we could estimate what length of cable they contained (matching them up to the reported weights of cable (minus the spool) listed on the shipping document). Paul and Yves continued to make good progress with the assembly and testing of the SIMFIP tool. Benoit and Alex spent the afternoon reviewing the logging results – it appears that the gamma log results match the previous results quite nicely – the results of the EC logging are not so clear – they will continue to review the data. Having two intervals of lowering the head of the well prior to relogging the well may have created a complex (and perhaps confusing) conductivity signal. Henning provided Pat with instructions on how to switch on and off the generator, and how to turn on the water pump supplying the water tank. He also showed where the inlet pipe is located in the stream. Paul and Yves noticed that large puddles of water accumulated on several roof panels of the SIMFIP tent, and proceeded to empty them (one onto Paul!) – we need to pull the roof panel tighter to avoid these in the future. Jan-Erik headed back to Lund in the evening. Pat remained at the site overnight to keep watch. A car did stop in front of the camp during the evening and the driver got out – it looked like he was taking pictures down the road – Pat stuck his head out of the tent, and the car eventually left. It rained during the night.

Set up and testing of seismic monitoring system in monitoring boreholes.

Lessons learned – We need to communicate clearly the logistical needs of the team. The misunderstanding of the number of spool stands needed could have posed a real problem in the next few days. We still need to figure out how these stands will be configured, and also need a way to properly anchor each of the stands so that they will not tip over when in use.

June 9th – We headed back to the well site just after 8 am. We put up the tripod to get a better idea of where to place the different items, and how the winch line will be oriented. We decided to pull off the wellhead cover so that the sheave could attach directly to the wellhead instead of having to pull over the lip of the cover. We first cleared away the gravel, then used boards and rods to pry the top off a bit. We then decided to hook up an end to the truck winch and slide it off. We had a quick safely meeting – we all put on hard hats for this job, and also made sure that nobody had their hands underneath the metal plate so that they could get their fingers pinched in case it fell. We positioned some rocks underneath as well so that the plate would not fall fully on the ground. We attached a strap to the far side, and were successful in sliding the plate off of the well. We had to help lift it a bit so that the bottom portion (a cylinder that hangs down) would not catch the actual well head and also not get damaged as we moved it away from the well head. We had a successful operation! We noticed that one of the pins for the tripod was missing – this will be an item to search for at the hardware store on Monday. We also thought about the best way to get the LBNL winch into position – we considered moving the tent forward (and then using the crane to lift it into place). Given that this would be a non-trivial operation, we decided to see if we could either have the crane position it along the side of the tent and then use the truck winch to pull it inside, or else to ask the crane operator to have a fork lift come to the site as well to move it into position. We tried using a hose to siphon off the water out of the wellhead area – this proved to be unsuccessful. Farzad and Alex went to town to get more diesel and to purchase a bucket to bail out the wellhead area. We moved the thin reels over to the other side of the tent – the plan is to have the heavy tubing reel on the side by the container, and the other reels on the other side. We also discussed how to anchor the jack stands in place – we have 28 spare tent stakes that we can use (four for each of the smaller stands, six for the larger triangular stands) – thus, we will need to obtain some additional stakes if possible. We discussed the results of the conductivity and gamma surveys from the previous day – the gamma results look good, but we did not see the conductivity spikes next to the inflow zones. One key difference was that when the logs were run previously, the pump was left on, so that the decrease in water head was maintained during the logging run. Because there had been past problems in the cable from the logging tool cutting the water discharge hose, it was decided to not run the

pump and the EC log simultaneously. Henning and Chris then departed back to Uppsala with the truck – Chris will be returning on Tuesday. Alex and Farzad returned with the diesel and some buckets. We used the spout to fill up the tank – we used two 20 L tanks (40 L total), and ended up with the gauge indicating that the tank was 7/8 full (it was on about 1/8 when we started). When using the second fuel can, Alex noticed a small drip from the connection between the tank and the spout – we repositioned it in place and the leak disappeared. Alex used some paper towels to mop up the few drops of diesel that had dripped on the fender and axle of the generator unit. We then used the buckets to empty out the sump around the well – there is a slow drip from the top of the wellhead as the well is flowing very slowly. Benoit worked on developing a protocol for identifying the depth using characteristic gamma peaks, and also figuring out the distances between the packers and clamps using a digital depiction of each zone of interest. Alex worked out the pressure drawdown curve for the cased section of the borehole using the data from the earlier pump test to estimate how long for a given pumping rate it will take to pump down to 75 m and he also looked at the well recovery to estimate the pump rate needed to maintain a steady state water level. Emil and Farzad returned back to the apartment early in the afternoon, and Auli, Alex, and Benoit left in the late afternoon. Paul and Yves continued assembling the SIMFIP unit – it is growing longer as each component is being added. Paul and Yves have been having trouble getting the wires for the gamma tool fed through the thin metal tubing – it keeps on getting stuck and/or broken. There is another wire for this purpose that is in the shipment that will make this job much easier. Pat remained at the site overnight to keep watch.

(Left) Removal of the metal wellhead cover so that we could directly access the wellhead (Right) Bailed out wellhead – open bolt holes can be used to secure the bottom sheave.

Lessons learned – We will need to maintain the water drawdown in the well by keeping the downhole pump running when we are using the SIMFIP tool if we are to see fluid entries where the previous FFEC logging runs indicated water inflow. Thus, it will be critical to secure the pump cables and hoses to the main SIMFIP cable when we are lowering it into the borehole so that they are not damaged. It would also be helpful to be able to use the InSitu Troll sensor so that we can monitor the water level in the borehole – the pressure sensor in the SIMFIP may not be sensitive enough to provide a good estimate of the water level.

June 10th – Because of the setback with the wiring for the gamma probe, we postponed the crane, but requested that a fork lift come out to the site to help with moving heavy objects. Pat and Alex went to the local hardware store to obtain some plywood boards, a metal rod to replace the missing pin on the tripod,

and a large step ladder for splicing lines when installing the tool down the borehole. The fork lift operator was able to move the LBNL winch into position in the winch tent (we opened up the side of the tent), move the metal well cover out of the way, lift and position the thick stainless steel cable onto two jack stands, and place the two electrical spools on two other pairs of jack stands. Auli was able to recover the FedEx shipment for Paul – this contained some critical parts (the feed wire for the gamma tool, the compass, and the conductivity probe, among other items) – this was a lifesaver. Yves and Paul were able to pass through the correct gamma tool wiring through the conduit without any difficulties! Benoit continued to work on developing a routine for identifying key gamma peaks, finding our target zones, and correcting for any difference in depth on the Uppsala depth counter while using our thicker cable. Yves worked on MatLab routines for interpreting the SIMFIP data, and Emil prepared for obtaining the gamma log tool data using the LBNL cable attached to the Uppsala system. We secured the LBNL winch using the same straps that we used for the Uppsala winch (to the trees). We noticed that we were one jack stand short for our setup; we need three jack stands to support the multiple reels of the thin metal tubing. We fashioned an additional stand by using the wooden pallets for one of the lighter reels. Paul attached the aluminum section where the compass gets mounted to the tool, and also wired up the gamma tool coupling. We refueled the generator, and took four empty tanks down to the nearest gas station for refueling.

(Left) LBNL winch moved into position with the forklift (Right) Paul and Yves successfully threading wiring through the SIMFIP conduit for the Uppsala gamma tool.

Lessons learned – Having flexibility in executing plans is critical – substituting the fork lift operator for the crane was very helpful in allowing us to prepare the site for installing the tool with the crane the following day. Having Auli track down and retrieve the shipment was critical in moving the project forward.

June 11th – We started at the well site at about 8:30 am and continued working on the SIMFIP. Emil did a test of the gamma tool connection through the LBNL cable, and found to our dismay that the tool was not

compatible with the cable! We then proceeded with our backup plan, which was to use both cables - the Uppsala cable for the gamma tool (which would then be suspended above the SIMFIP tool), and the LBNL cable for the SIMFIP. Pat and Alex went out shopping for materials to help secure the bottom sheave system to the wellhead – they obtained some eyelet pieces that could be connected to bolts that would fit through the open bolt holes on the well head. They also purchased a spare heavy-duty extension cord (that Paul will modify for use with the injection pump) as well as a few additional items. We placed three thick plywood boards over half of the opening of the well cellar so that the ladder could be used safely. The crane operator arrived just before 1:30, and once the modified SIMFIP (now without the gamma tool below) was ready, we had everyone help lift it so that the crane could lower the SIMFIP into the borehole. Just before that, we held a safety briefing to go over the need for hardhats when the crane was being used, and to have one person coordinate all of our movements with the tool. We discussed with the crane operator what we wanted him to do before we started to move the SIMFIP. The lifting and positioning of the SIMFIP went off without a hitch. Once the SIMFIP was positioned partially into the borehole and secured with two clamps, we then put the tripod into position, adjusted the angles and locations of the legs so that they met the safety criteria (the spacing between the legs could not be more than 75% of the height of the tripod), and also added straps to keep the legs from shifting. We then moved the ladder in place (having a person hold the ladder below while another person was on the ladder), put a load indicator on the eyelet, and then hoisted up the sheave and secured it to the bottom of the load indicator. We then fed the cable through the sheave and then attached the cable to the top of the tool. We then used the bolts and eyelets we had purchased along with a loop of webbing to secure the bottom sheave to the wellhead. We fed the cable line through the bottom sheave as well, and checked on the alignment of the tripod assembly. We made a minor adjustment to the tripod so that it was properly positioned so that the tool fed into the hole properly. We rotated the Uppsala winch by 180 degrees so that the counter would function properly when the LBNL cable passed along the top of the counter wheel, and disconnected the feeder arm that helps spool the cable back on the winch. Emil left to catch the train back to Uppsala, after doing some additional testing to verify that the gamma tool was working properly (and would work with a wire cable nearby), and showed our remaining crew how to properly operate the gamma tool. We set up four spools of thin tubing on a single rod using three jack stands – we chose two pairs of spools that had very similar tubing lengths (and were the longest) so that when they ran out, they would run out at about the same time so that both reels of tubing in a pair could be replaced at the same time. We pulled out the bottom ends of all of the fiber and electrical spools so that they could be connected to equipment later. Chris Juhlin arrived at Åre in the evening. Pat remained at the site overnight to keep watch.

(Left) Testing revealed that the gamma tool didn't work with the LBNL cable (Right) Paul cutting off the cable connector that we had constructed for the gamma tool at the bottom of the SIMFIP tool.

(Left) The team lifting the SIMFIP tool off of the table (Right) The crane lifting it in the air prior to positioning it partway into the borehole.

(Left) Moving the tripod into place (Right) Securing the bottom sheave onto the wellhead.

The end of a successful day!

Lessons learned – Even after doing extensive advanced planning to have the proper connectors for the Robertson gamma tool, we ended up not being successful having the tool work with our cable. Fortunately, we had a back-up plan envisioned previously (using the Uppsala winch), so we will be able to proceed. Having options available is critical when plans don't work as conceived.

June 12th – Auli arrived at the site at 8:00 a.m., just as the toilet servicing truck was starting to work on cleaning our toilet in the container. Pat, Yves, and Paul arrived around 8:15 a.m. and got the tents opened and generator refueled (10 L added) and working. Georgios arrived on site to help our team – we had a brief safety meeting to discuss the need to wear hard hats when people were working on the ladder, to have caution with the winch cable when it was moving, to be aware of tripping hazards, to be aware of electrical safety, to use gloves when working with the winch cable and the cable and tubing spools, and to alert everyone if somebody noticed any safety issues. Farzad and Georgios returned to town – we won't need more help until the afternoon at the earliest. We moved items around in the winch tent to make room for the injection pump, moving the UPC to the other side of the tent to be away from the pump, suspending electrical wires in the frame of the tent to eliminate tripping hazards, and shifting the position of the electrical box coming from the generator so that it would be protected by the tent from the pump in case any water was spilled. Yves and Paul proceeded to work on splicing the fiber and also making the many connections needed prior to putting the tool down the borehole. Auli left for Ostersund to pick up Joshi at the airport. We worked on making the pump hose connections from the large hose that comes from the water tank to the pump flow meter line – this requires new adaptor pieces, which Pat and Alex obtained from the hardware store in Jarpen and installed to connect the pump hose with the hose to the water tank. Paul rewired the injection pump so that it had the proper plug connection – he had to take off the CGI cable section so that it wouldn't trip. We were able to get the water pump and flow line to all work. Yves spliced a connection to the fiber reel so that we could hook up the interferometer, and Paul spliced and glued the wire connections for the probe. Pat took Alex back to the apartment and returned to work. Auli came out for a quick visit to ask if we should have the rest of team wait until tomorrow to join the effort – we decided that would be the best course of action. The team then worked on connecting all four of the thin stainless steel lines to the probe – the first two were flushed with water using the pump – it took about 5 minutes to flush each line with the pump operating at ~1000-1500 psi. Chris Juhlin stopped by for a quick visit to check on our progress. The lines were connected to the probe using Swagelok fittings, and then pressed into the aluminum block. We cut off a 3 meter section of the thick steel tubing, made it as straight as possible, and then connected it to the tool. Auli came up around 7:30 pm with pizzas for us! Auli, Yves, Paul, and Pat had a quick conference call with Chin-Fu to discuss the priority of depth intervals, given that we are likely not going to have enough time to investigate all of the intervals that had been identified as possible targets. We tentatively decided on looking at the flowing fracture at 506 m (it was a fairly simple fracture), the most transmissive fracture at 696 m, and an unfractured zone at 830 m (this would provide information relating to the stress regime) – if time permits, we could also look at either a zone with a steeply dipping fracture (1210/1214 m) or a non-transmissive fracture (595 m). Finally, we spliced the fiber cable to the fiber on the tool, and then used the interferometer to make sure that we had a signal. We saw the 7 peaks that we usually see – we also saw seven much smaller peaks – perhaps this is an artifact of using such a long cable. We finished at the site at about 9 p.m. Pat returned to the site to keep watch overnight, and refueled the generator with 20 L of diesel. Rain is in the forecast for tomorrow!

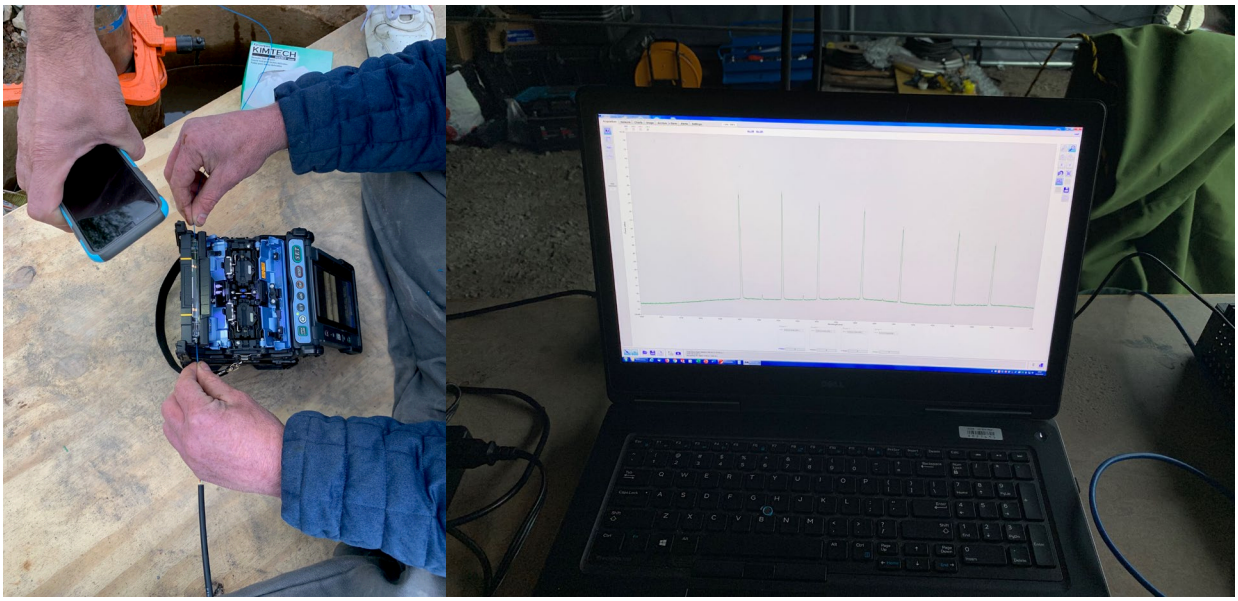

(Left) Splicing of the fiber from the probe to the spool (Right) we see the seven peaks, indicating that we are getting a good signal!

The system with all of the steel tubing connected – only a few more steps before lowering the tool into the borehole!

Lesson learned – Predicting how long it takes to hook up the tool is a very inexact art – it must be done carefully and slowly. It cannot be sped up by having more people available.

June 13th – Chris headed back to Uppsala, and the rest of our group went to the site at around 8 a.m. We started the generator, and had a short safety review, discussion lifting, tripping, wearing PPE, electrical hazards, and the use of the toilet. – Joshi is a new addition to our team. We used buckets to empty out the well sump. Paul checked the compass circuit before mounting it on the probe and noticed that the system only worked when the wiring was bent a certain way, so the decision was made to take apart the compass and repair the connections. Given that this needs time to let the glue dry, the decision was made to send Farzad, Joshi, and Georgios back to the apartment. Alex and Pat went to Åre to return some unused items and to obtain two new lights for the winch tent. We found three raincoats in the Uppsala safety gear – they are available for people to use in the rain (it is raining steadily now). We installed the new lights in the winch tent over the computer tables. The compass connection failed again – Paul reattached it another time. Paul worked on getting all of the data transmission lines working. We tested the load cell on the upper sheave – it is working properly. The replacement N_2 regulator arrived (it is rated for 200 bars in, 200 bars out); we shipped out the other regulator, and installed the new one on the nitrogen tanks. Pat took Alex back to the apartment to work with Benoit on the script for estimating depths. We bled the packer valves using the hand pump. Yves taped up all of the connections on the upper portion of the SIMFIP. Pat added another 20L of diesel fuel to the generator. Paul finished with the compass wiring/taping/gluing, and found that the groove for it in the aluminum housing was a bit too small. He proceeded to mill out a larger groove, and then tested the compass. It read 206 degrees – Paul's iPhone compass read 214 degrees, and Pat's iPhone compass read 246 degrees. Yves taped up the aluminum section. Alex, Benoit, Joshi, Giorgios, and Farzad all returned. Jan-Erik and Johan (a driller from Lund) stopped by for a quick visit – they are here to talk to contractors for building the well pad for COSC-2. We decided to take off the outer thick tubing that was spooled over the main section of tubing – we then discovered that the tubing was oriented in the opposite direction. Paul used blocks of wood and a thick packing strap to secure them under the spool, and used the hand cart (along with many people holding on to the spool) to rotate the spool 180 degrees and position it properly. We then used a Swagelok connection to attach it to the tool. We decided to attach a tape measure to the top of the packer to provide an analog option for tracking our depth. We started lowering the tool, and attached the conductivity probe to the wireline as we moved into the hole. At around 11 p.m., we decided to call it a day. Pat returned to serve as night watchman.

(Left) Attaching the repaired compass to the probe (Right) Securing the conductivity sensor strip to the wireline.

The end of a successful day!

Lesson learned- Always check each component carefully before attaching it to the probe – because Paul did a careful inspection of the compass, he discovered the faulty wiring, thus avoiding us having to come out of the hole later to repair it.

June 14th – We began work at around 8 a.m. under overcast and chilly conditions. Pat added 20 L to the generator and turned it on. We first worked on attaching the gamma probe to the line above the conductivity probe. We then continued to lower the tool and all of the connections down the borehole. The method we developed was to use a hose clamp to secure the thick metal tubing to the wireline cable, then gorilla tape to secure the four thin tubing lines to the cable and thick metal tubing, and then electrical tape to attach the electrical and wireline cables to the assembly. The spacing of each hose clamp is about 1.8-1.9 m (Paul's height). We started moving down the hole at a fairly slow rate, but got faster as we learned how to be more efficient. We found that we could spool out the electrical and fiber cables ahead of time, and focus on the metal tubing spools. Alex managed the computer, the wireline controls, and took notes each time we compared the analog depth reading using the measuring tape with the recorded depth from the Uppsala depth indicator and the actual depths obtained from the gamma peaks from the master gamma log. We had no difficulty in reading the gamma peaks (we had some concern that having the probe next to the wireline cable might be problematic). Bjarne arrived on site, and we had him go to the store to refill four of the 20L containers (he mentioned that he filled them to about 15 L to avoid overfilling them) and to obtain another 50 m reel of measuring tape. Auli went to the store to purchase an additional three 30 m reels (their remaining stock), and buy food for us. Jan-Erik and Johan (a driller from Lund) stopped by for a quick visit. We reconfigured our crew to have one person on the ladder to help feed the thick metal tubing to the wireline – this helped with the clamping. We continued to use measuring tape to help verify the depth down to 250 m (one tape of 60 m, two of 50 m, and three of 30 m). Auli took Benoit to the train station just before 3 pm, and purchased some additional food so that we could make dinner. We had started to run in the hole at increasing higher speeds (going from 5 to 10 to 20 amp settings on the wireline winch), when suddenly at around 5 pm, the wireline continued to run into the hole after Alex hit stop. Paul pulled the plug on the winch, and it stopped after running into the hole for about 10 meters. Paul put on the wireline clamp to prevent the wireline to go down the hole, and then checked the control settings of the winch to see if there was some problem with them. Yves decided that he and Paul would work on the winch system, and sent everyone back to the apartments to have dinner, with the plan to restart at around 7 p.m. Auli took Georgios to the train station. Paul adjusted the settings, and after everyone returned from dinner, we then tested the winch to make sure that it could move up and down out of the hole and the wireline could be stopped. We then pulled back out to where we had last clamped the tubing, and proceeded at a slower rate (5 amps, then 10 amps, then 15 amps) back into the hole. Just before 8 p.m., we had a similar episode where the wireline wouldn't stop going into the hole. When Paul pulled the power plug to the winch, the wireline started to speed up going into the hole. Paul and Yves were able to stop the wireline manually by applying the wireline clamp and positioning the "frying pan" tool to protect the cables. We then stopped again while Paul looked at the wireline programming – he found that the default setting for when the wireline was stopped was "free fall" – this was why it started spooling out so rapidly. We surmised that earlier on, when the weight of the cable in the hole was less, the gearbox helped stop the cable. After modifying the default setting to "brake", we then tested the wireline, and were able to control it going up, down, and stopping it. We added an additional safety feature to our procedure – we kept the wireline cable clamp attached to the wireline above where we are attaching the tubing and cables, shifting it each time we attach a new section of the cables and tubing – that way, it is already deployed in case the wireline starts to run on its own. We contacted Benoit to find out about possible fallback options for shallower fractures – he sent us a file with these details. We then pulled the 10 m of cable that had gone into the hole during the free fall event, and then went in at a slower (5 amp) rate, ending the day at around 10 pm at a total depth just beyond 360 m.

(Left) Attaching the gamma tool onto the wireline (Right) Strapping on the different tubing and cables onto the wireline as we go downhole with the SIMFIP.

The wireline clamp and "frying pan" tool in place securing the line from moving downward after the wireline "free fall" event.

Lesson learned – Be sure to review the settings of any equipment before it is put into use. The default settings of the winch were dangerous – fortunately, Paul and Yves had a backup method ready to help stop the downward movement of the winch cable.

June 15th – We arrived at the site again just after 8 a.m. It is drizzling lightly – not the warm sunny day that we had expected. Pat refueled the generator – the first fuel can that he used leaked from the connection between the can and the spout (even after several attempts to adjust it) – Pat stopped using that can, marked it as leaking, mopped up the spilled drops of diesel, and used a different can to refill the generator. We had a long safety discussion prior to starting work. We went over the events of the previous day, mentioning the need for good communications (which we had yesterday), noting anything that seems not normal. We reiterated the need for anyone working under the tripod to be wearing a hard hat at all times. We believe that we have the issue of the winch motor solved – it should have plenty of power to do its job – we just need to make sure that the controller is properly configured. Alex noted that prior to the winch going out of control, it was experiencing about 10 cm of continued movement after he hit the stop button – this may have been an early warning sign. Paul suggested that we reconfigure the location of the load cell – it is currently at the top of the tripod between the tripod and the sheave – although the load cell is rated to 10,000 lbs., the connectors to the tripod and the sheave may not be so robust – we wanted to make sure that the load suspended from the top of the tripod is as secure as possible. We then discussed repositioning it to the bottom sheave, where it would see less load. We then talked about how to do this – Paul suggested that we lift up the line a small bit, put a copper lining on the wireline clamp (so that it will clamp better), then place the weight of the line on the wireline clamp, take off the top sheave and the load cell, replace the top sheave, put the load cell on the bottom sheave, and then reposition the cable so that it is in exactly the same position as when we started the day. We will use straps to help hold up the top sheave – it is quite heavy. When Paul put the weight of the tool onto the wireline, it shifted a little bit. He then decided to only put copper on a single side with the thought that the wireline would be gripped more securely. While doing this, a section of copper from the clamp did fall down the wellbore – hopefully this won't cause any issues. We then put slack in the cable, disconnected the load cell, reattached the sheave, and put the load cell on the bottom sheave. We then noticed that the weight distribution on the tripod changed, causing it to move slightly (Yves noticed that two of the bottom guy straps were now loose, and that one of the legs had moved). We then shortened the straps for the bottom sheave that were attached to the wellhead so that the assembly was as close to the original position as possible. We also put in two stakes with straps on the tripod leg away from the winch to provide extra support. Paul and Yves then worked on repositioning the wireline so that it would be in the same position as when we stopped the previous evening. We then continued going into the borehole. At one point, Paul was testing the load cell by adding his weight to the wireline, when the winch started to slide, rotating in one direction. We then stopped, secured the wireline with the wireline clamp, and then secured the winch more carefully, using a third strap to tree, and also placing three stakes in front of the winch. We tested the winch security by having Paul hang on the line again – this time, it didn't move. We then proceeded to go down hole again before breaking for lunch at around 1 p.m. We then restarted going back in the hole. Pat left around 2 p.m. to look for more hose clamps – all of the local hardware stores closed at 2 p.m., but he found some clamps at the Q8 station in Jarpen. The team had determined the depth where the pump should be set, and we reached that depth and started putting the pump in place. We did a quick safety check to verify that the winch will pull the tool up – this worked without any problems. We broke at around 5 p.m. for a short break – Pat added two additional cans of fuel (probably about 30L) to fill up the generator. We then resumed our work putting the tool and all of its attachments down the borehole. We succeeded in getting the pump down to the target depth (~499 m for the gamma log tool), and then tested the conductivity strip (it worked!) and the pump – it also worked. As a secondary check on depth, the 75 m mark on the pump line appeared at the well head right when we got to the target depth! After additional setup and testing, we ended up leaving around 8 p.m. Pat returned to keep watch on the site overnight.

(Left) Successful rerigging of the load cell onto the lower sheave. Note wireline clamp and "frying pan" in place. (Right) Auli overseeing our operations from above!

(Left) Alex manning the winch and the gamma log mapping. (Right) Paul, Yves, and Joshi attaching the pump to the wireline.

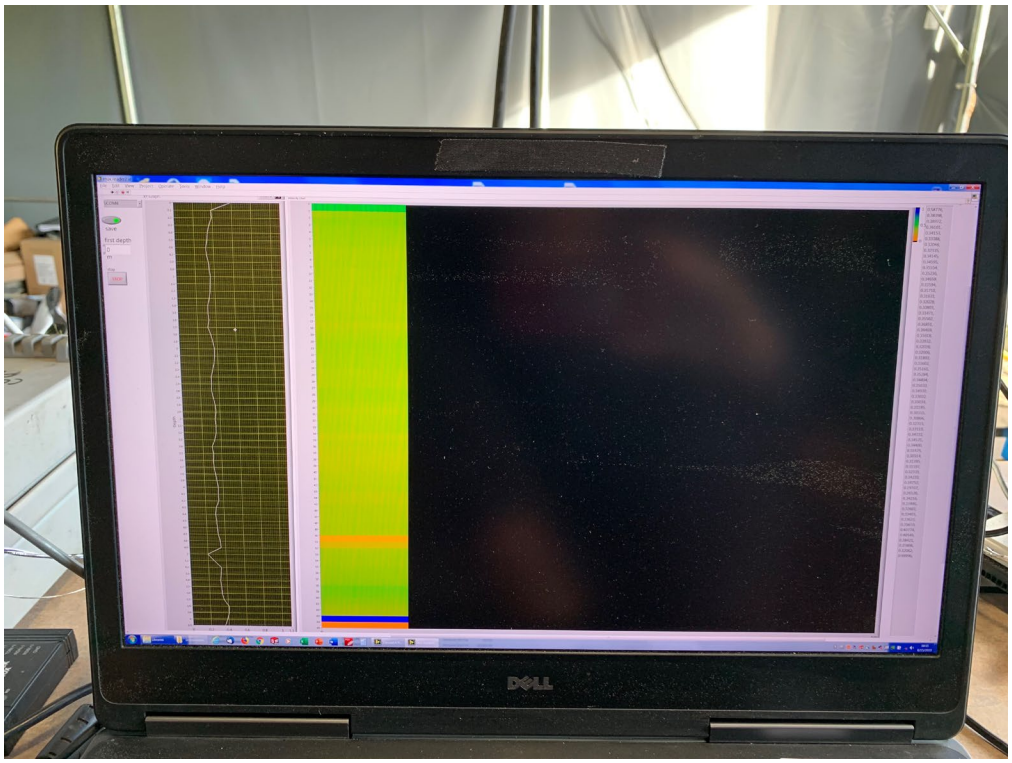

Signal from the conductivity array at 506 m– one zone has a small conductivity spike (this may be a spurious signal).

Lesson learned – We spent a good deal of time addressing safety issues (rerigging the load cell, securing the tripod leg, reinforcing the winch anchors, etc.) It is critical to make sure that you dedicate the time needed to have safe working conditions.

June 16th – We arrived at the site at 8 a.m. and Pat started up the generator. Paul checked the fiber system – it is still working! Paul proceeded to hook up the injection pump system and did a quick bucket filling flow test to verify the flow meter reading. We had a brief safety meeting before getting going. Paul connected up the fiber to verify that it was still working, and he also hooked up the pressure transducer so that we could monitor the progress of the head drawdown once we started pumping. Farzad got the Uppsala pump set up, and finally at 12:19 p.m. we started pumping with the injection pump. The reel of tubing was filled with air, so it took quite a bit of time for the system to become purged. We finally noticed an increase in the outflow at the wellhead around 12:50 p.m, suggesting that injection was occurring (with an injection rate around 3 lpm. We then started to pump with the Uppsala pump to try to set up a quasi-steady state with injection and pumping at 12:56, but stopped a few minutes later when we noticed that the Grundfos pump interfered with the readout of the pressure transducer and the flow meter of the LBNL pump. We tried grounding the pump, and restarted to Grundfos pump at 1:10 p.m., only to see the same issue. We stopped again at 1:12 p.m., and tried grounding the generator, but the problem persisted. The electrical cable leading downhole to the pump is not well shielded – that may be the root of the problem. One other issue that we encountered was that the electronic data logger for the Grundfos pump wasn't working – Pat and Farzad took turns writing down the pump data (time, pump motor setting, flow rate, and cumulative flow values). We then decided to go ahead and pump, starting at 1:20 p.m. at a rate of ~5 lpm (at that time, Paul had increased the injection rate to about 3.9 lmp). We maintained that rate until 1:48 p.m., when we stopped injecting and then increased the pump rate to ~ 10 lpm. We decided to stop injecting when the conductivity values measured by the EC/gamma logging tool had decreased below 150 µS/cm and appeared to stabilize, suggesting that the slug of fresh water that we were injecting had made its way from the injection point

between the packers up to the EC/gamma tool. The lowest EC values detected by the tool for the zone where the gamma tool was located was around 120 µS/cm – the baseline (pre-injection value) was above 450 µS/cm (check with Alex, who was monitoring this). Paul made intermittent measurements with the pressure transducer – we were able to do this by stopping the pumping for a few seconds while Paul could read his instruments. Paul got readings of 630 psi at 2:51 p.m., 626 psi at 3:01 pm (when we had a head of 75 m), and 625 psi at 5:50 pm, and a final reading of 624 psi at 6:10 p.m. (Paul took additional pressure readings at other times). During the afternoon, Bjarne and Joshi left our group. We achieved a drawdown to the level of the pump (75 m below the surface) at 3:01 p.m., which was noted when the flow rate on the pump changed rapidly towards zero. We then halted pumping for 10 minutes to let the head rise a little bit, and then resumed pumping at 3:11. Because we had not turned off the valve of the pump line when we turned it off, all of the water in the line had drained back into the well, so even though the pump had been turned back on, there was no flow registering at the surface while the line was refilling. We pumped slowly (in part to make sure that the pump would not be damaged if indeed it was not immersed), and finally water started discharging at the flow meter at 3:23 p.m. We pumped at a rate of ~6 lpm to maintain the head near 75 m – at 4:13 p.m., we slowed down the pump rate to around 4.5 lpm. We kept pumping until 6:10 p.m. The rationale for this was to match the three hours of pumping that had been done for the one of the log runs – this produced a less pronounced but also less diffuse signal for the peaks. We saw based on our own observations as well as those obtained by Chin-Fu earlier that it would not help identify individual fracture flow entries by running the test longer – the peaks tended to merge into a larger composite feature. We also saw that the bottom of the conductivity array appeared to be more conductive towards the end of the test – this just might be the unreplaced wellbore water moving upwards as we continued to pump (replacing the fresh injected water that was above it). Farzad added an additional 20L of diesel to the generator – Alex and Farzad then drove to refill the diesel fuel cans and to get dinner, and Pat went shopping and cooked dinner to bring to Paul and Yves. Yves spent quite a bit of time trying to work with the recorded conductivity data to identify actual inflow peaks where increases in conductivity would indicate proximity to a fracture (the sensor has ~60 registering stations located about 10 cm apart). Looking at the early indicators of changes in conductivity using the conductivity sensor that was deployed across the zone of interest, we detected three distinct fluid entry zones, the most prominent at around 504.5 m, a second at around 506 m, and a weak entry at a depth of around 507.2 m (check the actual depths with Yves). We noted that the biggest conductivity contrast appeared early on, and that as time progressed, the anomalies widened and made a much more diffuse signal, similar to what Chin-Fu observed. We also noted that the contrast between the fracture fluid and the replaced wellbore fluid was not very much – this may be due to forcing some of the fresh water into the fractures, so that the mixed fracture fluid was less saline. After much discussion, we decided to place the packers so that we would isolate the most prolific flow zone (504.5 m) from the two lower zones, and also avoid a shallower feature that we could see in the televiewer log. This would require that we bring up the tool a distance of 9.8 m – we used several different reference points to make this calculation. We proceeded to calculate what wireline distance that would correspond to with the Uppsala depth indicator, and also measured out the same distance using a tape measure on the wireline itself. Auli departed to pick up another team member at Ostersund, and Roland (a geophysics professor) and his wife and dog appeared in a camper to assist us. We quickly briefed Roland on what we were doing, and then proceeded to reposition the tool with the gamma logging tool at a depth of 489.99 m, spooling the metal tubing back on the reels – there was a very minor discrepancy of ~ 6 cm between the distance we marked on the wireline and the actual distance we measured using our calculated distance together with the gamma peaks. We then packed up our gear in the tents and called it a day at 10:45 p.m. Pat returned back to the site to keep watch (along with Roland and his wife).

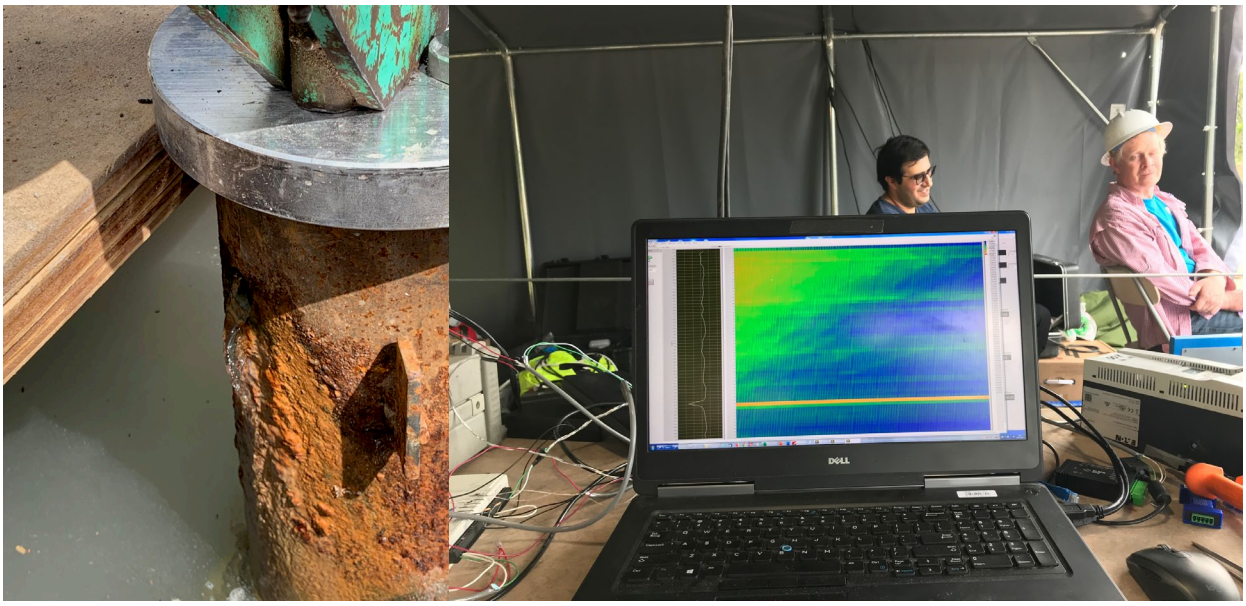

(Left) Flow from borehole increased with injection. (Right) Response of conductivity probe to fresh water flush of fracture zone.

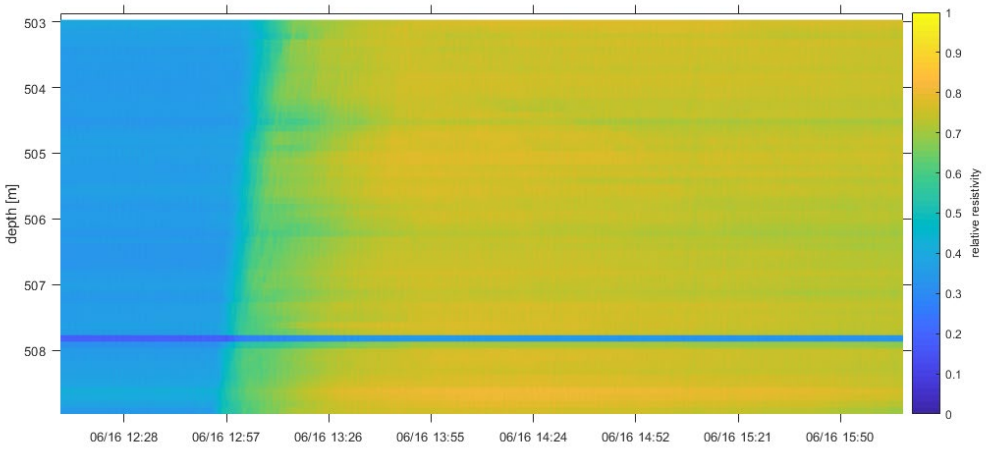

Appearance of initial salinity peaks from multiple fractures for 506 m depth FFEC peak. Blue represents higher conductivity waters, yellow represents fresh water. Blue line at 507.8 is a bad sensor.

Lesson learned – Running this conductivity test took much longer than anticipated, but it provided a key result – a feature that was previously interpreted to be caused by a single fracture inflow zone is actually a composite inflow zone with at least three distinct flowing fractures. Having this information will permit us to single out a specific fracture to test with the SIMFIP tomorrow. There may be better ways to avoid pushing so much fresh water into the fractures when we flushed the borehole interval, so that we could have better signal contrast when we produced the fractures by lowering the head.

June 17th – We encountered a setback before we even left for the well site today – Paul's primary computer died. Paul has a backup computer, so the plan is to run the SIMFIP system using that computer. We arrived at the site shortly after 8 a.m. – Roland and his wife were onsite with their camper. Eduardo joined us today – Auli picked him up at the airport last night. Auli arrived mid-morning with Emil from Ostersund. Paul worked on installing the backup computer to run the SIMFIP. He also checked the fiber – it is working. Pat and Eduardo had to prime the pump to get water from the stream to the big storage tank – it was down to

~640 L prior to refilling it back to 1000 L. The plan is to inject in the zone selected yesterday (504.5 m), then move down to a non-flowing steeply dipping fracture at 515.1 m, and then move up to a non-fractured zone (485.2 m) above the first flowing fracture. We need to be coming out of the hole before noon tomorrow if we are to be ready for the crane on Wednesday afternoon. Paul and Pat calibrated the injection pump flow rate using a bucket test. Alex and Farzad set up the seismic monitoring system to record when we begin the injection test. Alex tried to recover files on Paul's hard drive – it appears that many of the files were corrupted and can't be recovered. However, all of the data files from yesterday's tests were backed up on Yves' hard drive. We only lost the routines used to visualize the data. Paul continued to hook up the systems for the packers and clamps, and to prepare the back-up computer for running the SIMFIP. We first checked the orientation of the compass (213.8-214), made sure that the fiber system was working, inflated the packers by injecting water to 550 psi, and then clamped the SIMFIP in place. When we started injecting water into the chamber between the packers, we were dismayed to see that water was exiting the top of the well, suggesting that either the injection line had a leak into the borehole above the top packer, or that the top packer hadn't sealed. After some work with the packers, we obtained a good seal and the flow out of the borehole stopped – much to the relief of the team. We then started with the stepped pressure test – the baseline pressure was 713 psi, we then increased the chamber pressure to 780 psi and allowed the pressure to fall off and stabilize, then repeated this for 850, 900, 950, 1000, 1050, 1100, 1200 (where we first observed flow), and 1300 – we gradually increased the flow rate of the pump as needed. The behavior of the system was observed to be a bit different at this pressure, so we then went to 900 psi, then bled the chamber to a pressure of 726 psi (this sequence was the reversible test). We then increased to 990 psi, 1100 psi, 1300 psi, 1500 psi, 1700 psi, and then went to the maximum pumping rate (setting of 140) to obtain a chamber pressure of 1808 psi (flow was 3.66 lpm). We then shut in the system, and bled it off. We then used the pressure bleed off valve to run a constant pressure test at 1300 psi, and then did the same at 1600 psi. We then bled off the pressure and ended the test. Alex made a copy of the data so that we had a backup just in case. Pat refueled the generator – adding two 20L cans of fuel to it. We declamped the SIMFIP, deflated the packer, and then moved the line down so that the SIMFIP would be centered over a steeply dipping fracture at 515.1 m (this is seen in the televiewer log, and was listed by Wenning et al., 2017). We used the previous markings on the cable to come up 9.8 m – the final distance that we had to move the line was just over 10 m (~504.5 to 515.1 m). We proceeded to inflate the packer, clamp the tool in position, check the compass reading (which had rotated from the previous test – it is now reading 228). The bled chamber pressure was 727 psi, we then increased pressure to 794 psi, then 861, 911 psi, 958, 1014, 1050, 1113, 1173, 1206, 1253, 1300, 1350, 1400, 1450, 1500, and then dropped back down to 1139, 800, and 729 psi (this was the reversible test). The response for this test was markedly different from the first test – this was because of the absence of a permeable feature in the zone. We then resumed the next portion of our test at 1007 psi, stepping up to 1200, 1400, 1600, 1800, and reached a maximum pressure of around 1890 psi with the pump running at maximum speed (setting of 140). We kept up this flow rate for some time, with the pressure dropping to 1784 psi, shut in the well, and then bled off the pressure. The system then displayed an overlapping issue error message – Paul came and resolved this problem. During all of this, Emil, Eduardo, and Farzad returned to the camp with a delicious dinner of salmon, broccoli, zucchini, a dill sauce, and new potatoes for the entire team – we all had a great meal! We then started a constant pressure test – starting at 900 psi, then moving to 1100, 1400, 1600, 1800, 1698, and then shut in the system and bled off the pressure – this completed the sequence of tests for this interval. Alex made a copy of this second data set. We declamped the tool, deflated the packers, and then got the team to raise up the tool to the next (and final) depth interval to be studied – a non-fractured zone at 485.2 m. This move (~30 m) took a little less than an hour to complete. When we were moving up, Alex noticed that the gamma log was no longer displaying a signal. We replaced the car battery with another, and the signal returned! We had marked off the depth that we had to move the array directly on the wireline – Alex noticed about a 2 m discrepancy between the measured analog depth (which we used, and which was consistent with the gamma peak map), and the displayed depth from the logging system – perhaps this was in part caused by the short time where the power was low and the gamma tool wasn't displaying a signal. We turned off the generators and left the well site at around 12:20 am. We put out safety barriers to make sure that nobody would drive over the

cables on the ground. Pat later returned to watch over the site in his tent. This was a very successful day for the team – everyone worked extremely long hours and we were rewarded with an excellent data set.

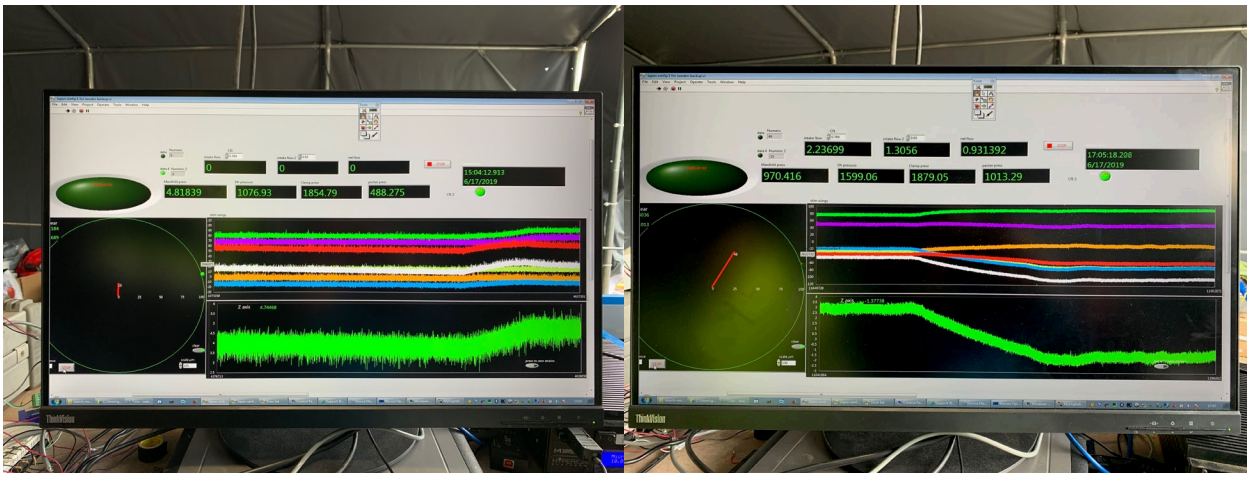

Images of flow test results for the flowing fracture at 504.5 m.

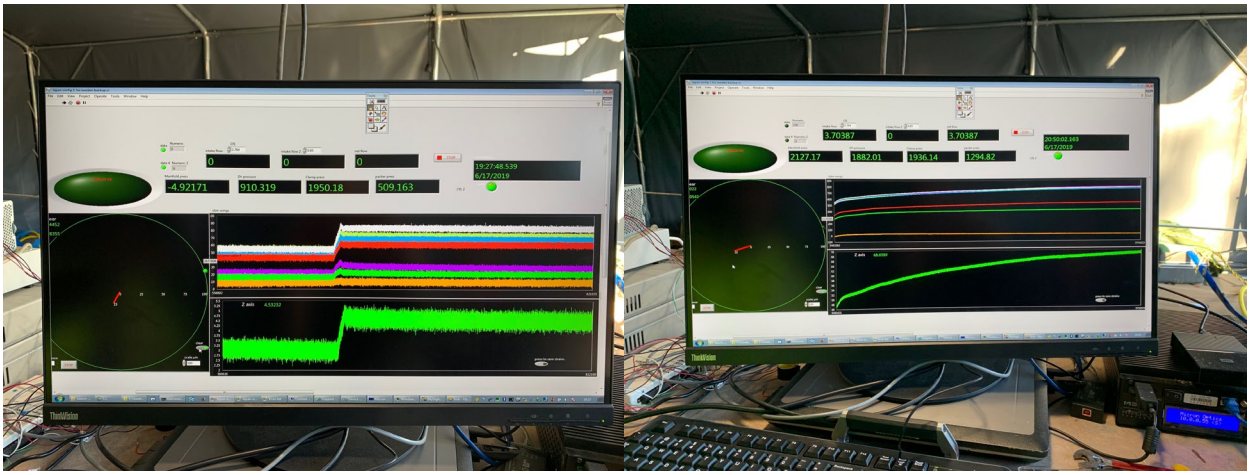

Images of flow test results for non-flowing fracture at 515.1 m.


(Left) Paul declamping the SIMFIP. (Right) Deflating the packers with nitrogen.

Lesson learned – Be sure to have backups of critical pieces of equipment. When Paul's main computer failed, he still had a second system that he was able to configure to run the tests. We did lose some time, but we were able to continue after a few hours delay.

June 18th – We returned to the site to work shortly after 8:00 – Emil and Farzad arrived first to turn on the seismic monitoring array. Pat turned on the generator, and Paul started working on reconfiguring the pump so that it would have more power. We also decided to cut the injection line so that the tubing on the reel would not have to be flowed through – this will avoid quite a bit of pressure loss due to friction. Paul hooked up the new connection, opened up the water tank valve, and started flushing the line to the packers with water at about 9:40 a.m., and then inflating them at 10:10 a.m. We then started our test of the intact rock zone at 485.2 m, beginning with a step pressure test at moderate pressures (no evidence of permeability), followed by a leak-off test (where we pumped at a constant rate until the rock broke (at a pressure of around 2250 psi), and then repeated this to grow the fracture. We then did some step pressure tests at higher pressures to look at the reopening pressure and closing pressures – this test was successful. We then declamped and then bled the packers. The final water tank level when we had completed all operations was about 400 L. Paul proceeded to disconnect all of the recording cables from the monitoring system so that we could start spooling up the cables when we begin to come out of the hole. We held a safety meeting prior to starting with pulling out of the hole to emphasize tripping hazards, lifting, communicating any concerns, wearing safety shoes, gloves with working with the spools and hard hats for every one working under the tripod. We proceeded to make great time in pulling out of the hole. We had a few mishaps with the threaded rods supporting the cable spools – the spools tended to move sideways gradually when spun on the rods, so we had to reposition the rods and spools every so often. We found the piece of copper that had fallen into the hole when we were at about 350 feet, and ended the day with just under 100 feet left to finish pulling the tool out of the hole (it clearly did not attain a depth where it could affect any of our measurements). We also organized and boxed up the downhole pump from Lund. Emil worked on disassembling and packing up the Uppsala seismic gear with help from others when time permitted. The team had another successful day in the field. After dinner, Pat went back to the site to camp out and watch over the location.

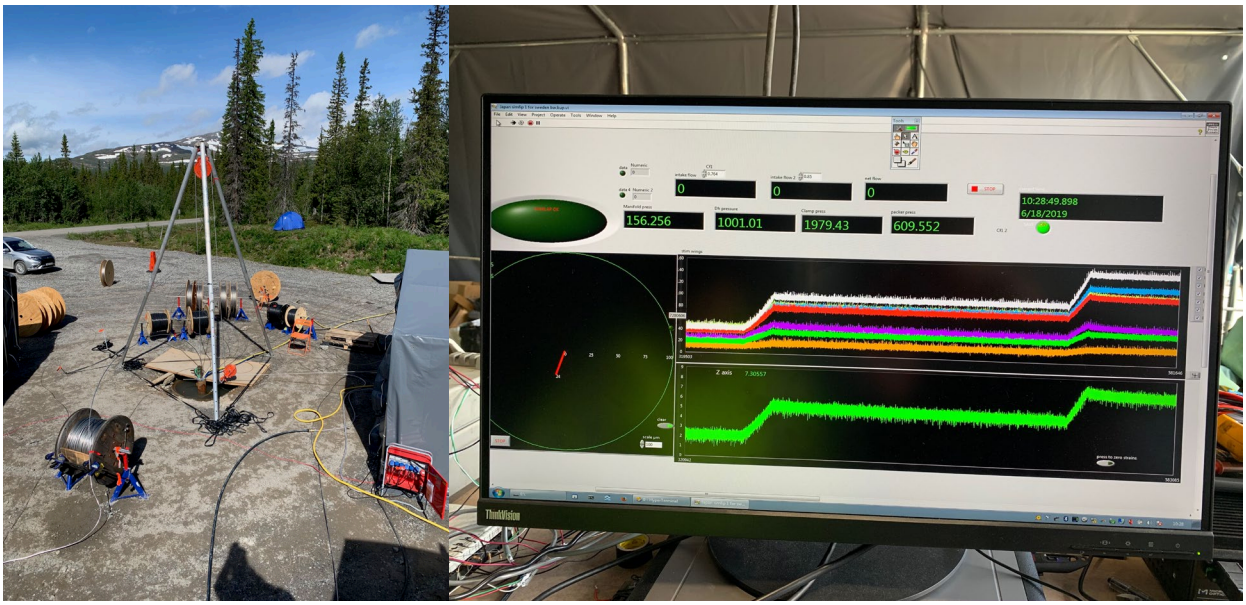

(Left) Our well site. (Right) Initial pressure step test results for intact rock zone at 485.2 m with pressure steps at 900 and 1000 psi – note no permeability.

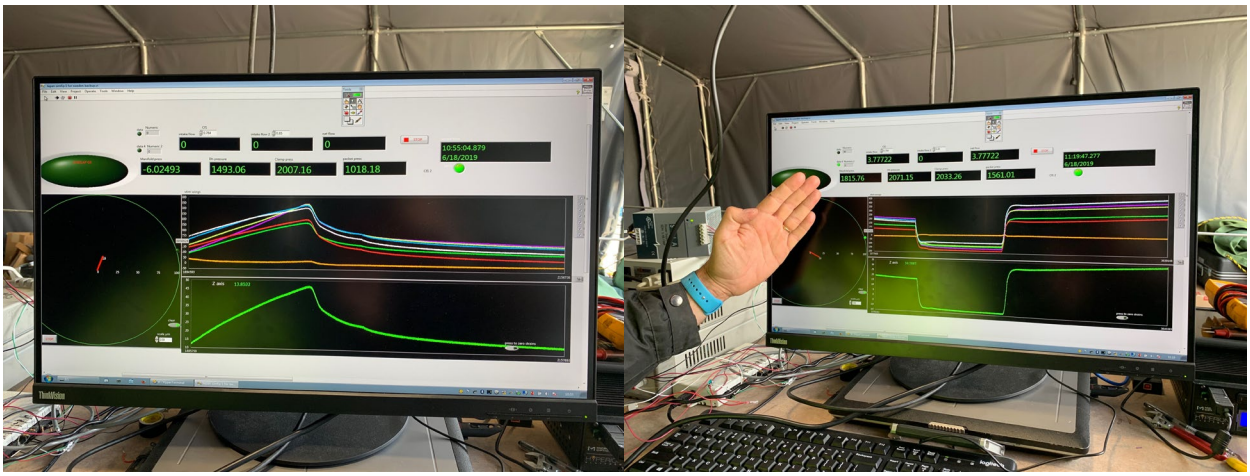

(Right) Results from fracture leakoff test for intact rock zone at 485.2 m. (Left) Further injection led to fracture opening. Yves' hand shows expected fracture orientation.

Lesson learned – Persist with your objectives. We had hoped to interrogate a flowing fracture, a sealed fracture, and intact rock when we first discussed our field objectives. In spite of all of our challenges that delayed our work, we were able to obtain good data sets for all three types of features. It was the dedication of our entire team that made this possible.

June 18th – We arrived at the site at around 8 a.m., and Pat added 20L of fuel to the generator and started it up. We had a brief safety meeting to emphasize being careful during our final day of field work, talking about PPE, lifting, tripping hazards, and communicating any concerns. We continued running out of the borehole and got to the gamma tool. One curious observation – there was a discrepancy of about 3 m between the actual (zero) and measured (~-3 m – e.g., 3 m out of the hole) depths when we got the top of the gamma tool up to the top of the casing – Emil suggested that perhaps the logging tool was not on for a short time, so we missed recording this distance (this may be related to the discrepancy Alex had noted previously when going to 485.2 m depth). We disconnected the gamma tool, then got to the conductivity probe. We disconnected it (we saw that all but one of the copper sensors had some corrosion on them – Paul confirmed that the one sensor without corrosion was the one faulty station), and laid it out carefully for packing later. We then disconnected the pressure transducer, and the feed lines to the U-tube for the packers. We finally got the SIMFIP out to the top packer, where we hooked up two clamps, and took the weight off of the wireline. We left the wireline hooked up, then carefully lowered down the top sheave, and disconnected both sheaves from the wireline. We then moved the tripod away, laid it down, collapsed the legs, and packed it in its crate. We started spooling up all of the cable lines and the tubing onto their spools. We put the spools onto their corresponding pallets for shipment back to Berkeley. We retrieved the pump, power cables, and hose from the stream and rolled the hose up. We drained the water tank, disconnected the hose, and carried the tank down to the pad. We took off the front and back of the winch tent. We reassembled the parts that we had removed from the Uppsala winch, and rotated it so that it could be used again. The crane arrived onsite at around 1:30, so we then worked on lifting the SIMFIP out of the borehole, placing it carefully on its table, we then had the crane operator lift up the thick tubing spool so that we could put it on its pallet, and then the crane lifted up the wellhole cover and placed it back into its original position. Emil had to break the lock on the top of the wellhole cover so that we could open it to ensure that the cover was oriented properly – we had to make a slight adjustment. Henning then arrived on location, and he talked to the crane operator about having his company arrange to pick up the LBNL components tomorrow for shipment back to Berkeley. Paul and Yves continued disassembling the SIMFIP so that it could be packed in its box. Emil ran a dummy tool down the hole to ~550 m so that the Uppsala wireline could be respooled properly. The generator was filled up using the remaining diesel fuel. The team took down the tents and packed the LBNL gear on pallets and the Uppsala gear into the rental truck and Uppsala truck. We tried to

move the Uppsala winch into the rental vehicle, but it was too heavy, so the plan is to have a fork lift assist in placing it into the vehicle. Pat took his tent down, and we then finished up around 7 pm. We enjoyed a delicious team dinner in Åre to celebrate a successful field expedition.

(Left) – Detaching the SIMFIP conductivity strip from the wireline. (Right) – Pulling the SIMFIP tool out of the borehole.

(Left) – Lifting the well cover back into place. (Right) – Group photo after successful field activities.

Lessons learned – If there are discrepancies in depth measurements, we should trust the gamma peak mapping and analog depth measurements over the corrected Uppsala wheel depths – there is more confidence in the actual gamma peak markers and physical measurements of the wireline (at least for fairly short intervals). Having multiple ways to estimate depth is preferred.

June 19th – Henning and Emil made a trip out to the site in the rain to oversee the fork lift load the Uppsala winch into the rental truck. They loaded up the remaining gear (such as the tent covers) in the vehicles, and made arrangements for transport of the nitrogen tanks, the trailer, the water tanks, and the LBNL gear. They then proceeded to drop off the generator in Jarpen and drive back to Uppsala with Alex and Farzad. Pat and Paul made a quick visit to the site, then headed off to see the Tannforsen waterfall. Pat, Paul, and Yves then drove to the Ostersund airport, where they returned the rental car, and met up with Auli for the flight back to Stockholm. Paul flew on to Zurich on his way back to the US, and Yves caught a flight to Nice. Auli returned home, and Pat checked into a hotel near the airport. Henning, Emil, Alex, and Farzad unloaded all of the gear from the two trucks into the Uppsala storage facility.

The well site, with only the LBNL shipment, the nitrogen bottles, the trailer, and the water tanks left for pick up.